UNIVERSITY OF EXTREMADURA

Department of Mechanical, Energy and Materials Engineering

DOCTORAL THESIS

Spark-plasma sintering of ZrB_2 ultra-high-temperature ceramics

Víctor Zamora Rodríguez

Badajoz (Spain), October 2012

GRUPO ESPECIALIZADO DE MATERIALES

UNIVERSITY OF EXTREMADURA

This work was performed in the context of the research line entitled Processing and Sintering of Advanced Ceramic Materials in the Grupo Especializado de Materiales of the University of Extremadura, and was supported by the Ministerio de Ciencia y Tecnología (Government of Spain) and FEDER funds under the Grant Nº MAT 2007-61609.

Spark-plasma sintering of ZrB_2 ultra-high-temperature ceramics

A Dissertation Presented by

VÍCTOR ZAMORA RODRÍGUEZ

in Candidacy for the Degree of Doctor of Philosophy (in Materials Science and Metallurgical Engineering) by the University of Extremadura

Supervised by:

Dr. ÁNGEL LUIS ORTIZ SECO
Associate Professor (Reader)
Materials Science and Metallurgical Engineering

Dr. FERNANDO GUIBERTEAU CABANILLAS
Professor
Materials Science and Metallurgical Engineering

Department of Mechanical, Energy and Materials Engineering
University of Extremadura
October 2012

Doctoral Thesis Committee

Dr. Arturo Domínguez Rodríguez
Professor
Department of Condensed Matter Physics
University of Sevilla

Dr. Nicolás de la Rosa Fox
Professor
Department of Condensed Matter Physics
University of Cadiz

Dr. José María da Fonte Ferreira
Associate Professor with Aggregation
Departament of Ceramic and Glass Engineering
University of Aveiro

Dr. Antonia Pajares Vicente
Professor
Department of Mechanical, Energy and Materials Engineering
University of Extremadura

Dr. Pedro Miranda González
Associate Professor (Reader)
Department of Mechanical, Energy and Materials Engineering
University of Extremadura

Badajoz, October, 2012

To All My Loved Ones

Acknowledgements

At the end of my Ph.D. Thesis I would like to thank all those people who have made this work possible and an unforgettable experience for me. It is a pleasant task to express my thanks to all those who have contributed in many ways to the success of this experience.

I would like to show my gratitude to my supervisors Dr. Ángel Luis Ortiz Seco and Dr. Fernando Guiberteau Cabanillas for introducing me to the world of the materials science, allowing me to carry out this doctoral thesis which, undoubtedly, without their help and encouragement it would not have been possible.

I owe sincere and earnest thankfulness to Prof. Mats Nygren for his priceless advices, remarks, suggestions and guidance, proposed with an extreme kindness during my several research stays at the Arrhenius Laboratory of the Stockholm University, who taught me the art of spark-plasma sintering.

I am very grateful to all my colleagues and staff in the department, for making the working environment inspiring, it is always a pleasure to come to work. My gratitude is also extended to colleagues and technicians from the University of Stockholm

I must also acknowledge to technical and human support provided by Facility of Analysis and Characterization of Solids and Surfaces of SAIUEx.

I could not forget to express my gratitude to my many student colleagues for providing a stimulating and fun environment in which learn and grow. I am indebted to all my friends and relatives for their emotional support, understanding and good times throughout my life and especially during this project.

Of course the Acknowledgements would not be complete without giving thanks to my parents. Both have instilled many admirable qualities in me , giving me a good foundation with which to meet life. They have taught me about hard work and persistence. A special mention to my sister, she is my biggest fan and supporter. I am very grateful to my mother-in-law for her friendship and many valuable contributions.

Last, but by no means least, I thank my wife María Pura for her unconditional support and love during all this time. I could not have completed this journey without her by my side. There are no words that can express my gratitude and appreciation for all you have done and been for me. Thank you with all my heart and soul.

Table of Contents

List of Figures

"Nothing in life is to be feared, it is only to be understood. Now is the time to understand more, so that we may fear less"

Marie Sklodowska Curie (1867-1934)

Chapter I: Introduction and Statement of Purpose

There exists great interest in the development of materials that tolerate very high temperatures (> 1600 °C), high pressures (> 50 kPa), strong localized stresses (mechanical contact and wear), and chemically aggressive environments (corrosive gases). Among the industries interested in these materials are the aeronautics and space sectors. Indeed, it is expected that the XXI century will see a revolution in supersonic and space flight, and in general the development of propulsion craft. Without a doubt, all these advances, as has been the case up to now, will be intimately related with the development of new materials (Fig. 1.1).

With respect to supersonic flights, it is sufficient to consider that as the speed of the craft increases, the temperature of its surface grows exponentially due to the high friction. The speed forecasts are already for Mach 6, for which reason the estimated temperatures are greater than 1500 °C, as well as very severe wear of the surfaces [1]. Therefore, one of the present challenges in supersonic technology is the manufacture of light

materials that are resistant to oxidation, wear, thermal shock, and creep in conditions of cyclic and prolonged use at high temperatures [2].

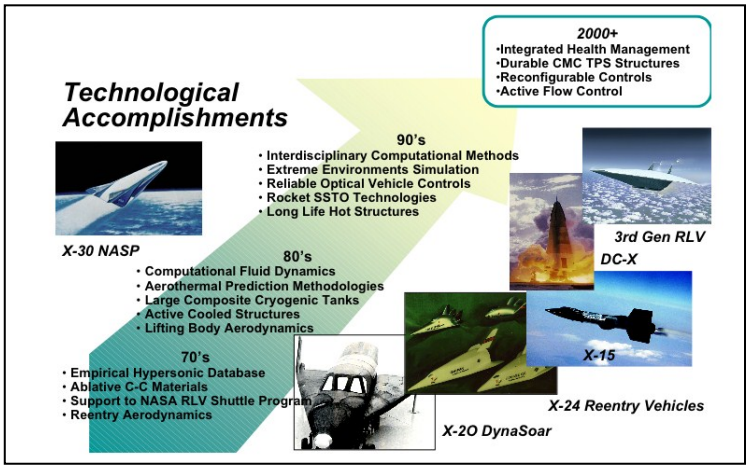

Figure 1.1. Technological accomplishments made in last tens and future forecasts within the aeronautics and space sectors.

Space shuttles are re-usable vehicles for exit and entry into the atmosphere. When returning to Earth, the nose and wing tips reach temperatures greater than 1700 °C (Fig. 1.2.A). In order to reduce those high temperatures designs with blunt shapes are used, so that the shock wave induced during re-entry turns aside part of the generated heat (Fig. 1.2.B).

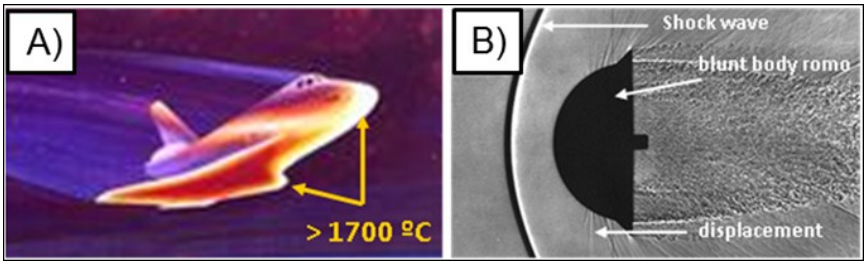

Figure 1.*2.* (A) Image of a space shuttle returning to Earth [4], and (B) shock wave generated during the re-entry to the atmosphere [5].

In order to take greater advantage of this effect, the shuttles return to Earth with the nose slightly raised. Nevertheless, this design reduces the manoeuvrability of the shuttle, and in addition causes a temporary loss of communication with the control tower. As a consequence, there are very limited windows of suspension of missions and re-entry into the atmosphere. In order to diminish these drawbacks, the intention is for the next generation of space shuttles to have pointed shapes (see in Fig. 1.3. (a) design of the X-48B and (b) conceptual design for the X43-A), even though this means that the temperatures and the wear of their surfaces will be much greater. Hence, the technical challenges are nowadays centred on the development of high temperature materials that allow the manufacture of light components that are more resistant to oxidation, damage by contact, wear, thermal shock, and creep [3].

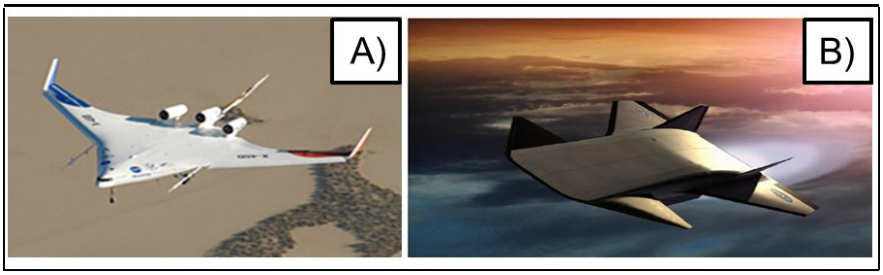

Figure 1.3. Design of a future space shuttle (X-48B) built by Boeing´s Phantom Works Division (A) [6] and conceptual design for the X43-A, a reusable hypersonic aerospace vehicle (B) [7].

Shortly the development of new propulsion engines is also expected. In real service conditions, these systems will even reach 3000 °C, in an extremely hostile environment of highly reactive dissociated chemical species, to then undergo abrupt cooling to ambient temperature. In these circumstances, the question is not if a given material will fail (it is sure that it

will fail), but how long it will take to fail. The life expectancy of the materials used at the moment in some of these applications does not surpass one minute (Fig. 1.4). The critical technical challenges are then in the development of light materials that are extremely resistant to oxidation, combustion by gases, thermal shock, wear, and creep at high temperatures.

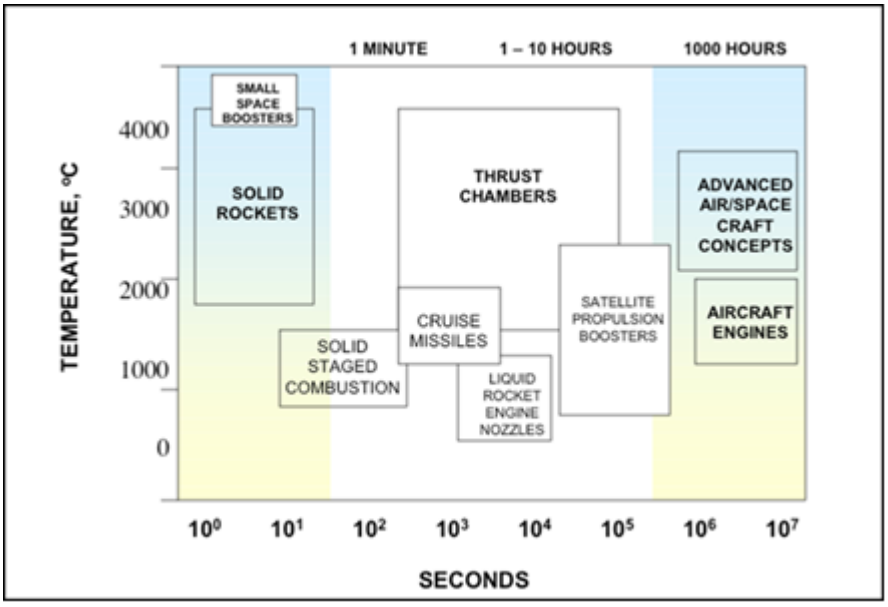

Figure 1.4. Life expectancy of the materials used at the moment in propulsion engines.

The materials for applications at very high temperatures (ultra-high temperature materials or UHTMs) must be light and very stable physically and chemically in reactive atmospheres over 1600 °C. Refractory ceramic materials appear to be the only candidates able to fulfill these requirements in cyclic and/or prolonged conditions, for which reason there is at the present time an unprecedented demand for "ultra-high temperature ceramics" (UHTCs). This has motivated a boom in research aimed at improving the high temperature

performance of some well-known ceramic compounds and at searching for new candidates that promise a better combination of properties. The initial list of ultra-high temperature ceramics was very short. It included ZrC, HfC, and HfN, but the three have problems because they oxidize without forming protective scales at lower temperatures than 1800 °C [8]. Alloys of Hf-Ta were also investigated and discarded in spite of having an acceptable resistance to oxidation because of the limitations imposed by their "low" melting point of only 2000 °C [1, 9-11]. The materials of the Ir-C system are too expensive, and in addition are insufficiently refractory due to the existence of a eutectic point at 2296 °C [12-14]. The compounds of SiO_2 doped with W have too much susceptibility to thermal shock and deform by viscous flow. The oxide ceramics have also been discarded because, although they are intrinsically resistant to oxidation, they have little resistance to thermal shock and creep, and have low thermal conductivities and high coefficients of expansion [15, 16]. The compounds of C-C, C-SiC, and SiC-SiC have very attractive mechanical properties at ultra-high temperatures, but very little resistance to oxidation. Coatings resistant to oxidation do not have much interest because they delaminate due to the difficulty in matching the thermal expansion coefficients with the substrate.

Although all these options have been frustrated, research done in the last few years has allowed the identification of the diborides of metals of the IVb group (i.e., Zr, Hf, and Ta) as the most promising UHTCs [17-19] . This is because they are all highly refractory materials (melting points > 3000 °C), hard (hardnesses > 20 GPa), light (densities < 10 $g \cdot cm^{-3}$), resistant to thermal shock, "good" thermal conductors (conductivities > 50-100 $W \cdot m^{-1} \cdot K^{-1}$ in the temperature range 25-2000 °C), and in addition present great mechanical

resistance above 1500 °C. The most extensively investigated of these three materials is zirconium diboride (ZrB_2), probably because it is the lightest and cheapest. It crystallizes in the hexagonal system (space group P6/mmm, with lattice parameters of a = 3.169 Å and c = 3.531 Å), and has a melting point around 3300 °C, density of 6.1 g cm^{-3}, elastic modulus greater than 420 GPa, hardness greater than 20 GPa, a high thermal conductivity of approximately 134 $W \cdot m^{-1} \cdot K^{-1}$ at 2030 °C, and a thermal expansion coefficient of $8 \cdot 10^{-6}$ K^{-1} in the temperature range 25-2200 °C [20].

While ZrB_2 combines a series of physico-chemical properties of great interest for applications at ultra-high temperatures, it has two serious disadvantages that limit its enormous potential. On the one hand, its high melting point forces one to use very high sintering temperatures and pressures (> 2000 °C and 50 MPa) to make relatively dense materials (> 90% of theoretical density) [21]. And on the other hand, it is a non-oxide compound, and therefore tends to oxidize in prolonged and/or cyclic exposures at high temperatures. Indeed, ZrB_2 has been suggested to oxidize forming ZrO_2 and a boron glass that is highly volatile and hence does not provide any protective barrier to further oxidation [22]. It is therefore understandable that research on ZrB_2 has centred on trying to resolve these two drawbacks.

Previous studies have shown that the incorporation and dispersion of SiC particles in a matrix of ZrB_2 increases its hardness and resistance to oxidation, simultaneously with facilitating its densification [23-25]. The increase of hardness is because the grains of SiC are much harder than those of ZrB_2 (35 GPa as against 25 GPa). The explanation given for the greater resistance to oxidation is that SiC oxidizes to form SiO_2 which combines with the boron glass originated in neighbouring grains of ZrB_2 to finally form a far more

refractory borosilicate glass. With the subsequent evaporation of boron, this glass is transformed into one of silica that completely vitrifies the surface, thus providing better protection against oxidation. Due to the interest in the presence of precursors of SiO_2 to improve the resistance to oxidation of ZrB_2, the incorporation of particles of silicates of Ta, Nb, W, Cr, Mo, and Zr has been tested [26-30]. The materials and procedures used for their manufacture have, however, been very different. The absence of a common experimental platform has meant that it has been impossible to draw reliable guidelines for processing that would allow progress in the design of ZrB_2 ceramics for ultra-high temperatures. Another factor that makes this task difficult is that there exist no thermodynamic and kinetic models that explain the oxidation process, and which hence would allow one to predict the behaviour in as yet untested situations. There is also the aspect still to investigate of the influence of the powder preparation routine on the sinterability of the UHTCs. Indeed, it is widely-accepted that these are precisely the greatest obstacles to the development and implementation of UHTCs.

As was mentioned above, it has been observed that the incorporation of SiC particles improves the densification of ZrB_2. These results are surprising given that the melting point of SiC is around 3000 °C and that it is a compound which is very difficult to sinter. Indeed, the active mechanism of densification in compounds of ZrB_2/SiC has still not been identified (nor in other systems with ZrB_2). Curiously, neither has this fact been used to try to reduce the temperatures and/or pressures of sintering with respect to pure ZrB_2. Evidently, the absence of models of sintering and microstructure evolution prevents the optimization of the process of manufacture of these ceramics, at the same time as making it difficult to search for alternatives to

SiC which would give a better and faster densification of ZrB_2 (logically without loss of resistance to oxidation). This would without doubt mean an authentic revolution in the field of processing of ultra-high temperature resistant ceramics.

Most studies on pure or doped ZrB_2 have centred exclusively on investigating resistance to oxidation and properties. While these aspects are without doubt essential for applications to ultra-high temperatures, very little attention has been paid to the densification of these materials in spite of the importance of that aspect to ensure the use of dense components under service conditions. Thus, there is a lack of systematic sintering studies as a function of the processing variables and of the conditions of the starting powders.

The present Ph.D. Thesis is aimed at trying to cover some of the gaps in ZrB_2 knowledge. In particular, the aim is to develop at lower cost new ZrB_2 ceramics with a wide variety of different microstructures, by means of the suitable control of the fabrication process. The specific objective is indeed the study of the mechanisms of densification in the ZrB_2 ceramics without and with SiC addition. In order to reach this objective, systematic spark-plasma sintering experiments will be carried out, modifying in a controlled form by high-energy ball-milling the characteristics of ZrB_2 powders and also altering the content of SiC. The resulting microstructures of these sintering experiments will be characterized by means of a broad combination of techniques, and analysed in the context of the models of sintering of ceramic materials.

REFERENCES

1) Opeka, M. M., Talmy, I. G. and Zaykoski, J. A., Oxidation-based materials selection for 2000 °C + hypersonic aerosurfaces: Theoretical considerations and historical experience. J Mater Sci. 2004;39:5887-904.

2) Monteverde, F., Bellosi, A. and Luigi Scatteia., Processing and properties of ultra-high temperature ceramics for space applications. Mater Sci Eng A. 2008;485:415-21.

3) Gasch, M. J., Ellerby, D. T. and Johnson, S. M., Ultra high temperature ceramic composite. Handbook for Glass, Ceramics and Composites. ASTM, 2004.

4) https://es.globedia.com/nasa-vende-losetas-transbordador.html.

5) http://history.nasa.gov/SP-4302/ch2.8.html.

6) https://space-station-shuttle.blogspot.com.

7) Fahrenholtz, W. G. Ultra-high temperature ceramics-An introduction to ultra-high temperature ceramics.

8) Vottovich, R. F. and Pugach, É. A., High-temperature oxidation of ZrC and HfC. Powder Metall Met Ceram. 1973;12:916-21.

9) Zhou, Y-L., Niinomi, M. and Akahori, T. Changes in mechanical properties of Ti alloys in relation to alloying additions of Ta and Hf. Mater Sci Eng A. 2008;484:153-6.

10) Sha, J. B. and Yamabe-Mitarai, Y. Saturated solid-solution hardening behavior of Ir-Hf-Nb refractory superalloys for ultra-high temperature applications. Scripta Mater. 2006;54:115-9.

11) Gasch, M. and Johnson, S. Physical characterization and arcjet oxidation of behavior of Ir-Hf-Nb refractory superalloys for ultra-high temperature applications. Scripta Mater. 2006;54:115-9.

12) Wu, W., Chen, Z., Cheng, H., Wang, L. and Zhang, Y. Tungsten and iridium multilayered structure by DGP as ablation-resistance coatings for graphite. Appl Surf Sci. 2011;257:7295-304.

13) Meier, G. H. and Pettit, F. Z. The oxidation behavior of intermetallic compounds. Mater Sci Eng A. 1992;153:548-560.

14) O´Neill, H. St. C., Berry, A. J. and Eggins, S. M. The solubility and oxidation state of tungsten in silicate melts: Implications for the comparative chemistry of W and Mo in planetary differentiation processes. Chem Geol 2008;255:346-359.

15) Kaufman, L. and Nesor, H. Stability characterization of refractory materials under high velocity atmospheric flight conditions. Technical Report AFML-TR-69-84, Part III, 3, 1970.

16) Buckley, J. D. and Edie, D. D. Carbon-carbon materials and composites. Noyes Publications, 1993.

17) Peshev, P., Bilznakov, G. and Leyarovska, L. On the preparation of some chromium, molybdenum and tungsten borides. J Less-Common Metals. 1967;13:241-7.

18) Juretschke, H. J. and Steinitz, R. Hall effect and electrical conductivity of transition-metal diborides. J Phys Chem Solids. 1958;4:118-27.

19) Inkson, B. J., Boothroyd., C. B. and Humphreys, C. J. Borides morphology in A (Fe, V, B) Ti-Al alloy containing B_2-phase. Acta Metall Mater. 1995;43:1429-38.

20) Narottam P. Bansal. Handbook of ceramic composite, USA: Kluwer Academic Publishers;2005.

21) Guo, S-Q., Nishimura, T., Kagawa, Y. and Yang., J-M. Spark plasma sintering of zirconium diborides. J Am Ceram Soc. 2008;91:2848-55.

22) Parthasarathy, T.A., Rapp, R. A., Opeka, M. and Kerans., R. J. A model for the oxidation of ZrB_2, HfB_2 and TiB_2. Acta Mater. 2007;55:5999-6010.

23) Zimmermann, J. W., Hilmas, G. E., Fahrenholtz, W. G. Thermal shock resistance of ZrB_2 and ZrB_2-30%SiC. Mater Chem and Phys. 2008;112:140-5.

24) Zhu, S., Fahrenholtz, W. G. and Hilmas, G. E. Enhaced densification and mechanical properties of ZrB_2-SiC processed by a preceramic polymer coating route. Scripta Mater. 2008;59:123-6.

25) Ogata, T., Mori, T., Nakamura, K., Kobayashi, K. and Kuwijinma, H. Mechanical properties of particulate dispersed and SiC whisker reinforced boride composite materials by hot pressing. Proceeding satellite symposium. Advanced structural inorganic composites 7th Int. meeting on Modern Ceramics Thecnologies. Motecatini Terme, 27-30 June, 1990, 235-43.

26) Sorrell, C. C., Stubican, V. S. and Bradt, R. C. Mechanical properties of ZrC-ZrB_2 and ZrC-Tib_2. Directionally solidified eutectics. J Am Ceram Soc. 1986;69:317-21.

27) Venkateswaran, T., Basu, B., Raju, G. B., Kim, D-Y. Densification and properties of transition metal borides-based cermets via spark plasma sintering. J Eur Ceram Soc. 2006;26:2431-40.

28) Mroz, C. Processing and properties of microcomposite TiZrC and $TiZrB_2$ materials. Ceram Eng Sci Proc. 1993;14:725-35.

29) Moryiama, M., Aoki, H. and Kobayashi, Y., Fabrication and mechanical properties of hot pressed TiB_2-ZrB_2 ceramic system. J Ceram Soc Jap. 1998;106:1196-200.

30) Jin, Z., Zhang, G., Bao, Y., Bai, C., Yue, X. and Zhao, H., Size effect of strengthened particles of ceramic Composites. J Chin Ceram Soc. 1995;23:610-7.

"Nothing is too wonderful to be true, if it be consistent with the laws of nature"

Michael Faraday (1791-1867)

Chapter II: Crystallite Size Refinement of ZrB_2 by High-Energy Ball-Milling in the Presence of SiC

2.1. MOTIVATION

The ultra-high-temperature ceramic (UHTC) ZrB_2 is currently being actively investigated as an aerospace material for extreme environments such as those encountered in hypersonic flights, atmospheric re-entry, and rocket propulsion. However, ZrB_2 is not only hard to sinter [1,2], but also by itself does not meet all the exigent requirements of oxidation resistance and mechanical properties demanded by extreme-environment aerospace engineering [1,2]. For these reasons, ZrB_2 is typically combined with other refractory ceramics. One of the most widely used is SiC at relative concentrations between 5 and 30 vol.% [1,2]. The benefit of adding SiC to ZrB_2 is threefold. Firstly, SiC acts as a sintering aid, facilitating densification at lower temperatures. This is attributed to the fact that the surface of the SiC particles is irremediably covered by a thin film of SiO_2 that promotes liquid-phase sintering [3]. Secondly, SiC provides ZrB_2 with greater oxidation

and ablation resistance because the borosilicate scales resulting from the simultaneous oxidations of ZrB_2 and SiC are much more protective than the boria scales resulting from the oxidation of ZrB_2 alone [1,2]. Thirdly, SiC improves the thermo-mechanical properties relevant for the aerospace applications proposed for ZrB_2 [1,2]. For example, the hardness increases because SiC is harder than ZrB_2, the toughness improves because of the crack defection and crack-wake bridging in the weak ZrB_2-SiC interfaces, the strength increases because SiC inhibits grain growth thus reducing the dominant initial flaw size, and finally, the thermal shock resistance also improves since SiC increases the strength and thermal conductivity, and lowers the elastic modulus of the composite. It is not surprising therefore that more research effort is being devoted to the development of ZrB_2+SiC UHTCs than of ZrB_2 UHTCs.

Current practice in preparing the powder mixtures required for the fabrication of ZrB_2+SiC UHTCs typically involves attrition or planetary milling in wet conditions of the ZrB_2 and SiC starting powders either together or separately (in the latter case, there is a later additional step of homogenization) for 24 h or more to refine the particle sizes, followed by drying the slurries [3-16]. This approach results in sinterable, homogeneous mixtures of ZrB_2 plus SiC powders, but with sub-micrometre particle sizes (i.e., ~0.5 μm) because under these operating conditions attrition or planetary milling is a form of conventional milling. While the benefits of this processing strategy over the use of pure ZrB_2 are indisputable, the processing routine would be markedly simplified and the sinterability would be further improved if the ZrB_2 and SiC powders were refined together directly down to nanoscale. This cannot be achieved by conventional ball-milling, however, because the

stresses generated are not high enough to fracture fine particles. Recently, it has been shown that high-energy ball-milling (HEBM) in dry conditions with shaker millers can produce ultrafine agglomerates (i.e., ~120 nm) of nano-particles (i.e., ~15 nm) from pure ZrB_2 powders in a few hours [17]. But the procedure is not directly extrapolatable to mixtures of ZrB_2 and SiC powders because it is unknown whether the addition of a second phase such as SiC affects the HEBM comminution mechanism of ZrB_2 or its kinetics. This therefore was the target of the present study which is aimed at comparing the HEBM behaviour of ZrB_2 without and with different additions (5, 17.5, and 30 vol.%) of SiC. We found that ZrB_2 is not immune to the presence of SiC, and discuss the implications that this has for the preparation of nano-powders of ZrB_2 plus SiC.

2.2. EXPERIMENTAL PROCEDURE

2.2.1. Processing

Commercially available powders of ZrB_2 and SiC (in both cases Grade B of H.C. Starck, Berlin, Goslar, Germany) were used as starting materials. The SiC is of type α, in particular, essentially the 6H polytype [18]. The two as-purchased powders have a >99.5% purity, and consist of single-crystal particles with an average size of ~2 μm in the case of ZrB_2 and ~0.55 μm in the case of SiC. Four powder compositions were prepared: pure ZrB_2, and ZrB_2 plus 5, 17.5, and 30 vol.% SiC (abbreviated henceforth as ZrB_2-x%SiC, where x refers to the vol.% SiC content). The HEBM of the pure ZrB_2 powders and of the three ZrB_2+SiC powder mixtures was performed using a

shaker mill (Spex 8000D, Spex CertiPrep, Metuchen, United States) equipped with cylindrical hardened-steel containers loaded with 5 WC balls of 6.7 mm in diameter. The milling was carried out by shaking the containers at about 1060 back-and-forth cycles per minute in a complex three-dimensional trajectory, under the following conditions: ball-to-powder weight ratio of 4, and milling times in the range 1-180 min in air to impart different degrees of milling intensity.

2.2.2. Microstructural Characterization

The as-purchased and ball-milled powders were characterized using X-ray diffractometry (XRD), laser scattering (LS), and field-emission scanning electron microscopy (FE-SEM). The XRD was used to identify the phases present, to determine the phase composition in selected cases, and to evaluate the crystallite size of ZrB_2 as a function of the ball-milling condition. The phase identification was performed by indexing the XRD patterns with the aid of the PDF2 database. The phase composition was determined quantitatively by Rietveld analysis of the XRD patterns, using the commercial software package Topas (Topas 4.1, Bruker AXS, Karlsruhe, Germany) [19]. The crystallite sizes of ZrB_2 were evaluated by applying the variance method [20] to its 101 peak. This peak was chosen because it is the most intense one of ZrB_2, and does not overlap with any SiC peak. The crystallite size of SiC in the ZrB_2+30%SiC mixture was evaluated from its 103 peak, which is intense, does not overlap with any ZrB_2 peak, and is located near the 101 peak of ZrB_2. The XRD data were collected in step-scanning mode with monochromatic $CuK\alpha_1$ radiation (λ=1.54183 Å), using a high-resolution laboratory diffractometer (D8 Advance, Bruker AXS, Karlsruhe, Germany) and the following three

acquisition conditions: (1) scanning in the range 20-80° 2θ, step width 0.016° 2θ, and count time 3 s/step which was used to identify the phases present, (2) scanning in the range 39.5-44.5° 2θ, step width 0.016° 2θ, and count time 5 s/step which was used to evaluate the ZrB_2 crystal sizes, and (3) scanning in the range 36.5-39.5° 2θ, step width 0.016° 2θ, and count time 15 s/step which was used to evaluate the SiC crystal sizes. The LS was used to determine the particle sizes in the powders, with the analyzer employed being equipped with red and blue light sources (Mastersizer 2000, Malvern Instruments, Worcestershire, United Kingdom). These determinations were performed in quintuplicate. The FE-SEM was used to examine the particle morphology, and to validate the particle and crystallite sizes measured by LS and XRD, respectively. The observations were made without metal coating, at 10 kV with secondary electrons, using a field-emission microscope (S4800-II, Hitachi, Ibarakiken, Japan). The XRD, LS, and FE-SEM specimens were prepared using routine methods applicable to ceramic powders.

2.3. RESULTS

Figure 2.1 shows XRD patterns of the pure ZrB_2 powders and of the ZrB_2+30%SiC mixture before and after HEBM for selected times. Since the XRD patterns of the ZrB_2+5%SiC and ZrB_2+17.5%SiC mixtures showed the same trends as those that will now be discussed for the extreme cases of the pure ZrB_2 powder and the ZrB_2+30%SiC mixture, they will not be presented for the sake of brevity. It can be seen in Fig. 2.1 that the XRD peaks are increasingly broader and lower with increasing HEBM time. Because of the absence of severe plastic deformation in the brittle ZrB_2 and SiC [17,21], the

broadening and collapse of the peaks indicate that HEBM progressively refines the crystallite sizes. It can also be seen in Fig. 2.1 that the XRD peaks do not shift from their position in the un-milled condition, indicating that HEBM neither alters the crystal structures nor forms solid solutions between the ZrB_2 and SiC in the case of the ZrB_2+SiC mixtures.

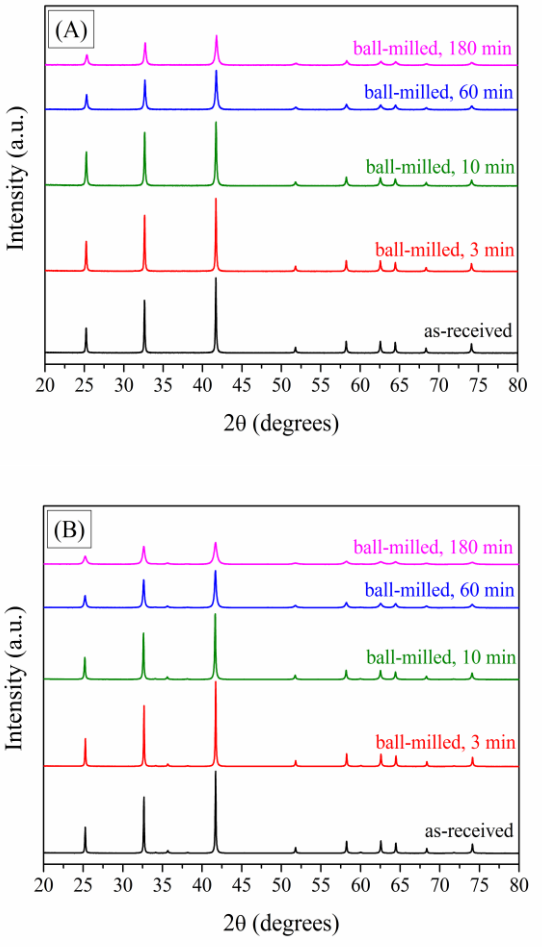

Figure 2.1. XRD patterns of (A) the ZrB_2 powders and of (B) the ZrB_2 powders with 30 vol.% of SiC before and after HEBM for selected times.

Finally, in Fig. 2.2 one observes that the XRD patterns after 180 min of HEBM exhibit WC peaks, indicating contamination of the powders by the milling media at some time between 60 and 180 min of HEBM. The level of contamination is very low, however, with the Rietveld analysis of the XRD patterns (included in Fig.2.2) showing that the WC content after 180 min of HEBM is less than 2.5 wt.%. This minute contamination by WC had been not observed in previous studies of HEBM on ZrB_2 [17,22], and was probably detected in the present study thanks to the use of a high-resolution diffractometer. The contamination by WC, however, should not be interpreted as a negative aspect because WC itself is a sintering additive of ZrB_2 [23].

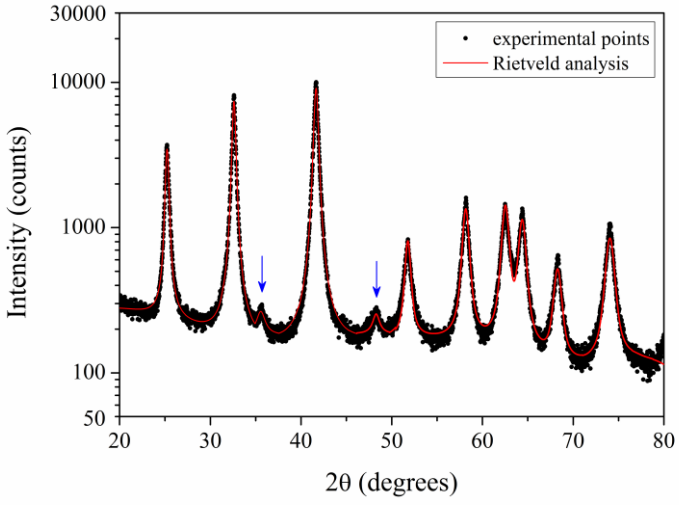

Figure 2.2. XRD pattern of the ZrB_2 powder after 180 min of HEBM, together with the corresponding Rietveld analysis. The WC peaks free of overlap with ZrB_2 peaks are marked with arrows. The logarithmic scale is to facilitate the appreciation of the WC peaks.

Figure 2.3 shows the average crystallite size of ZrB_2 as a function of the HEBM time in the powders milled in the pure state and co-milled with SiC (5, 17.5, or 30 vol.%). It can be seen that the evolution of the crystallite size with HEBM time is qualitatively similar in all cases, i.e., the crystallite size first decreases rapidly, then much more gradually, and finally tends asymptotically towards a certain limiting value. It is also very evident in Fig. 2.3, however, that ZrB_2 crystals are refined more slowly when they are co-milled with SiC, an effect that becomes more pronounced with increasing SiC load in the ZrB_2+SiC mixture.

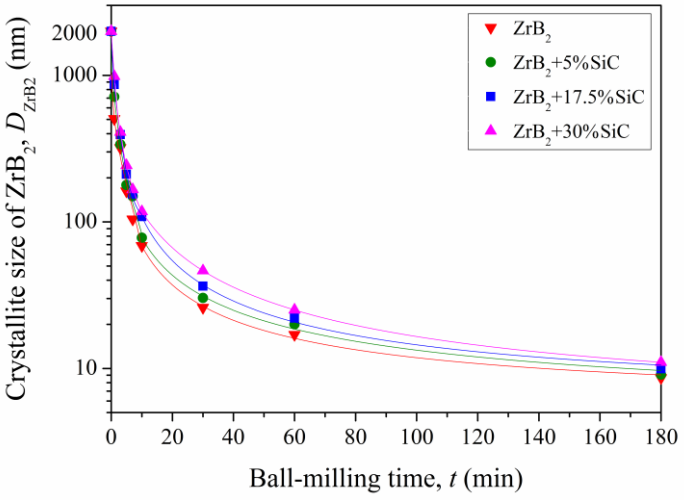

Figure 2.3. Average crystallite size of ZrB_2 as a function of HEBM time for the ZrB_2 powders ball-milled without and with SiC (5, 17.5, and 30 vol.%). The solid lines are to guide the eye. The crystallite size in the as-purchased condition was taken to be the same as the particle size.

Thus, for example, using the expression $D = Kt^{2/3}$ to model the dependence of crystallite size on the HEBM time [24,25], the constant K is found

to be 513±30 nm•min$^{2/3}$ for the ZrB_2 powder without SiC, and 672±34, 807±43, and 903±51 nm•min$^{2/3}$ for the powders with 5, 17.5 and 30 vol.% SiC, respectively. The addition of SiC, however, did not alter the limiting crystallite size because if the curves are extrapolated to longer HEBM time, they all appear to converge at ~5 h of ball-milling at a crystallite size of ~7-8 nm. Finally, the ZrB_2 crystallites are in all cases free of lattice microstrains and have the same lattice parameters as in the as-received condition because the XRD analysis revealed no signs of Gaussian peak broadening or peak shifting.

Figure 2.4 compares FE-SEM images of the typical particles in the pure ZrB_2 powder milled for short and long times. One observes in Fig. 2.4.A that the particle size of the starting powder (~2 μm) is rapidly reduced to the sub-micrometre scale in less than 1 min of HEBM, and that the powder particles have faceted surfaces. Furthermore, as in the case shown in this Fig. 2.4.A, some of these particles contain cracks. After long-term HEBM (Fig 2.4.B), the morphology of the powder particles has evolved towards smooth-surfaced of nano-particles (i.e., < 20 nm) that form ultrafine (i.e., < 200 nm in size) agglomerates. Furthermore, TEM observations performed by us in previous studies of HEBM on ZrB_2 (not repeated here) have shown that these agglomerates are indeed porous and that their primary nano-particles are crack-free [17]. Finally, the fact that these agglomerates are strong, because they have survived the ultrasonic bath, reveals the occurrence of cold welding. Cold-welding during HEBM is a well-known phenomenon, and is typical but not exclusive of ductile compounds [24,26]. Indeed, despite the brittleness of ZrB_2, cold-welding occurs for long HEBM times because nano-particles behave in a more ductile fashion, and there is a local

temperature spike at the collision site (~300-500 °C) with the presence of high compressive stresses (~6 GPa) of very short duration (of the order of 10^{-6}-10^{-5} s) [26].

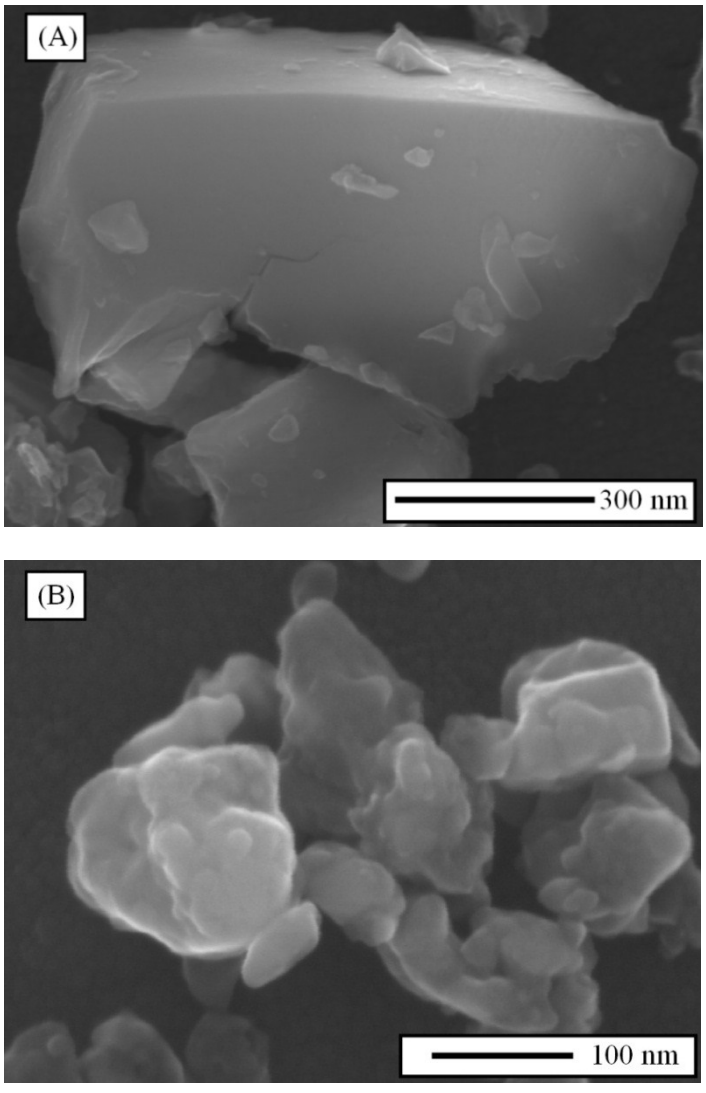

Figure 2.4. FE-SEM images of the ZrB_2 powder particles after HEBM for (A) 1 min and (B) 180 min.

Figure 2.5 shows FE-SEM images of the typical particles in the ZrB_2+30%SiC mixture milled for only 1 min. Unlike the pure ZrB_2 powder, the ZrB_2+30%SiC mixture consists of two distinct types of particle, one of sub-micrometre sizes (Fig. 2.5.A) and the other of nanometre sizes (Fig. 2.5.B). The extensive FE-SEM observations showed the sub-micrometre particles to be very abundant, to typically have sizes ranging from 1 to 0.3 μm, to have faceted surfaces, and (as in the case shown) to sometimes contain cracks. They also indicated that the less abundant nano-particles are smaller than 100 nm, have rounded surfaces, and are randomly distributed between the sub-micrometre particles. The EDS analysis performed during the FE-SEM examinations revealed that in general the sub-micrometre particles are ZrB_2 and the nano-particles are SiC. There are also some small ZrB_2 particles with angular shapes. These are fracture debris of the larger ZrB_2 particles. As in the case of the pure ZrB_2 powder, the FE-SEM image in Fig. 2.6 shows that long-term HEBM also changes the morphology of the particles in the ZrB_2+30%SiC mixture to strong agglomerates that have much finer, rounded particles which are cold-welded in their interior. When ZrB_2 is co-milled with SiC, these agglomerates are somewhat smaller, and their primary particles are somewhat larger. Thus, the addition of SiC slows down the kinetics of crystallite size refinement (see Fig. 2.3) and minimizes the cold-welding of the ZrB_2 particles during HEBM. Furthermore, the EDS analysis of the agglomerates in the ZrB_2+30%SiC powder mixture showed the predominance of Zr accompanied by smaller amounts of Si. This chemical analysis result was found to be quite reproducible from one agglomerate to other. These observations, together with the previous XRD analysis that ruled out the formation of solid solutions, indicate that these agglomerates are composed of

individual nano-particles of ZrB_2 and SiC homogeneously mixed at a nanometre scale.

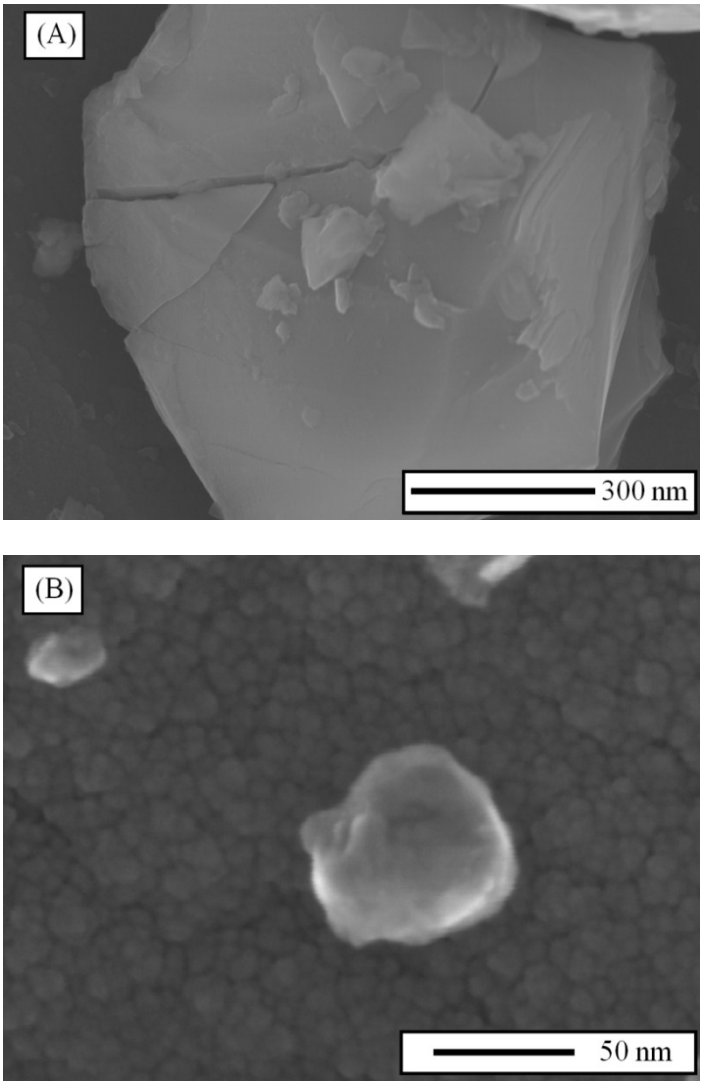

Figure 2.5. FE-SEM images of the powder particles in the ZrB_2 powder with 30 vol.% of SiC after HEBM for 1 min showing the presence of (A) micrometre-sized particles (ZrB_2) and (B) nano-particles (SiC).

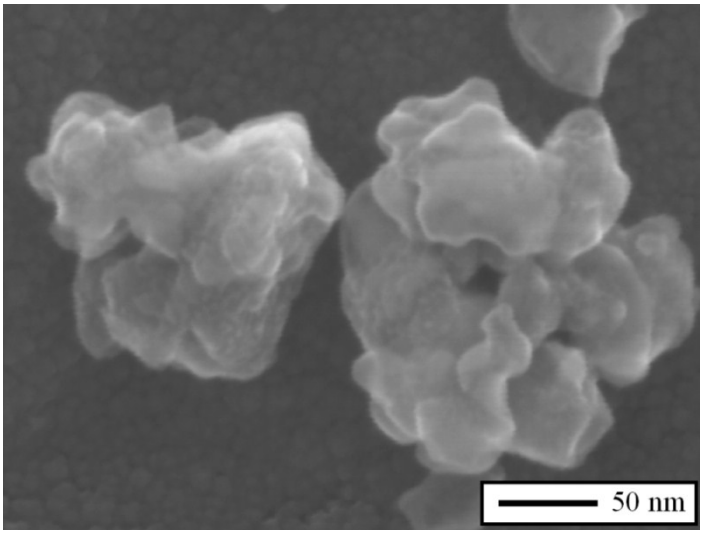

Figure 2.6. FE-SEM images of the powder particles in the ZrB_2 powder with 30 vol.% of SiC after HEBM for 180 min.

Figure 2.7 shows the average size of the particles as a function of the HEBM time in the powders milled in the pure state and co-milled with SiC (5, 17.5. or 30 vol.%). There are various interesting features in this figure. Firstly, the evolution of the particle size is substantially different in the powders milled with and without SiC. In the case of the pure ZrB_2 the particle size first decreases, then increases, and finally stabilizes, whereas in the ZrB_2+SiC mixtures the particle size decreases continuously. Secondly, the particle sizes determined by LS in the ZrB_2+SiC mixtures at the early stages of HEBM are smaller than the crystallite sizes of ZrB_2 measured by XRD, unlike the case of the pure ZrB_2 powder. Furthermore, the particle sizes in the ZrB_2+SiC mixtures do not follow the increasing trend of the crystallite sizes with increasing the SiC loading shown in Fig. 2.3. The clear explanation of these two observations is that at short HEBM times the SiC particles are much

smaller than the ZrB_2 particles (i.e., nanometre vs sub-micrometre sizes; Figs. 2.4.A and B), and that LS measures the contributions from both ZrB_2 and SiC whereas XRD distinguishes them. Thirdly, LS always yields far larger sizes than XRD in the late stages of HEBM. This is simply due to the formation of hard agglomerates, as was observed by FE-SEM (Figs. 2.3.B and 2.5). The LS data thus confirm the occurrence of cold-welding during HEBM in all cases, and also show it to be much less severe with increasing SiC content (ultimate agglomerate sizes of 160, 120, 115, and 90 nm for SiC loads of 0, 5, 17.5, and 30%, respectively).

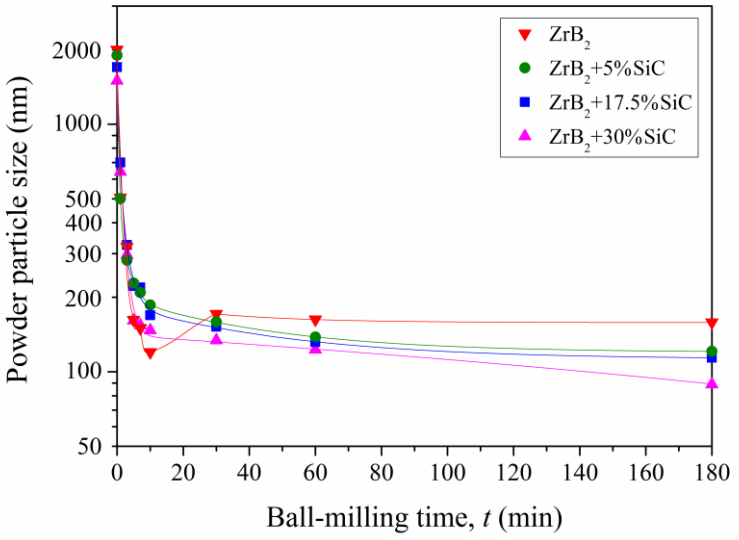

Figure 2.7. Average powder particle size as a function of HEBM time for the ZrB_2 powders ball-milled without and with SiC (5, 17.5, and 30 vol.%). The solid lines are to guide the eye.

2.4. DISCUSSION

The XRD, FE-SEM, and LS results presented above demonstrate that the behavior of the crystallite size refinement of ZrB_2 has been altered by the presence of SiC. Specifically, high-energy co-ball-milling of ZrB_2 with SiC does not change the mechanism of crystallite size refinement, but slows down its kinetics. This conclusion is inferred from the fact that the crystallite size curves of ZrB_2 in Fig. 2.3 all obey the same functional dependence on HEBM time (i.e., $D = Kt^{2/3}$), but with the constant K increasing with the SiC content. The mechanism is repeated brittle fracture followed by cold-welding, as revealed by the following experimental observations: (i) the rapid refinement in the early stages of HEBM and the existence of a limiting crystallite size, (ii) the faceted shape and the cracks in the powder particles at short HEBM times, (iii) the absence of lattice microstrains in the interior of the crystals throughout the HEBM that rules out severe plastic deformation, and (iv) the formation of strong agglomerates containing primary nano-particles in the late stages of HEBM. Although SiC does not change the mechanism of crystallite size refinement, it does have two distinct effects: (i) reducing the rate of crystallite size refinement and, (ii) promoting the formation of finer agglomerates. The former phenomenon is a surprise to us because it is not what we would have expected. Previous studies [22,27] have revealed that adding a softer material during ball-milling slows down the crystallite size refinement of the harder material because the softer material can act as a lubricant. When a harder material is added, such as adding SiC to Al, the crystallite size refinement of the softer material accelerates substantially due to the increased severe plastic deformation of the softer material induced by the presence of many harder material particles [28,29]. SiC is harder than ZrB_2; however, as

shown in this study, it does not accelerate the crystallite size refinement of ZrB_2, indicating that a new mechanism is present for the ZrB_2+SiC mixture. This new mechanism is discussed below.

One of the possible mechanisms for the unexpected effect of SiC discussed above is the reduced ball-to-powder volume ratio with the addition of SiC to ZrB_2. We have shown in an earlier study [17] that the crystallite size refinement of pure ZrB_2 is slower when the ball-to-powder weight ratio is reduced from 4 to 2, equivalent to ball-to-powder volume ratios of 1.6 and 0.8, respectively. Using the ball-to-powder weight ratio of 4, the total volume of the WC balls, and the density values of ZrB_2 (6.1 $g \cdot cm^{-3}$) and SiC (3.21 $g \cdot cm^{-3}$) together with their concentrations, one calculates the ball-to-powder volume ratio to be 1.6, 1.56, 1.35, and 1.33 for the pure ZrB_2 powder and the ZrB_2+5%SiC, ZrB_2+17.5%SiC, and ZrB_2+30%SiC mixtures, respectively. This straightforward calculation shows that the ball-to-powder volume ratio decreased with increasing SiC concentration in the ZrB_2+SiC mixture simply because we maintained the ball-to-powder weight ratio fixed at 4 and ZrB_2 is denser than SiC. It might then be argued that the slower crystallite size refinement of ZrB_2 with increasing SiC concentration in the ZrB_2+SiC mixtures is due simply to this decrease in the ball-to-powder volume ratio, thereby reducing the effective compressive stresses applied to the individual particles during HEBM. However, as shown in Fig. 2.8, when one compares the data of crystallite size as a function of HEBM time for the pure ZrB_2 ball milled with a ball-to-powder volume ratio of 0.8 [17] and the ZrB_2+30%SiC ball-milled with a ball-to-powder volume ratio of 1.33, one finds that the kinetics of crystallite size refinement is slightly slower for the latter despite the fact that the ball-to-powder volume ratios is much higher (i.e., 67%

higher). Thus, this comparison clearly rules out the mechanism of reducing the ball-to-powder volume ratio played by SiC.

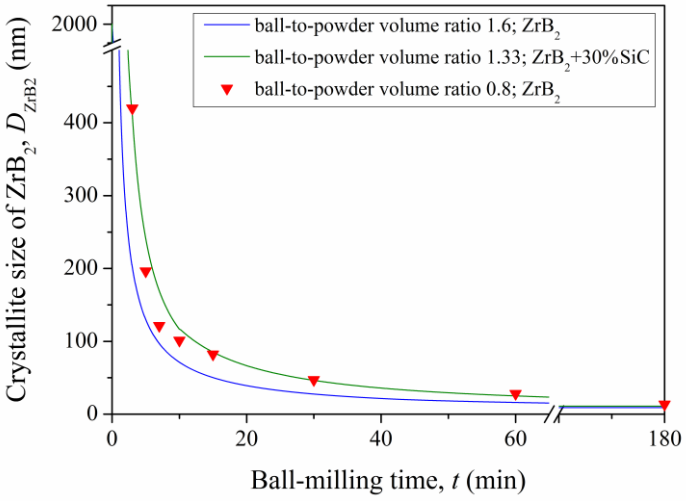

Figure 2.8. Average crystallite size of ZrB_2 as a function of HEBM time for the ZrB_2 powders ball-milled without SiC using ball-to-powder volume ratios of 1.6 and 0.8, and with 30 vol.% of SiC using a ball-to-powder volume ratio of 1.33.

Another possible mechanism for the unexpected effect of SiC is the reduction of the crystallite size refinement rate through the direct role played by SiC. A previous study [22] has shown that the slower kinetics of crystallite size refinement during the HEBM of ZrB_2 can be achieved in the presence of 2 wt.% graphite. This phenomenon has been attributed to the lubricating effect of the graphite on the contacts between the ZrB_2 particles themselves as well as between the particles and the colliding balls. Thus, SiC may, like graphite, also "lubricate" the contacts during the HEBM of ZrB_2. However, unlike graphite, SiC has no lubricating properties by itself, and the

coefficients of friction of SiC and ZrB_2 in dry air are very similar (~0.8) [30,31]. Therefore, the "lubrication" mechanism has necessarily to be different. The evidence obtained by FE-SEM (Fig. 2.5.B) suggested that this mechanism may well be closely related to the nanoscale size of SiC. We therefore monitored by XRD the evolution of the SiC crystals in the ZrB_2+30%SiC mixture throughout the HEBM, and compared it with that of the ZrB_2 crystals in the same mixture (Fig. 2.9)[a]. It can be seen that the general trend is

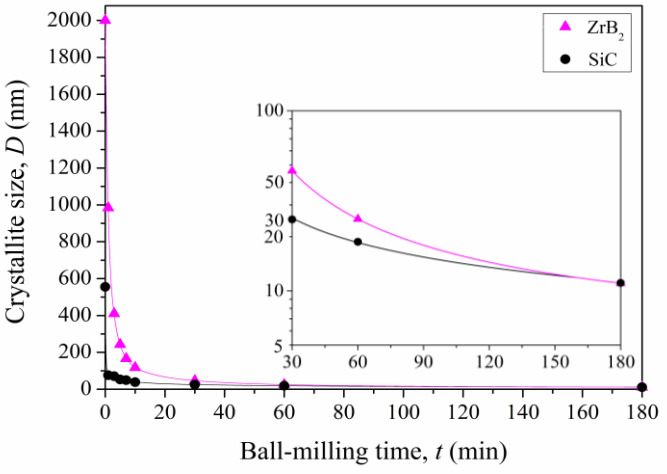

Figure 2.9. Average crystallite size of ZrB_2 and SiC as a function of HEBM time for the ZrB_2 powders ball-milled with 30 vol.% of SiC. The solid lines are to guide the eye. The inset is a detail of the region of long-duration HEBM.

qualitatively similar, and can also be described by the expression $D = Kt^{2/3}$ because the mechanism of crystal size refinement is the same in SiC as in ZrB_2.

[a] The choice of the ZrB_2+30%SiC mixture powder for this purpose was simply because the greater SiC content facilitates the precise modeling of the SiC XRD peaks required to accurately calculate its crystallite size.

However, the crystallite size refinement of SiC is much faster than that of ZrB_2, with the constant K being 103±8 nm•min$^{2/3}$ for SiC versus the 903±51 nm•min$^{2/3}$ for ZrB_2. Thus, despite its smaller particle size in the as-purchased condition which would make fracture more difficult, SiC is refined faster than ZrB_2 due to its greater brittleness (K_{IC} of 3 vs 5 MPa•m$^{1/2}$).

The important feature to note in Fig. 2.9 is that the particle size of the SiC starting powder (0.55 μm) is reduced rapidly to below 100 nm in less than 1 min of HEBM, after which the further reduction in crystallite size is very slight. We believe that this early nano-crystallization of SiC is the key to the unexpected effect of SiC. Crystallite size refinement in brittle materials occurs by brittle fracture, and fracture strength scales inversely with the square root of the crystal sizes [32]. This accounts for the $t^{2/3}$ dependence of the crystal size on the HEBM time. At a certain critical HEBM time, the crystals have become small enough, i.e., nanoscale, for the compressive stress imparted during the collisions to fall below the crystals' fracture strength. These nano-crystals, once formed, can no longer be fractured during HEBM, and consequently simply slide past each other because the collisions during the HEBM occur without lateral constraints. In this scenario, the SiC nano-crystals consume collision energy and reduce the compressive stress on ZrB_2 particles. As a result, crystallite size refinement of ZrB_2 slows down and harder SiC appears to have the "lubricating" effect. This energy consumption mechanism is also consistent with the phenomenon of increasing SiC load leading to slower refinement kinetics (Fig. 2.3). The fact that the presence of SiC does not affect the ultimate size of the ZrB_2 crystallites (Fig. 2.3) is also in good agreement with this mechanism because the ultimate size is mainly determined by the

fracture strength of the crystallites and the compressive stress at the collision site.

It is interesting to note that the generation of many SiC nano-particles at the early stage of HEBM is in good accordance with the observation that the more SiC, the finer agglomerates (Fig. 2.7). It is well known that the size of agglomerates is determined by the combined effect of the fracture rate and the cold-welding rate [24]. For pure ZrB_2 the fracture rate is high at the early stage of HEBM, leading to the formation of the smallest agglomerates at about 10-min of HEBM (Fig. 2.7). However, as the HEBM time increases, the fracture rate decreases because smaller particle sizes are more resistant to fracture [32] and the cold-welding rate increases due to the increased number of particles. As a result, the size of agglomerates increases and finally stabilizes as the HEBM time increases beyond 10 min (Fig. 2.7).

For the ZrB_2+SiC mixtures both the fracture rate and the cold-welding rate are altered by SiC. Fundamentally, the extent of cold welding and its rate during HEBM of multiple brittle materials are affected by the chemical affinity between different materials. As evidenced by the smaller agglomerate sizes for all of the ZrB_2+SiC mixtures in comparison with the pure ZrB_2 powder, the present study has revealed that the chemical affinity between SiC and ZrB_2 is lower than that between ZrB_2 themselves at the HEBM temperature. Based on this reasoning, the observed alternation in the agglomerate size as a function of the HEBM time for the ZrB_2+SiC mixtures can be explained as follows. At the early stage of HEBM, the fracture rate of ZrB_2 has been reduced because of the collision energy consumption by frictional sliding of many SiC nano-particles and thus the reduced compressive stress on ZrB_2 particles. The reduced fracture rate results in larger

agglomerate sizes than those observed for the pure ZrB_2 powder at the early stage of HEBM (Fig. 2.7). However, as the HEBM time increases and most of the ZrB_2 particles become very small, the major role of SiC nano-particles changes to minimize cold welding events because of the lower chemical affinity between SiC and ZrB_2 than that between ZrB_2 themselves at the HEBM temperature. As a result, when more SiC is added and thus more SiC nano-particles are trapped at the collision site, fewer ZrB_2 can be cold welded, leading to the phenomenon that the more SiC, the finer agglomerates at the long HEBM time (Fig. 2.7).

Finally, the present study has interesting implications concerning the processing of ZrB_2+SiC UHTCs. Firstly, relative to the conventional attrition milling of ZrB_2+SiC mixtures, the refinement of the primary particle sizes to the nanoscale achieved by HEBM is expected to enhance the subsequent sintering kinetics if powder pressing is conducted properly. Such expected enhancement is due to the reduced diffusion distance and increased interparticle interfaces resulting from the formation of ultrafine agglomerates composed of primary nano-particles. Secondly, the processing routine is simplified notably both by the elimination of steps during the powder batch preparation, and by the time-saving in other steps due to the high-energy co-ball-milling in dry conditions dealing simultaneously with the ZrB_2 refinement and the homogeneous dispersion of the SiC additive at nanometre scale in a few hours. Indeed, these are objectives which have been extensively pursued by the UHTC community.

2.5. SUMMARY

The effect of SiC addition (5, 17.5, and 30 vol.%) on the high-energy ball-milling (HEBM) behaviour of ZrB_2 is investigated. It was found that the presence of SiC during HEBM did not alter ZrB_2 refinement mechanism of repeated brittle fracture followed by cold-welding, thereby leading to the formation of agglomerates consisting of primary nano-particles. SiC did, however, slow down the kinetics of crystallite size refinement and promoted the formation of finer agglomerates. Both of these phenomena became more pronounced with increasing SiC content in the ZrB_2+SiC powder mixtures, and they were attributed to the energy dissipation effect of the nanocrystalline SiC particles during HEBM of the ZrB_2+SiC powder mixture. This study offers the first evidence that the addition of harder materials to softer materials can slow down the refinement of crystallite sizes, and thus provides a new mechanism to control crystallite sizes during HEBM. The simultaneous attainment of nano-particles of ZrB_2 and SiC, reduced agglomerate sizes, and homogeneous SiC dispersion at the nanometre scale may have important implications for the ultra-high-temperature ceramic community, as it simplifies the processing route and is likely to facilitate the sintering of ZrB_2-SiC composites.

2.6. REFERENCES

1) Fahrenholtz, W. G., Hilmas, G. E., Talmy, I. G. and Zaykoski, J. A. Refractory diborides of zirconium and hafnium. J Am Ceram Soc. 2007; 90:1347-64. See also references therein.

2) Guo S-Q. Densification of ZrB_2-based composites and their mechanical and physical properties: a review. J Eur Ceram Soc. 2009;29:995-1011. See also references therein.

3) Hwang, S. S., Vasiliev, A. L. and Padture, N. P. Improved processing and oxidation resistance of ZrB_2 ultra-high temperature ceramics containing SiC nanodispersoids. Mat Sci Eng. 2007; A464:216-24.

4) Chamberlain, A. L., Fahrenholtz, W. G., Hilmas, G. E. and Ellerby, D. T. High-strength zirconium diboride-based ceramics. J Am Ceram Soc. 2004;87:1170-2.

5) Yan, Y., Huang, Z., Dong, S. and Jiang, D. Pressureless sintering of high-density ZrB_2-SiC ceramic composites. J Am Ceram Soc. 2006;89:3589-92.

6) Zhu, S., Fahrenholtz, W. G. and Hilmas, G. E. Influence of silicon carbide particle size on the microstructure and mechanical properties of zirconium diboride-silicon carbide ceramics. J Eur Ceram Soc. 2007;27:2077-83.

7) Zhang, S. C., Hilmas, G. E. and Fahrenholtz, W. G. Pressureless sintering of ZrB_2-SiC ceramics. J Am Ceram Soc. 2008;91:26-32.

8) Monteverde, F., Bellosi, A. and Scatteia, L. Processing and properties of ultra-high temperature ceramics for space applications. Mat Sci Eng. 2008; A485:415-21.

9) Zou, J., Zhang, G-J., Kan, Y-M. and Wang, P-L. Pressureless densification of ZrB_2-SiC composites with vanadium carbide. Scripta Mater. 2008;59:309-12.

10) Zhang, S. C., Hilmas, G. E. and Fahrenholtz, W. G. Mechanical properties of sintered ZrB_2-SiC ceramics. J Eur Ceram Soc. 2009;31:893-901.

11) Watts, J., Hilmas, G., Fahrenholtz, W. G., Brown, D. and Clausen, B. Stress measurements in ZrB_2-SiC composites using Raman spectroscopy and neutron diffraction. J Eur Ceram Soc. 2009;30:2165-71.

12) Zhang, H., Yan, Y., Huang, Z., Liu, X. and Jiang, D. Properties of ZrB_2-SiC ceramics by pressureless sintering. J Am Ceram Soc. 2009; 92:1599-602.

13) Guo, W-M., Zhang, G-J. and Wang, P-L. Microstructural evolution and grain growth kinetics in ZrB_2-SiC composites during heat treatment. J Am Ceram Soc. 2009;92:2780-3.

14) Wang, X-G., Guo, W-M. and Zhang, G-J. Pressureless sintering mechanism and microstructure of ZrB_2-SiC ceramics doped with boron. Scripta Mater. 2009;61:177-80.

15) Zhang, H., Yan, Y., Huang, Z., Liu, X. and Jiang, D. Pressureless sintering of ZrB_2-SiC ceramics: The effect of B_4C content. Scripta Mater. 2009;60:599-62.

16) Zamora, V., Sánchez-González, E., Ortiz, A. L., Miranda, P. and Guiberteau, F. Hertzian indentation of a ZrB_2-30% SiC ultra-high-temperature ceramic up to 800 °C in air. J Am Ceram Soc. 2010;93:1848-51.

17) Galán, C. A., Ortiz, A. L., Guiberteau, F. and Shaw, L. L. Crystallite size refinement of ZrB_2 by high-energy ball milling. J Am Ceram Soc. 2009;92:3114-7.

18) Xu, H., Bhatia, T., Deshpande, S. A., Padture, N. P., Ortiz, A. L. and Cumbrera, F. L. Microstructural evolution in liquid-phase-sintered SiC: Part I, effect of starting powder. J Am Ceram Soc. 2001;84:1578-84.

19) Coelho A. Topas Academic, version 4. Bruker AXS, 2000.

20) Sánchez-Bajo, F., Ortiz, A. L. and Cumbrera, F. L. Analytical formulation of the variance method of line-broadening analysis for Voigtian X-ray diffraction peaks. J Appl Cryst. 2006;39:598-600.

21) Pan, Y. B., Huang, Z. R., Jiang, D. L., Mazerolles, L., Michel, D., Pastol, J-L. and Wang, G. High energy planetary ball milling of SiC powders. Key Eng Mat. 2007;351:7-17.

22) Galán, C. A., Ortiz, A. L., Guiberteau, F. and Shaw, L. L. High-energy ball milling of ZrB_2 in the presence of graphite. J Am Ceram Soc. 2010;93:3072-5.

23) Chamberlain, A. L., Fahrenholtz, W. G. and Hilmas, G. E. Pressureless sintering of zirconium diboride. J Am Ceram Soc. 2006;89:450-6.

24) Suryanarayana, C. Mechanical alloying and milling. Prog Mater Sci. 2001;46:1-184.

25) Li, S., Wang, K., Sun, L. and Wang, Z. A simple model for the refinement of nanocrystalline grain size during ball milling. Scripta Metall Mater. 1992;27:437-42.

26) Soni, P. R. Mechanical alloying. Fundamental and applications. Cambridge International Science Publishing. Cambridge, UK; 2001.

27) Shaw, L., Yang, Z-G. and Ren, R-M. Synthesis of nanostructured Si_3N_4/SiC composite powders through high energy reaction milling. Mater Sci Eng. 1998;A244:113-26.

28) Saberi, Y., Zebarjad, S. M. and Akba, G. H. On the role of nano-size SiC on lattice strain and grain size of Al/SiC nanocomposite. J Alloy Compd. 2009;484:637-40.

29) Kamrani, S., Simchi, A., Riedel, R. and Seyed-Reihani, S.M. Effect of reinforcement volume fraction on mechanical alloying of Al-SiC nanocomposite powders. Powder Metall. 2007;50:276-82.

30) Lu, Z., Zhou, Y., Zhang, M. and Huang, Q. Dry friction behaviour of reaction-bonded silicon carbide at high temperature. Key Eng Mater. 1993;336-338:2472-4.

31) Umeda, K., Enomoto, Y., Mitsui, A. and Mannami, K. Friction and wear of boride ceramics in air and water. Wear. 1993;169:63-68.

32) Lawn, B. R. Fracture of brittle solids. Cambridge University Press, Cambridge, United Kingdom, 1993.

"I do not want to believe, I do want to know"

Carl Edward Sagan (1934-1996)

Chapter III: Oxidation of ZrB_2 Powders during High-Energy Ball-Milling in Air

3.1. MOTIVATION

It has been demonstrated that the refinement of the starting powders and the elimination of surface oxide impurities are two key processing steps to enhance the solid-state sinterability of the poorly sinterable ZrB_2 powders that are being used to process ultra-high-temperature ceramics (UHTCs) [1-7]. The reduction in the particle size shortens the diffusion distance of the chemical species, thus speeding up the densification kinetics significantly for the interparticle-diffusion controlled sintering [8], something that is especially relevant in ZrB_2 due to the serious kinetic restrictions imposed by its strong covalent bonding and its low self-diffusion coefficients [9]. It is not surprising therefore that the typical micrometre-sized ZrB_2 particles need to be refined to the submicrometre range before the sintering heat-treatment. With respect to surface oxide impurities in non-oxide ceramics, they are known to favor the evaporation-condensation mass transport mechanism [10], and this promotes coarsening thus reducing the

driving force for densification and limiting the final density [10]. Hence, it is necessary to remove the surface oxides of ZrO_2 and B_2O_3 in ZrB_2 at temperatures below which coarsening is significant (1650-1850 °C) to thus retain the original particle size up to the temperatures where densification can proceed.

In most studies on ZrB_2 UHTCs, the starting powders are refined by wet attrition milling using some alcohol or inert organic solvent as liquid media [3,4]. Under these wet operating conditions, attrition milling is actually conventional ball-milling because the liquid media reduces the milling intensity, so that its function is only comminution (i.e., particle size reduction). The typical ZrB_2 particles achieved by attrition milling have submicrometre sizes (between 0.6 and 0.2 μm), much smaller than the micrometre-sized particles (~2 μm) of the commonest commercially available ZrB_2 powders. The current practice used to remove the surface oxides of ZrO_2 consists of adding to the ZrB_2 powders sintering additives with a high potential to act as reducing agents, the most widely used of which are C, B_4C, and WC [1,2,5,11]. The removal of B_2O_3 from the surface of ZrB_2 is by evaporation, simply maintaining an actively pumped vacuum at temperatures below 1650 °C [2,6]. Apart from the intrinsic surface oxide layer in the ZrB_2 particles, further oxidation of the ZrB_2 powder occurs during the attrition milling. Typically, between 1 and 2 wt.% oxygen is introduced during attrition milling under flowing argon gas atmosphere, and a little bit more (i.e.,~2 wt.%) if the milling is conducted in air [1-3,6,7,11-14].

Recently, it has been shown that high-energy ball-milling in dry conditions using shaker mills can refine the ZrB_2 powders to the nanoscale [15-17], something that conventional ball-milling cannot do. This is

because the mechanism of crystal size refinement in ZrB_2 is brittle fracture, where the fracture strength scales inversely with the square root of the crystal size [18], and the compressive stresses generated with the impacts during the high-energy ball-milling are sufficiently high (i.e., GPa) to fracture fine particles [19,20]. This refinement to the nanoscale offers unprecedented opportunities to enhance sintering kinetics immensely, as has been demonstrated lately [21]. An aspect that has received no attention to date despite its importance is the oxidation of the ZrB_2 powders during high-energy ball-milling in air. Predicting this oxidation a priori is difficult because high-energy ball-milling times are fairly short (~3 h) relative to attrition milling times (~24 h), which contributes to minimizing the oxidation, whereas the milling intensity is much higher and the nano-particles are more air-sensitive, which factors have the opposite effect.

With these premises in mind, the present study was undertaken with the objective of investigating the oxidation of ZrB_2 powders induced by their high-energy ball-milling in air, because milling in air would simplify the routine of powder preparation. The study includes determination of the oxygen uptake, and the structural and chemical statuses of the captured oxygen.

3.2. EXPERIMENTAL PROCEDURE

3.2.1. Processing

The starting powder was a commercially available micrometer ZrB_2 powder with 99% purity and single crystal particles of average size 2 μm. The

as-purchased ZrB_2 powder was subjected to high-energy ball-milling using a shaker mill (Spex 8000D, Spex CertiPrep, Metuchen, United States) operated at about 1060 back-and-forth cycles per minute. The milling was carried out in a cylindrical hardened-steel container with WC balls (6.7 mm in diameter) at a ball-to-powder weight ratio of 4, for 180 min, in air.

3.2.2. Microstructural Characterization

The ball-milled powder was analyzed using various characterization techniques: transmission electron microscopy (TEM) for the direct examination of the size and morphology of the powder particles and nanocrystals, inert gas fusion (IGF) for the determination of the oxygen uptake, X-ray diffractometry (XRD) for the identification of the amorphous or crystalline nature of the phases present, helium pycnometry for the measurement of the density, and Fourier-transform infrared (FTIR), Raman, and X-ray photoemission (XPS) spectroscopy for the determination of the bonding environment or status. The TEM observations were made at 200 kV in bright-field mode, using two conventional microscopes (Tecnai G^2 20 Twin, FEI, Eindhoven, The Netherlands; and JEM-2100, JEOL, Croissy-sur-Seine, France). The oxygen content measurements were done with an IGF determinator (TC-136, Leco Instrument, St. Joseph, United States) using graphite crucibles, helium gas, and Ni as flux. The XRD data were collected in step-scanning mode (step width 0.02° 2θ, and count time 3 s/step) using a high resolution laboratory diffractometer (D8 Advance, Bruker AXS, Karlsruhe, Germany) equipped with a primary monochromator that provides pure $CuK\alpha_1$ radiation (λ = 1.54183 Å) and a linear ultra-fast detector. Two measurement ranges were employed: 20-80°, and 20-55°. The phases present

were identified with the aid of the PDF2 database, and were quantified using the Rietveld method (Topas 4.1, Bruker AXS, Karlsruhe, Germany). The density measurements were made by helium pycnometry (Stereopycnometer, Quantachrome Instruments, Hartley Wintney, United Kingdom). The FTIR spectra were recorded in the 4000-400 cm^{-1} range on a conventional spectrophotometer (Nicolet iS10, Thermo Scientific, East Grinstead, United Kingdom), using the KBr pellet method and an accumulation condition of 60 scans at 1 cm^{-1} resolution. The Raman spectra were measured in the 1000-125 cm^{-1} range using a micro-Raman spectrometer (Nicolet Almega XR, Thermo Scientific) equipped with a 633 nm He-Ne laser operated at 5.25 mW power, and were the result of 10 accumulations lasting 1 s. The XPS spectra of the Zr 3d and B 1s core lines were recorded in ultra-high vacuum (10^{-6} Pa) in the 176-194 eV range at 0.4 eV energy resolution using a high-resolution spectrometer (K-Alpha, Thermo Scientific) equipped with a monochromatic Al-Kα X-ray source (1486.6 eV). The C 1s peak was used to correct the binding energies in the XPS spectra. The protocol of sample preparation for each of these techniques followed standard procedures for ceramic powders.

3.3. RESULTS AND DISCUSSION

Figure 3.1 compares representative TEM images of the aspurchased ZrB_2 powder and of the ZrB_2 powder ball milled for 180 min in air. Clearly, the high-energy ball-milling has reduced the particle size by one order of magnitude from the micrometre scale (~2-3 μm) to the nanometre scale (~120-200 nm). Furthermore, higher-magnification TEM images such as that shown in Fig. 3.2 indicate that the powder particles after high energy ball-

milling are actually porous agglomerates consisting of many individual tiny single-crystals with an average size of ~10 nm.

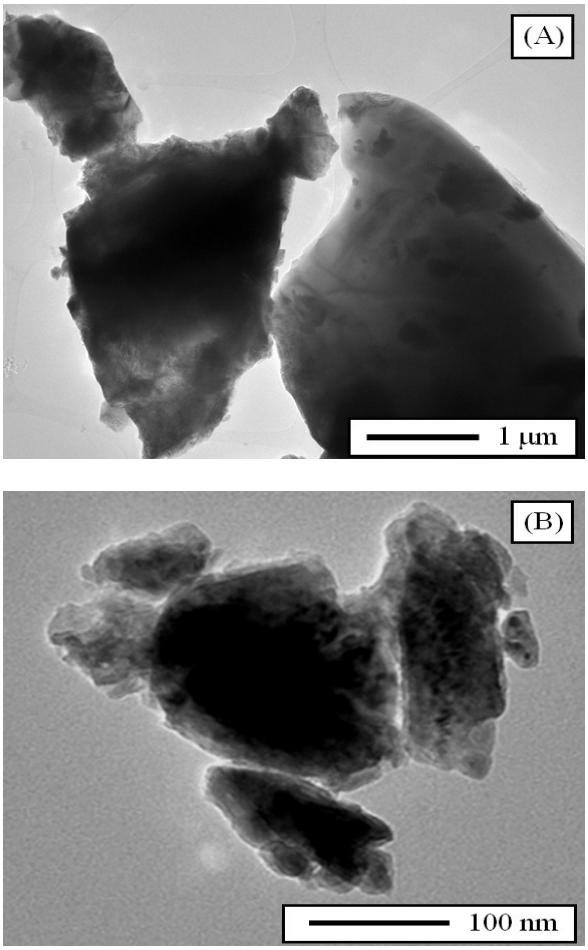

Figure. 3.1. TEM bright-field images of the ZrB_2 powder particles (A) in the as purchased condition, and (B) after high-energy ball-milling for 180 min in air.

The oxygen contents determined by IGF were 1.537 and 4.514 wt.% for the as purchased and ball-milled ZrB_2 powders, respectively, so that one can conclude that there is an oxygen uptake of ~3 wt.% during the high-

energy ball-milling in air. This oxygen content is greater than those typically reported for ZrB_2 powders prepared by attrition milling which are normally in the 2-3 wt.% range depending on the exact milling conditions [1-3,6,7,11-14]. To explore the structural and chemical statuses of the oxygen captured during the high-energy ball-milling in air, an exhaustive characterization of the ball-milled powder was needed, as we shall describe next.

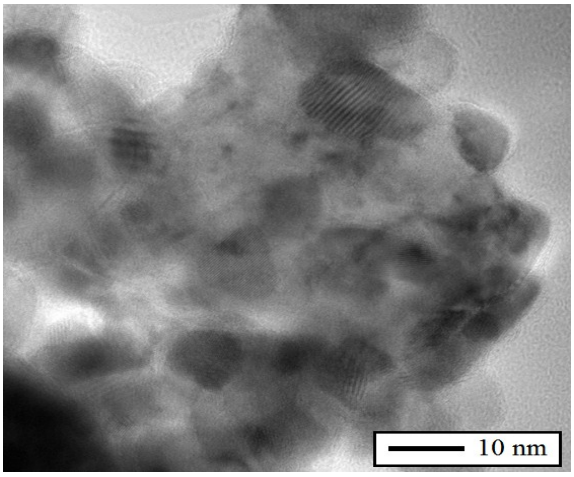

Figure. 3.2. TEM bright-field image of the interior of the ZrB_2 powder particles with 180 min of high-energy ball-milling in air, showing the agglomeration and cold-welding of individual primary nano-particles with 10 nm size.

Figure 3.3 compares the XRD patterns of the ZrB_2 powder before and after the high-energy ball-milling for 180 min in air. Apart from the reduction in the peak intensity, the marked peak broadening, and the increase in the background after the high-energy ball-milling that together reflect the crystallite size refinement to the nanoscale (~10 nm), and the presence of additional peaks that reveal the introduction of 2.5 wt.% of WC according to the corresponding Rietveld analysis, there are another two important features

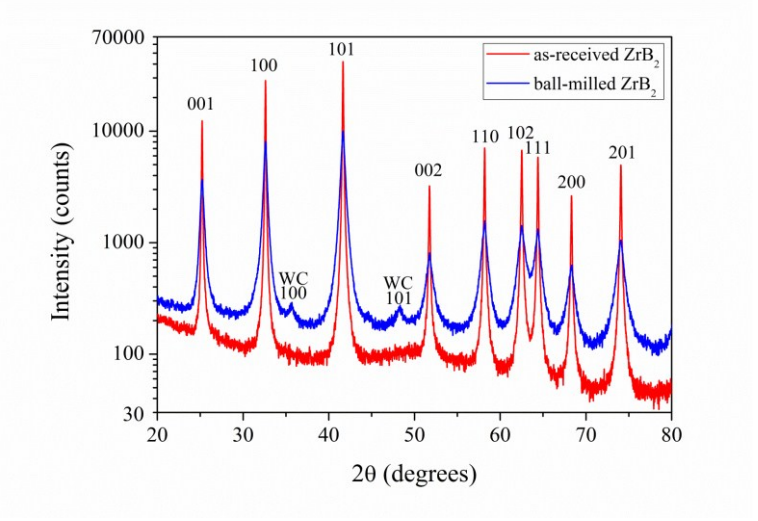

Figure. 3.3. XRD patterns of the ZrB_2 powders before and after high-energy ball-milling for 180 min in air. The WC peaks free of overlap with ZrB_2 peaks (which have been indexed) are marked. The logarithmic scale is to facilitate appreciation of the WC peaks (also indexed).

in the figure. The first is that the ZrB_2 peaks remain in place. Since the absence of peak shifting excludes the formation of solid-solutions with oxygen atoms as solutes in the ZrB_2 host, it can be concluded that the oxygen captured during the high-energy ball-milling in air has formed oxides. The second is the absence of ZrO_2 and/or B_2O_3 peaks in the XRD patterns of the ball-milled ZrB_2 powder. Taking this observation together with the previous one, one can conclude that these oxides are amorphous. One could nevertheless argue that it would be very difficult to detect B_2O_3 by XRD in the presence of ZrB_2 because the scattering factor of Zr will dominate the entire diffractogram. Nevertheless, ZrO_2 should be detected which would prove the oxidation via the reaction:

$$ZrB_2 + 5/2O_2 \longrightarrow ZrO_2 + B_2O_3$$

if this oxidation reaction had resulted in crystalline oxides. It could also be argued that crystalline ZrO_2 and B_2O_3 are formed during the high-energy ball-milling in air, but at amounts below the XRD detection limit. However, given the oxygen content determined by IGF and assuming equimolar formation of ZrO_2 and B_2O_3 as predicted by the above reaction, their concentrations is estimated to be 6.95 and 3.93 wt.%, respectively, which are clearly high enough to be detected by XRD.

To prove that this is indeed the case, two powder mixtures in which 1 wt.% crystalline ZrO_2 was added to ZrB_2 were prepared and analyzed by XRD. In one of these two mixtures the crystals had submicrometre sizes and in the other nanometre sizes, done so as to rule out any crystallite-size effect in the detection of crystalline ZrO_2 in ZrB_2-based powders. It can be seen in Fig. 3.4 that, despite the low ZrO_2 concentration of only 1 wt.%, the XRD

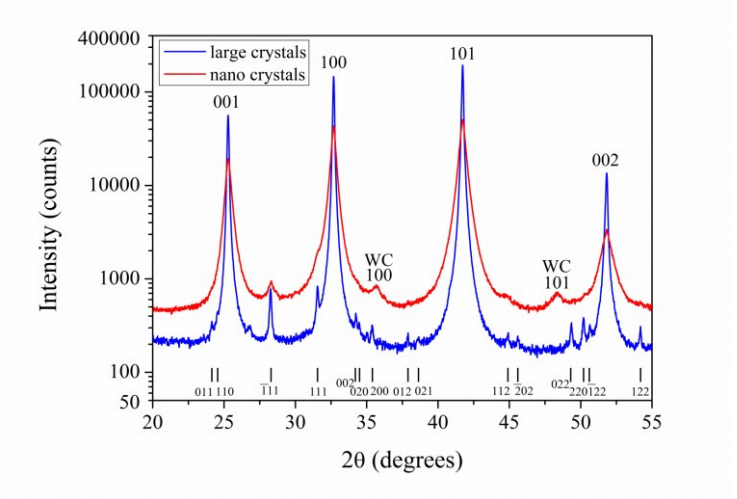

Figure. 3.4. XRD patterns of the ZrB_2+1wt.% ZrO_2 powder mixtures with coarse crystals and with nano-crystals. The WC peaks free of overlap with ZrB_2 peaks (which have been indexed) are marked. The position of the ZrO_2 peaks is marked with short vertical lines. The logarithmic scale is to facilitate appreciation of the ZrO_2 and WC peaks (also indexed).

patterns of these mixtures exhibit clear peaks of this oxide. Hence, these observations confirm that the oxide concentration deduced from IGF is above the detection limit of the diffractometer, and therefore that the oxides formed during high-energy ball-milling in air are amorphous because otherwise they would have been detected.

Despite its non-crystalline nature, the amorphous-phase content in the ball-milled ZrB_2 powder can be estimated from its XRD pattern using the Rietveld method in conjunction with the spiking technique (known crystallinity internal-standard method). In the present study, 30 wt.% Al_2O_3 was used as the spike phase because it provides a sufficient number of peaks in the XRD pattern with no overlap with the ZrB_2 peaks, and because its oxide nature rules out the presence of a passivating amorphous layer. With this XRD analysis, as shown in Fig. 3.5, the amorphous-phase content in the

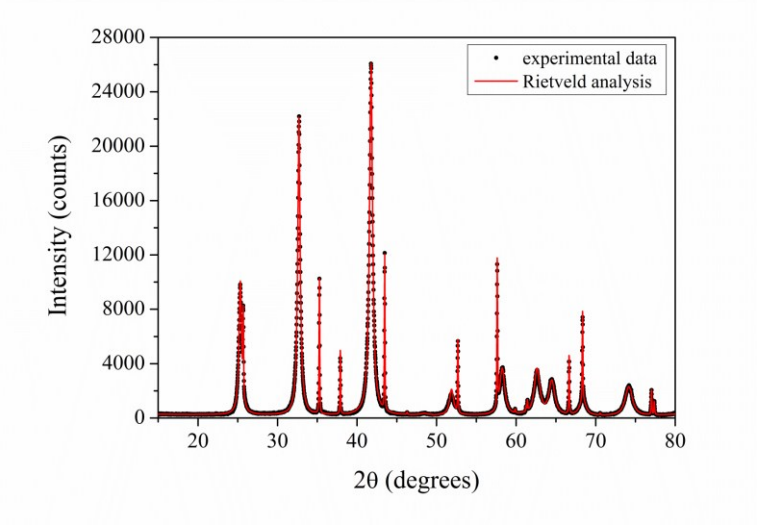

Figure. 3.5. Rietveld analysis of the XRD pattern of the ZrB_2 powder with 180 min of high-energy ball-milling in air plus 30 wt.% of α-Al_2O_3 submicrometre powder. The points are the experimental data and the solid line is the Rietveld refinement.

ball-milled ZrB_2 powder was calculated to be 12 wt.%, which is clearly consistent with the oxide concentration (i.e., ZrO_2 + B_2O_3) determined by IGF (~11 wt.%).

The measurements of the powder density performed by helium pycnometry also lend strong credence to the formation of amorphous oxides, as they show that the density decreases from 6.12 $g \cdot cm^{-3}$ in the as-purchased condition to 5.82 $g \cdot cm^{-3}$ after 180 min of high-energy ball-milling in air. Using the rule-of-mixture with the values of theoretical density and volume concentrations determined experimentally of ZrB_2 (6.1 $g \cdot cm^{-3}$, 86.94 wt.%), WC (17.67 $g \cdot cm^{-3}$, 2.23 wt.%), ZrO_2 (5.86 $g \cdot cm^{-3}$, 6.91 wt.%) and B_2O_3 (2.46 $g \cdot cm^{-3}$, 3.93 wt.%), the density of the ball-milled powder was calculated to be 5.826 $g \cdot cm^{-3}$, in perfect agreement with the experimental measurement.

To further investigate the formation of amorphous ZrO_2 and B_2O_3 during the high-energy ball-milling of ZrB_2 in air, FTIR and Raman spectroscopy studies were conducted with the aim of detecting the vibration bands of the Zr-O and B-O bonds. Shown in Figs. 3.6 and 3.7 are, respectively, the FTIR and Raman spectra of the as-purchased and ball-milled ZrB_2 powders, together with the spectra of ZrO_2 and B_2O_3 powders that were also collected experimentally and included for comparison. As can be seen in Fig. 3.6, not only are the FTIR spectra from the two ZrB_2 powders similar, but neither do they exhibit the vibration bands typical of ZrO_2 and B_2O_3. As shown in Fig. 3.7, this scenario is also valid for the Raman spectra, despite ZrB_2 not being Raman active [22] which in principle should have facilitated the detection of the Raman peaks of ZrO_2 and B_2O_3. Thus, it can be concluded that the FTIR and Raman spectroscopic studies are unable to conclusively discriminate the presence of the concentrations of ZrO_2 and B_2O_3 formed

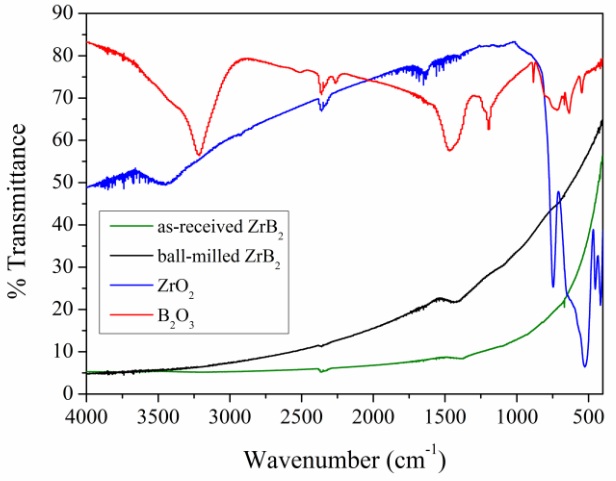

Figure. 3.6. FTIR spectra of the ZrB_2 powders before and after high-energy ball-milling for 180 min in air. The FTIR spectra of ZrO_2 and B_2O_3 have been included for comparison. The bands at ~2350, 1400 and 670 cm^{-1} and the noise at 3900-3650 and 1830-1430 cm^{-1} are due to background.

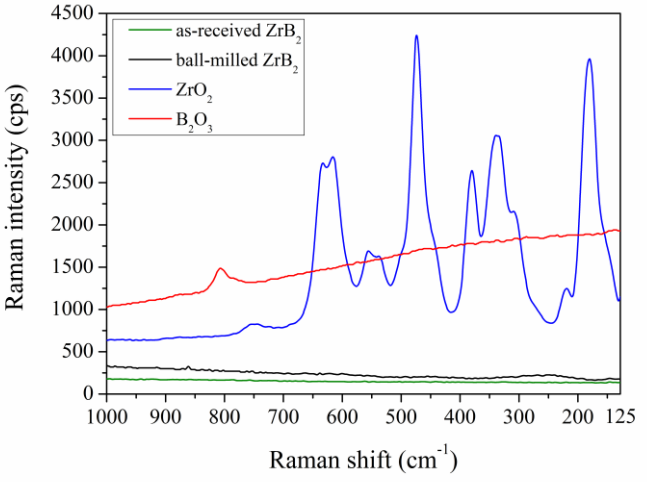

Figure. 3.7. Raman spectra of the ZrB_2 powders before and after high-energy ball-milling for 180 min in air. The Raman spectra of ZrO_2 and B_2O_3 have been included for comparison.

during the high-energy ball-milling of ZrB_2 in air.

To confirm the formation of amorphous oxides as deduced from the XRD, IGF and helium pycnometry analyzes, the as-purchased and ball-milled ZrB_2 powders were investigated by XPS, which is a spectroscopic technique with a far better detection limit than FTIR or Raman spectroscopy. In particular, we monitored the binding energy of the Zr 3d and B 1s core levels before and after the high-energy ball-milling for 180 min in air (Fig. 3.8). One

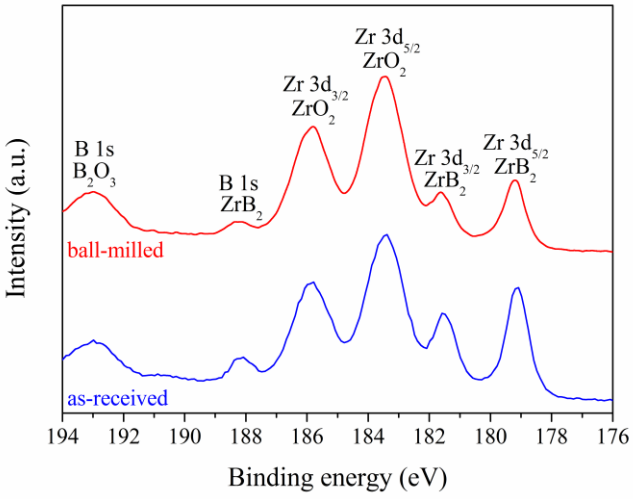

Figure. 3.8. High-resolution XPS spectra of the Zr 3d and B 1s core-levels for the ZrB_2 powders before and after high-energy ball-milling for 180 min in air.

observes that the Zr 3d core level shows the typical $3d_{5/2}$ and $3d_{3/2}$ spin-orbit split, while the B 1s core level exhibits the typical single peak. However, two Zr $3d_{5/2}$-$3d_{3/2}$ doublets and two B 1s singlets are observed in each powder, which is a clear sign of the existence of two different bonding statuses for the Zr and B atoms. In both the as-purchased and the ball-milled powders, one set of Zr $3d_{5/2}$-$3d_{3/2}$ doublets plus B 1s singlet is located at binding energies

of ~179.2, 181.6, and 188.2 eV, respectively, values which are attributed to ZrB_2 [23,24]. The other set of doublets plus singlet appears at higher binding energies of ~183.5, 185.9, and 193.1 eV, respectively, which are due to ZrO_2 and B_2O_3 [23,24]. One also observes that the ZrO_2/ZrB_2 and B_2O_3/ZrB_2 peak intensity ratios are greater in the powder subjected to high-energy ball-milling in air. Therefore, XPS has unambiguously detected the presence of ZrO_2 and B_2O_3 in the as-purchased and ball-milled ZrB_2 powders, and also shows them to be much more abundant in the ball-milled powder. Also noted in the XPS spectra of the two powders are that the ZrO_2 related peaks are more intense than the ZrB_2 related peaks. This observation, together with the oxygen contents that showed that the oxides are minor components and the fact that XPS is a surface technique, indicate that ZrO_2 and B_2O_3 cover the surface of the ZrB_2 particles. This hypothesis was further tested experimentally in the ball-milled powder by etching the surface with Ar^+ ions to remove material followed by XPS data collection, and also by TEM. One observes in Fig. 3.9 that the ZrB_2/ZrO_2 and ZrB_2/B_2O_3 peak intensity ratios increase after the etching, a clear sign that the ZrB_2 powder particles are covered by an oxide layer. As can be seen in Fig. 3.10, the direct high-resolution TEM observations also support the presence of an amorphous nano-film at the fringe of the agglomerates. This oxide distribution is attributed to two factors: (i) the lower chemical affinity between the oxides and ZrB_2 than between ZrB_2 crystals themselves which would promote cold-welding during the high-energy ball-milling via contacts of the type ZrB_2-ZrB_2; and (ii) the spontaneous surface passivation of ball milled powder particles when exposed to ambient conditions after the high-energy ball-milling.

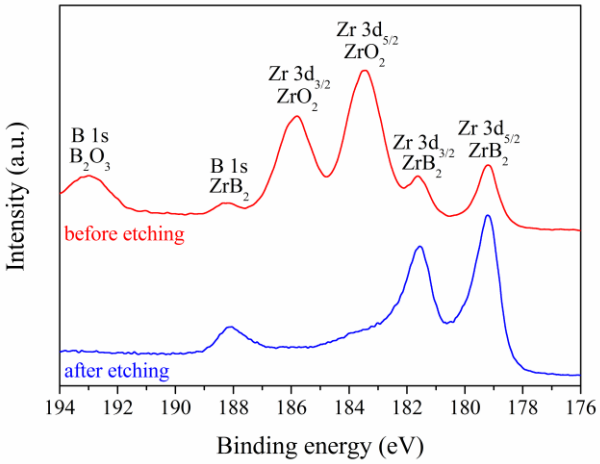

Figure. 3.9. High-resolution XPS spectra of the Zr 3d and B 1s core-levels for the ZrB_2 powders with 180 min of high-energy ball-milling in air before and after etching with Ar+ ions. Also included in the figure is the peak indexing. The spectra have been shifted along the Y-axis to facilitate comparison.

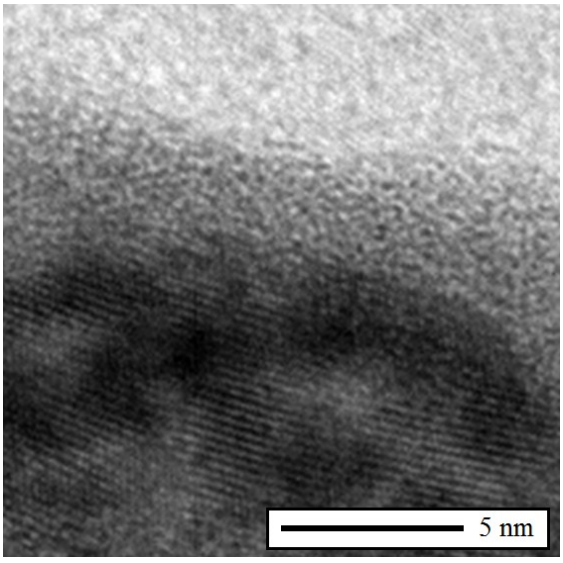

Figure 3.10. High-resolution TEM bright-field image of the fringe of the ZrB_2 powder particles with 180 min of high-energy ball-milling in air, showing the presence of an amorphous region of nanometric thickness.

Finally, it is worth mentioning that a recent spark-plasma sintering (SPS) study [21] has revealed that the greater oxygen content of this ZrB_2 nano-powder obtained by high-energy ball-milling in air does not hinder its densification. On the contrary, it exhibits improved SPS kinetics relative to powders with larger particles and less oxygen content, which has been attributed to the large inter-particle boundary surface area[a] that can greatly enhance grain-boundary diffusion at lower temperatures. Whether the SPS results can or not be extrapolated to the pressureless sintering (PS) is something that has yet to be investigated experimentally. Whichever the case, it is reasonable to think that the sinterability of this ZrB_2 nano-powder (by SPS, PS, or hot-pressing) would improve further if the high-energy ball-milling were performed in an inert atmosphere, although the comminution routine would be more tedious and costly.

3.4. SUMMARY

Oxide impurities in ZrB_2 powders promote coarsening, resulting in lower sinterability. Given its importance for sintering, we studied the oxidation of ZrB_2 powders during high-energy ball-milling (the form of milling able to refine ZrB_2 powders to the nanoscale) with the aid of various characterization techniques, namely fusion in inert gas, X-ray diffractometry, helium pycnometry, transmission electron microscopy, and Fourier-transform infrared, Raman, and X-ray photoemission spectroscopy. It was found that

[a] Taking an average agglomerate size of 200 nm and a primary particle size of 10 nm with the assumption of spherical agglomerates, the inter-particle boundary area per unit volume within each agglomerate is 1.67×10^7 m^{-1}.

powders as the more conventional attrition milling. Also this oxygen does not form solid solutions with ZrB_2, but amorphous oxides (i.e., ZrO_2 and B_2O_3) that locate preferentially on the surface of the ultra-fine agglomerates resulting from col-welding of the nano-particles that forma during the ball-milling.

3.5. REFERENCES

1) Chamberlain, A. L., Fahrenholtz, W. G. and Hilmas, G. E. Pressureless sintering of zirconium diboride. J Am Ceram Soc. 2006;89:450-6.

2) Zhang, S. C., Hilmas, G. E. and Fahrenholtz, W. G. Pressureless densification of zirconium diboride with boron carbide additions. J Am Ceram Soc. 2006;89:1544-50.

3) Fahrenholtz, W. G., Hilmas, G. E, Talmy, I. G. and Zaykoski, J. A. Refractory diborides of zirconium and hafnium. J Am Ceram Soc. 2007;90:1347-64.

4) Guo, S-Q. Densification of ZrB_2-based composites and their mechanical and physical properties: a review. J Eur Ceram Soc. 2009;29:995-1011.

5) Zhu, S., Fahrenholtz, W. G., Hilmas, G. E. and Zhang, S. Pressureless sintering of zirconium diboride using boron carbide and carbon additions. J Am Ceram Soc. 2007;90:3660-3.

6) Fahrenholtz, W. G., Hilmas, G. E., Zhang, S. C. and Zhu, S. Pressureless sintering of zirconium diboride: particle size and additive effects. J Am Ceram Soc. 2008;91:1398-404.

7) Thompson, M., Fahrenholtz, W. G. and Hilmas, G. Effect of starting particle size and oxygen content on densification of ZrB_2. J Am Ceram Soc. 2011;94:429-35.

8) Herring, C. Effect of change of scale on sintering phenomena. J Appl Phys. 1950;21:301-3.

9) Telle, R., Sigl, L. S. and Takagi, K. Boride-based hard materials. Handbook of Ceramic Hard Materials, vol. 2, Wiley-VCH, Weinheim, 2000, 802-945.

10) Dole, S. L., Prochazka, S. and Doremus, R. H. Microstructural coarsening during sintering of boron carbide. J Am Ceram Soc. 1989;72:958-66.

11) Zhu, S., Fahrenholtz, W. G., Hilmas, G. E. and Zhang, S. C. Pressureless sintering of carbon-coated zirconium diboride powders. Mater Sci Eng A. 2007;459:167-71.

12) Zhang, H., Yan, Y., Huang, Z., Liu, X. and Jiang, D. Pressureless sintering of ZrB_2-SiC ceramics: the effect of B_4C content. Scripta Mater. 2009;60:559-62.

13) Zhang, S. C., Hilmas, G. E. and Fahrenholtz, W. G. Mechanical properties of sintered ZrB_2-SiC ceramics. J Eur Ceram Soc. 2011;31:893-901.

14) Wang, X-G., Guo, W-M. and. Zhang, G-.J Pressureless sintering mechanism and microstructure of ZrB_2-SiC ceramics doped with boron. Scripta Mater. 2009;61:177-80.

15) Galán, C. A., Ortiz, A. L., Guiberteau, F. and Shaw, L. L. Crystallite size refinement of ZrB_2 by high-energy ball milling. J Am Ceram Soc. 2009;92: 3114-7.

16) Galán, C. A., Ortiz, A. L., Guiberteau, F. and Shaw, L. L. High-energy ball milling of ZrB_2 in the presence of graphite. J Am Ceram Soc. 2010;93:3072-5.

17) Zamora, V., Ortiz, A. L., Guiberteau, F., Nygren, M. and Shaw, L. L. On the crystallite size refinement of ZrB_2 by high-energy ball milling in the presence of SiC. J Eur Ceram Soc. 2011;31:2407-14.

18) Lawn, B. R. Fracture of brittle solids. Cambridge University Press, Cambridge, United Kingdom, 1993.

19) Suryanarayana, C. Mechanical alloying and milling. Prog Mater Sci. 2001;46:1-184.

20) Soni, P. R. Mechanical Alloying. Fundamental and Applications. Cambridge International Science Publishing, Cambridge, UK, 2001.

21) Zamora, V., Ortiz, A. L., Guiberteau, F. and Nygren, M. Crystal-size dependence of the spark-plasma-sintering kinetics of ZrB_2 ultra high-temperature ceramics. J Eur Ceram Soc. 2012;32:271-6.

22) Watts, J., Hilmas, G., Fahrenholtz, W. G., Brown, D. and Clausen, B. Measurement of thermal residual stresses in ZrB_2-SiC composites. J Eur Ceram Soc. 2011;31:1811-20.

23) Huerta, L., Durán, A., Falconi, R., Flores, M. and Escamilla, R. Comparative study of the core level photoemission of the ZrB_2 and ZrB_{12}. Physica C. 2010;470:456-60.

24) Alfano, D., Scatteia, L., Monteverde, F., Bêche, E. and Balat-Pichelin, M. Microstructural characterization of ZrB_2-SiC based UHTC tested in the MESOX plasma facility. J Eur Ceram Soc. 2010;30:2345-55.

"Scientific research is one of the most exciting and rewarding of occupations"

Frederick Sanger (1918)

Chapter IV: Crystal-Size Dependence of the Spark-Plasma-Sintering Kinetics of ZrB_2 Ultra-High-Temperature Ceramics

4.1. MOTIVATION

Ultra-high-temperatureh ceramics (UHTCs) are a key element for progress in various extreme-environment aerospace applications such as hypersonic flight, scram-jet propulsion, rocket propulsion, and atmospheric re-entry [1]. Zirconium diboride (ZrB_2) is one of the short list of candidate UHTCs, and probably the one that has received most attention to date [2,3]. Unfortunately, one of the major obstacles for the development and implementation of ZrB_2 UHTCs is that the serious kinetic constraints imposed by the combination of the strong covalent bonding, low self-diffusion coefficients, oxygen impurities on the particle surfaces, and large particle sizes makes it impossible to densify the typical commercially available micrometre ZrB_2 powders by conventional sintering (pressureless sintering or hot pressing) at moderate temperatures [2,3]. It is not surprising therefore that the search for

a solution to the problem of the poor sinterability of ZrB_2, as also of other UHTCs, is an area of particular interest for research [2,3].

It is well known that the sinterability of highly covalent-bonded ceramics can be enhanced by refining the starting powders due to the reduction in the diffusion distance of chemical species [4]. This is also true for ZrB_2 UHTCs, as has recently been demonstrated by Thompson et al [5]. They pressureless sintered pure ZrB_2 powders with two crystal sizes under the same conditions, and found that the density increased by ~10% in the temperature range of 1600-2100 °C when the crystal size was reduced by attrition milling from the as-purchased condition of ~2 μm down to ~0.2 μm, although the densification was anyway still very limited (i.e., as low as 75% at 2100 °C for the ball-milled powder) [5]. They also observed with the same powders that the relative density reached by spark-plasma sintering (SPS) at 1900 °C for 5 min increased from ~70 to 97% with crystal size refinement from the micrometer down to the submicrometre range [5]. These and other observations [2,3,5,6] have reinforced the commonly held belief that ZrB_2 is intrinsically unsinterable without pressure in the pure state, but that it can be densified by SPS or hot pressing at nearly 1900 °C if the starting powders are refined appropriately, because the sintering kinetics of pure ZrB_2 depends on the crystal size. However, investigation into the crystal-size dependence of the sintering kinetics of pure ZrB_2 UHTCs has been limited to studying the densification data corresponding to micrometre or submicrometre crystal sizes. No information exists for crystals at the nanoscale, even though this is the scale at which one expects improvement in the kinetic performance of the powder to be most relevant. This underscores the need to include more crystal sizes in a

systematic densification study of pure ZrB_2 UHTCs in order to determine the broader trend of the crystal size dependence of ZrB_2 density.

The present study was therefore aimed at comparing the SPS kinetics of micrometre, submicrometre, and nanocrystalline ZrB_2 powders without additives. Although SPS is similar to HP in that they both apply a uniaxial load, it has the advantage that the pulsed electrical current heats the die (and the compact if the powder is electrically conductive) directly, and the rapid sintering cycles enable better control of the final microstructure and therefore of the properties of the resulting material [7-10]. Since the fine and ultra-fine ZrB_2 powders are typically prepared by milling the commercially-available coarse powders, the broader objective of the present study is to advance towards the lower-temperature sintering of ZrB_2 UHTCs via the optimization of the comminution practice.

4.2. EXPERIMENTAL PROCEDURE

4.2.1. Processing

A commercially available micrometre powder of ZrB_2 (Grade B, H.C. Starck, Berlin, Germany) was chosen as starting material to prepare the rest of the powders. To this end, the as-purchased powder of single-crystal particles of 2 μm average size was subjected to high-energy ball-milling in a shaker miller (Spex 8000D, Spex CertiPrep, Metuchen, United States) operated at about 1060 back-and-forth cycles per minute. The milling was carried out in cylindrical hardened-steel containers with WC balls (6.7 mm in diameter)

under a ball-to-powder weight ratio of 4, and for times in the range of 1-180 min to impart different degrees of milling intensity to the as purchased ZrB_2 powder, and thus create an ample set of ZrB_2 powders with crystal sizes ranging progressively from ~2 μm all the way down to just some nanometres (in particular, 10 nm). The X-ray diffractometry (XRD; D8 Advance, Bruker AXS,Karlsruhe, Germany) analysis[a] [13] of the ball-milled powders shown in Fig. 4.1 revealed that there indeed occurred such a progressive decrease in

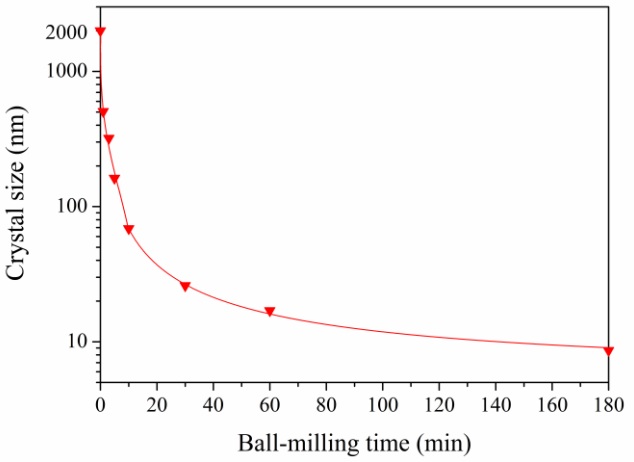

Figure. 4.1. Average size of the ZrB_2 crystals as a function of high-energy ball-milling time, determined by XRD. The points are the experimental data, and the solid line is merely to guide the eye. The crystal size in the as-purchased condition was taken to be the same as the particle size measured by electron microscopy.

[a] To allow the valid measurement of the crystal size in all ball-milled powders, the XRD data of the most intense peak of ZrB_2 (i.e., its 101 peak) were collected using a high-resolution diffractometer equipped with a primary monochromator that provides pure $CuK\alpha_1$ radiation as well as with an ultra-fast linear detector, and configured with thin slits to ensure a very sharp instrumental broadening, and the calculations were made by applying the variance method with Voigt profile functions [13]. Furthermore, the crystal sizes so calculated have been validated by transmission electron microscopy in the chapter 3.

crystal size with increasing high-energy ball-milling time, but the laser scattering analysis (LS; Mastersizer 2000, Malvern Instruments, Worcestershire, United Kingdom) of the powders shown in Fig. 4.2 indicated however that the nano-crystals achieved with the long-time high-energy ball-milling had actually agglomerated [11,12]. The LS analysis also indicated that the particle size distributions were all unimodal, and with similar relative size dispersion (i.e., ~1.5-1.7 as measured in terms of $(D_{90}-D_{10})/D_{50}$).

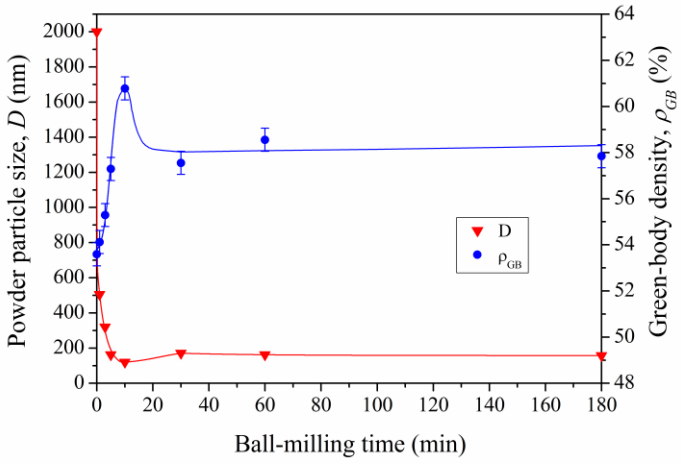

Figure. 4.2. Average particle size in the ZrB_2 powders as a function of high-energy ball-milling time, determined by LS. Also included is the green-body densification for the ZrB_2 without and with the high-energy ball-milling. The points are the experimental data, and the solid lines are merely to guide the eye.

4.2.2. Sintering

The different ZrB_2 powders were individually loaded into 12-mm diameter graphite dies lined with graphite foil, and were spark-plasma sintered (Dr. Sinter SPS-2050, Sumitomo Coal Mining Co, Tokyo, Japan) in dynamic

vacuum (i.e., ~6 Pa) up to 1900 °C. The temperature was first raised to 600 °C in 3 min, and thence onwards was measured by an optical pyrometer focused on the die. The heating ramp was set at 200 °C/min up to 1200 °C, and at only 100 °C/min from 1200 to 1900 °C because, this being the critical densification range [14], it was advisable to monitor the progress in more detail. A uniaxial pressure of 50 MPa was applied up to 1200 °C, and was then increased to 75 MPa and maintained until completion of the sintering cycle. The soaking at 1900 °C lasted as long as was required for the punches to cease traveling, at which moment the load was released and the electrical power was shut off to allow rapid cooling to room temperature (i.e., in 1-2 min). The SPS furnace is equipped with a dilatometer of resolution better than 0.001 mm, connected to a computer to log the shrinkage curves. These curves were corrected for the expansion of the graphite parts (i.e., die, punches, and spacers) to give the real shrinkage curve of the powder itself. The densification curves were reconstructed from the shrinkage curves by considering the relative densities of the sintered samples.

4.2.3. Microstructural Characterization

These relative densities were determined by first measuring the absolute density by the Archimedes method using distilled water as the immersion medium, and then dividing by the density of the powder measured by helium pycnometry (Multipycnometer, Quantachrome Instruments, Florida, United States). The microstructure of the sintered materials was observed by scanning electron microscopy (S-3600N, Hitachi, Ibarakiken, Japan) to validate the porosity data.

4.3. RESULTS AND DISCUSSION

Figure 4.3 shows the densification curves as a function of time for the ZrB_2 powder before and after the different degrees of milling intensity. It can be seen that the curves all have the same general shape, i.e., there is first a plateau, then the sintering progresses moderately, then much more abruptly, and lastly gradually towards the ultimate densification. It can also be seen in Fig. 4.3 that with increasing ball-milling time the densification curves shift towards lower times, i.e., towards lower temperatures, and that the ultimate densification increases. Both these aspects constitute clear evidence that the high-energy ball-milling enhances the sintering kinetics of ZrB_2. Note that the

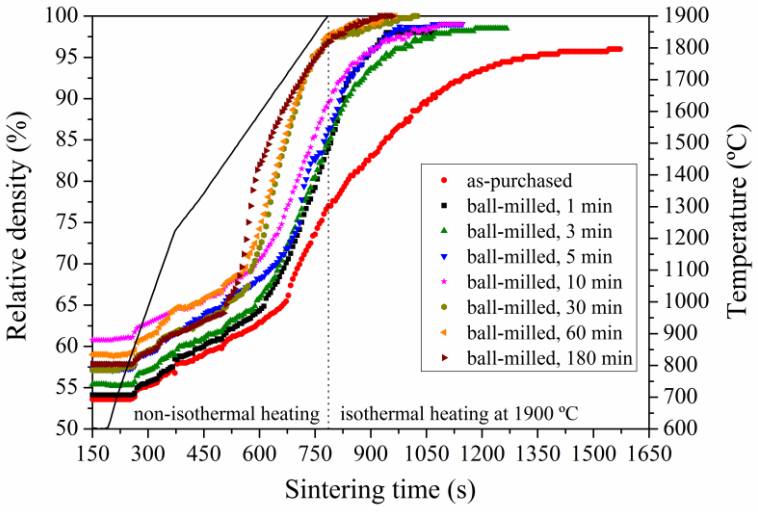

Figure. 4.3. SPS-densification curves as a function of time for the as-purchased ZrB_2 powder and the ZrB_2 powders subjected to high-energy ball-milling. The points are the experimental data. The solid line indicates the temperature profile used. The dashed line separates the regimes of non-isothermal and isothermal heating during the SPS cycle.

improvement in kinetic performance of the powder cannot be attributed to possible contamination by WC that would help in the densification because (i) this was only detected in a minimal amount (i.e., less than 2.5 wt.% of WC as measured by XRD through the Rietveld method and confirmed by energy-dispersion X-ray spectroscopy) in the powder with 180 min of ball-milling [15] while the enhancement in sintering behavior is observed for all ball-milled powders, and (ii) the thermodynamic calculation shows that in the standard state the removal reaction of ZrO_2 by WC is favourable above 1944 °C [16], and indeed WC has been observed to act as a pressureless sintering additive above 2100 °C [17]. Three different forms of sintering behaviour can be distinguished in Fig. 4.3. Firstly, there is the as-purchased powder with a micrometre crystal size of ~2 μm, which has the slowest sintering kinetics; secondly there are the powders ball-milled for 1, 3, and 5 min which have somewhat faster sintering kinetics than that of the as-purchased powder; and thirdly, there are the powders ball-milled for 30, 60, and 180 min which have much faster sintering kinetics than the rest of the powders. The kinetics of the powder ball-milled for 10 min is intermediate between that of the powders with short (1, 3, and 5 min) and long (30, 60, and 180 min) ball-milling times.

According to Fig. 4.1, it can be concluded that the kinetics improvement is only moderate when the crystal size is refined to within the submicrometre range (i.e., ball-milling times of 1, 3, and 5 min), but notable when the crystal size is refined to within the nanoscale (i.e., ball-milling times of 30, 60, and 180 min). These results have important practical implications because they reveal that high-energy ball milling can provide ZrB_2 powders with the superior kinetic performance not achievable today via attrition milling. Note that attrition milling has been so far the gold standard

comminution treatment of ZrB_2 powders, but it refines the crystal sizes only down to ~0.5-0.2 μm, a size scale at which improvement in sintering behaviour was found to be only moderate (see Fig. 4.3).

Let us now examine the densification curves in greater detail. Firstly, it can be seen in Fig. 4.3 that the initial densification (henceforth termed green-body densification because the density measurements performed on selected powders showed no differences in the degree of densification at 25 °C and at the onset of the SPS cycle at 600 °C) has a complex dependence on ball-milling time, and does not correlate with the crystal size as it first increases, then decreases, and finally again increases slightly or stabilizes within the errors despite the crystal size decreasing progressively with ball-milling time (see Fig. 4.1). This observation was not a surprise because the powder packing density scales inversely with powder particle sizes [18], not with crystal sizes. As shown in Fig. 4.2, the evolution of the green-body densification with ball-milling time follows qualitatively the inverse trend of the average powder particle size. This simplistic correlation between the green-body densification and the average powder particle size is probably because the particle size distributions are all unimodal and self-similar. Secondly, it can also be seen in Fig. 4.3 that the densification curves all exhibit a densification jump at ~260-265 s (i.e., at 850-880 °C), followed by a gradual linear increase in densification. This jump and the subsequent linear stretch of densification can be attributed to mechanical compaction of the powder [19]. A second densification jump is also observed at ~370-380 s (i.e., at ~1200 °C), which is when the load was increased from 50 to 75MPa. Thirdly, the temperature for the onset of sintering (T_{OS}), which is the temperature at which the curves start to deviate from the linear compaction stretch, decreases continuously with

decreasing crystal size. In particular, as shown in Fig. 4.4 the decrease in T_{OS} is only moderate with the reduction of crystal size within the submicrometre range (~100 nm), but abrupt from there on downwards.

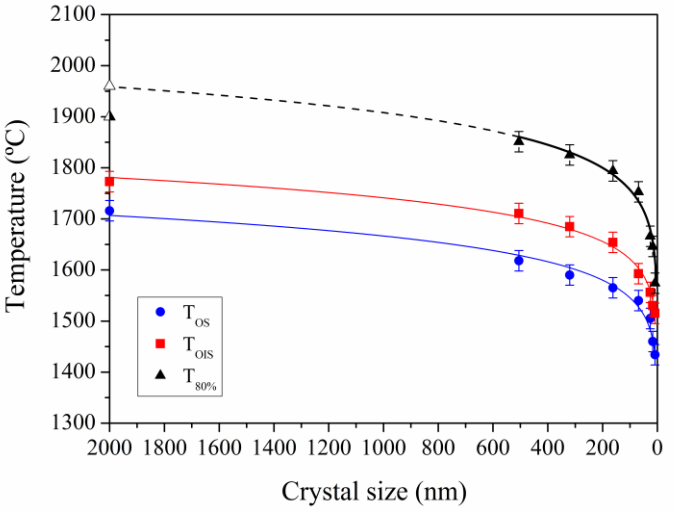

Figure. 4.4. Evolution of T_{OS}, T_{OIS}, and $T_{80\%}$ with the reduction in crystal size. The points are the experimental data, and the solid lines through the T_{OS} and T_{OIS} data are merely to guide the eye. The thicker solid line through the $T_{80\%}$ data is the fit used to compute the activation energy of the grain-boundary diffusion in ZrB_2. The dashed line is the prediction of the fit for the crystal size of the as purchased powder. The open and semi-closed triangles are the values of $T_{80\%}$ determined for the as-purchased powder in the isothermal heating regime and the extrapolation of the non-isothermal densification curve to 80% of relative density, respectively.

This same trend is also apparent for the temperature of the onset of the intermediate stage of sintering (T_{OIS}), which is the sintering regime in which the open porosity is eliminated and typically begins at a relative density of ~70% [20]. The temperature for the onset of the final stage of sintering (T_{OFS}), which is the sintering regime in which the closed porosity is eliminated

and typically begins at a relative density of ~90% [20], also drops with reduction in crystal size. Thus, whereas in the as-purchased powder and in the powders ball-milled for 1, 3, and 5 min the final stage of sintering initiates after the isothermal heating at 1900 °C for 272, 42, 35, and 25 s, respectively, it occurs in the non isothermal regime at 1900 °C in the powder ball-milled for 10 min and at 1770±10 °C in the powders with 30, 60, and 180 min of ball-milling. And fourthly, the degree of non-isothermal densification and the ultimate densification also improve with the reduction in crystal size. Thus, whereas in the as-purchased powder and in the powders ball-milled for 1, 3, and 5 min the final stage of sintering initiates after the isothermal heating at 1900 °C for 272, 42, 35, and 25 s, respectively, it occurs in the non isothermal regime at 1900 °C in the powder ball-milled for 10 min and at 1770±10 °C in the powders with 30, 60, and 180 min of ball-milling. And fourthly, the degree of non-isothermal densification and the ultimate densification also improve with the reduction in crystal size. Note that the as-purchased powder with micrometer-sized crystals reached only ~78% density at 1900 °C, which increased up to ~96% after the isothermal heating at 1900 °C for 13 min. The powders with submicrometre-sized crystals (i.e., those ball-milled for 1, 3, and 5 min) reached a greater density of ~86-88% at 1900 °C, and almost full density (>98%) when soaked there for ~6 min. The ultra-fine powder ball-milled for 10 min densified up to ~91% at 1900 °C, and up to ~99% when maintained at 1900 °C for 6 min. Finally, the nano-powders (i.e., those ball-milled for 30, 60, and 180 min) reached ~98% density at 1900 °C, and densified completely after a brief soaking time at 1900 °C that was indeed shorter with decreasing crystal size (i.e., 228, 150, and 144 s, for the 26, 17, and 9 nm sizes, respectively). The direct observation of the microstructures by

SEM confirmed these densification data. As shown in Fig. 4.5.A and B, pores can be clearly seen in the UHTC fabricated from the as-purchased powders, whereas they were hardly discernible in the rest of the UHTCs. It is

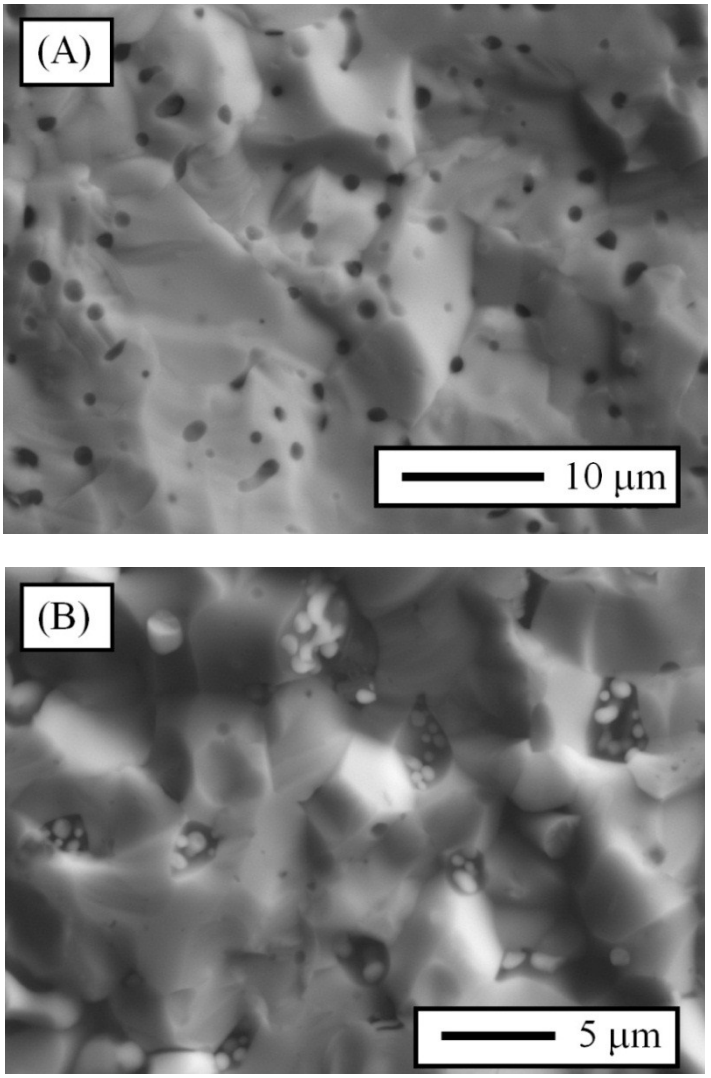

Figure. 4.5. Overleaf.

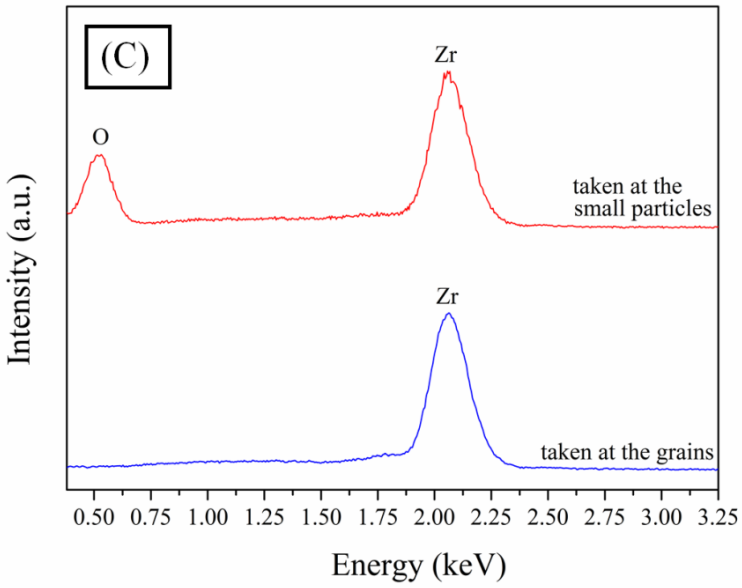

Figure. 4.5. SEM micrographs of the ZrB_2 UHTCs processed from the as purchased powder (A) and (B) the powder with 180 min of high-energy ball-milling. (C) Energy-dispersive X-ray spectra taken in spot mode on the grains and small particles in the SEM micrograph of Fig. 4.5.B.

observed in the SEM micrographs that the UHTCs fabricated from the ball-milled powders contain small particles located at grain boundaries and multigrain junctions. These were identified as being ZrO_2 by energy-dispersive X-ray analysis (see Fig. 4.5.C), and confirmed by XRD (not shown). The formation of ZrO_2 is consistent with the fact that the high-energy ball-milling was conducted in air, and therefore there is oxygen uptake on the crystal surfaces from 1.537 wt.% in the as-purchased condition to 4.514 wt.% after 180 min of high-energy ball-milling, as measured by the inert gas (helium) fusion method. Since these oxide impurities are known to favour coarsening over densification [2,3,17,21,22], it is reasonable to think that the kinetic effect of

the crystal size reduction is more pronounced than observed here. Indeed, that the oxidation uptake hinders densification can be seen clearly in Fig. 4.3 on comparing the last stretches in the densification curves of the powders ball-milled for 60 and 180 min. Finally, also evident comparing Fig. 4.5.A and B is that the grains are smaller with decreasing crystal size in the starting powder, although all the sintered UHTCs have micrometre-sized grains because the nanostructure of the ball-milled powders is not retained when sintering at 1900 °C.

Figure. 4.6 shows the maximum shrinkage rate (V_{MSR}) and the temperature at which this is reached (T_{MSR}), as determined from the time derivative of the shrinkage curves. The analysis of these data is also very interesting. It can be seen that V_{MSR} increases continuously with decreasing crystal size. However, the increase is first moderate from ~5 μm•s^{-1} up to ~6.4 μm•s^{-1} with reduction in crystal size from 2 μm down to 0.5 μm, and then there is a slight rise up to ~7 μm•s^{-1} as the crystal size is refined down to 100 nm, followed by an abrupt rise up to ~12 μm•s^{-1} as the crystal size decreases to 10 nm. It can be also seen in the figure that T_{MSR} decreases continuously with decreasing crystal size. In particular, the fall in T_{MSR} is only marginal from ~1810 to ~1750 °C as the crystal size decreases to 100 nm, but then falls abruptly to ~1550 °C as the crystal size is reduced to 10 nm. In solid-state sintered materials as in the present case, the maximum in the densification-rate curve is attributed to the change in the mechanism responsible for mass transport from surface diffusion to grain-boundary diffusion [23]. Surface diffusion produces neck growth and grain coarsening, but does not cause significant densification [20]. Grain-boundary diffusion, on the contrary, produces marked densification [20].

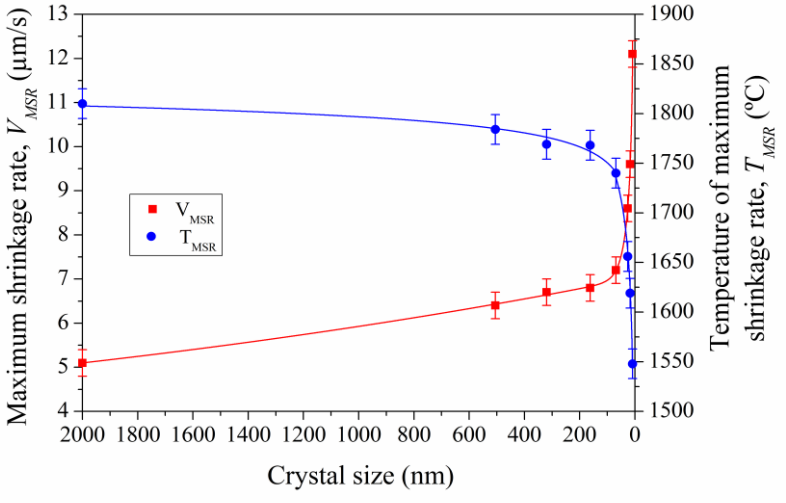

Figure. 4.6. Evolution of V_{MSR} and of T_{MSR} with the reduction in crystal size. The points are the experimental data, and the solid lines are merely to guide the eye.

It can thus be concluded that the high-energy ball-milling promotes greater grain-boundary diffusion in ZrB_2 at lower temperatures. This can be understood by considering that high-energy ball-milling refines the crystal sizes (see Fig. 4.1), shortening the diffusion distances of the Zr and B species and inducing the formation of a greater density of grain boundaries available as faster diffusion paths, and also activates them mechanically by introducing surface defects that also increase the diffusion coefficient [24]. Indeed, the temperature reduction with decreasing crystal size is an established fact in the framework of solid-state sintering theory [20]. Consider a powder with crystals of size D_1 that reaches a given degree of densification at temperature T_1. It has been demonstrated that with the change in crystal size from D_1 to D_2 this

powder will reach the same degree of densification at a temperature T_2 given by the expression [20]:

$$T_2 = \frac{1}{\left(\frac{1}{T_1}\right) - \left(\frac{km}{Q}\right)\ln\left(\frac{D_2}{D_1}\right)} \quad (4.1)$$

where k is universal gas constant, m is a constant that depends on the mass transport mechanism, and Q is the activation energy. If D_2 is less than D_1 then a reduction in the sintering temperature is predicted (i.e., $T_2 < T_1$). This is indeed the trend observed experimentally. Unfortunately, the activation energy of the grain boundary diffusion in ZrB_2, responsible for its densification, cannot be inferred from the data of T_{OIS}, T_{MSR}, or T_{OFS} because T_{OIS} is reached in the sintering regime controlled by surface diffusion, T_{MSR} is reached at different degrees of densification, and T_{OFS} is reached in many cases during the regime of isothermal heating at 1900 °C. To compute this activation energy, the temperature at which 80% of densification is achieved ($T_{80\%}$) was measured, and is also plotted in Fig. 4.4. The choice of $T_{80\%}$ is because, with the degree of densification being a constant, it falls within the regime of non-isothermal heating controlled by grain-boundary diffusion for all the powders except the as-purchased powder which will not be included in the calculations. Applying the above expression with m=4 for grain-boundary diffusion, the activation energy is found to be 2070 kJ/mol. This is a very high activation energy, which explains why the commercially-available ZrB_2 powders with micrometre-sized particles are considered to be intrinsically unsinterable without sintering additives at moderate temperatures.

Finally, it is worthwhile to discuss briefly the relevance and potential implications derived from the results and discussion. The present study reveals

that crystal size refinement enhances the SPS kinetics of ZrB_2 powders, and most likely that of pressureless sintering and hot-pressing, but that the enhancement is relevant only with reduction in crystal size down to the nanoscale. This underscores the importance of using high-energy ball-milling for the preparation of the ZrB_2 starting powders, since the nanoscale is not really achievable by conventional attrition milling. Furthermore, the shrinkage rate data are especially interesting because they suggest that it would in principle be possible to densify ZrB_2 UHTCs with minimal grain coarsening close to the temperature dictated by T_{MSR} as a function of the crystal size, if these powders were sufficiently isothermally soaked at such a temperature under the appropriate compaction pressure. One could then process ZrB_2 UHTCs both at lower temperatures than required today and with finer microstructures, both of which aspects are objectives being intensively pursued by the ceramics community. Elucidation of this expectation, however, requires further sintering studies on ZrB_2.

4.4. SUMMARY

The crystal-size dependence of the spark-plasma-sintering (SPS) kinetics of ZrB_2 ultra-high-temperature ceramics (UHTCs) was investigated. It was found that refining the starting powder enhances the SPS kinetics, reducing the onset temperatures of sintering and of the intermediate and final sintering regimes, as well as promoting a greater maximum shrinkage rate at lower temperatures. This enhancement was only relevant with reduction in

crystal size to the nanoscale. Finally, the implications for low-temperature sintering of ZrB_2 UHTCs are discussed.

4.5. REFERENCES

1) Wuchina, E., Opila, E., Opeka, M., Fahrenholtz, W. and Talmy, I. UHTCs: ultra-high temperature ceramic materials for extreme environment applications. Interface. 2007;16:30-6.

2) Fahrenholtz, W. G., Hilmas, G. E., Talmy, I. G. and Zaykoski, J. A. Refractory diborides of zirconium and hafnium. J Am Ceram Soc. 2007;90:1347-64, see also references therein.

3) Guo, S-Q. Densification of ZrB_2-based composites and their mechanical and physical properties: a review. J Eur Ceram Soc. 2009;29:995-1011, see also references therein.

4) Rahaman, M. N. Ceramic processing and sintering. Marcel Dekker: New York; 1995.

5) Thompson, M., Fahrenholtz, W. G. and Hilmas, G. Effect of starting particle size and oxygen content on densification of ZrB_2. J Am Ceram Soc. 2011;94:429-35.

6) Bellosi, A., Monteverde, F. and Sciti, D. Fast densification of ultra-high temperature ceramics by spark plasma sintering. Int J Appl Ceram Technol. 2006;3:32-40.

7) Nygren, M. and Shen, Z. Spark plasma sintering: possibilities and limitations. Key Eng Mater. 2004;264-268:719-24.

8) Munir, Z. A., Anselmi-Tamburini, U. and Ohyanagi, M. The effect of electric field and pressure on the synthesis and consolidation of materials: a review of the spark plasma sintering method. J Mat Sci. 2006;41:763-77.

9) Munir, Z. A., Quach, D. V. and Ohyanagi, M. Electric current activation of sintering: a review of the pulsed electric current sintering process. J Am Ceram Soc. 2011;94:1-19.

10) Orru, R., Licheri, R., Locci, A. M., Cincotti, A. and Cao, G. Consolidation/synthesis of materials by electric current activated/assisted sintering. Mat Sci Eng R. 2009;63:127-287.

11) Galán, C. A., Ortiz, A. L., Guiberteau, F. and Shaw, L. L. Crystallite size refinement of ZrB_2 by high-energy ball milling. J Am Ceram Soc. 2009;92:3114-7.

12) Galán, C. A., Ortiz, A. L., Guiberteau, F. and Shaw, L. L. High-energy ball milling of ZrB_2 in the presence of graphite. J Am Ceram Soc. 2010;93:3072-5.

13) Sánchez-Bajo, F., Ortiz, A. L. and Cumbrera, F. L. Analytical formulation of the variance method of line-broadening analysis for voigtian X-ray diffraction peaks. J Appl Crystallogr. 2006;39:598-600.

14) Guo, S-Q., Nishimura, T., Kagawa, Y. and Yang, J-M. Spark plasma sintering of zirconium diborides. J Am Ceram Soc. 2008;9:2848-55.

15) Zamora, V., Ortiz, A. L., Guiberteau, F., Shaw, L. L. and Nygren, M. On the crystallite size refinement of ZrB_2 by high-energy ball-milling in the presence of SiC. J Eur Ceram Soc. 2011;31:2407-14.

16) Fahrenholtz, W. G., Hilmas, G. E., Zhang, S. C., Zhu, S. Pressureless sintering of zirconium diboride: particle size and additive effects. J Am Ceram Soc. 2008;91:1398-404.

17) Chamberlain, A. L., Fahrenholtz, W. G. and Hilmas, G. E. Pressureless sintering of zirconium diboride. J Am Ceram Soc. 2006;89:450-6.

18) German, R. M. Powder metallurgy science. Princeton, NJ: Metal Powder Industries Federation; 1994.

19) Silvestroni, L., Bellosi, A., Melandri, C., Sciti, D., Liu, J. X. and Zhang, G. J. Microstructure and properties of HfC and TaC-based ceramics obtained by ultrafine powder. J Eur Ceram Soc. 2011;31:619-27.

20) German, R. M. Sintering theory and practice. Wiley: New York; 1996.

21) Dole, S. L., Prochazka, S. and Doremus, R. H. Microstructural coarsening during sintering of boron carbide. J Am Ceram Soc. 1989;72:958-66.

22) Zhang, S. C., Hilmas, G. E. and Fahrenholtz, W. G. Pressureless densification of zirconium diboride with boron carbide additions. J Am Ceram Soc. 2006;89:1544-50.

23) Shen, Z. and Nygren, M. Microstructural prototyping of ceramics by kinetic engineering: applications of spark plasma sintering. Chem Rec. 2005;5:173-84.

24) Suryanarayana, C. Mechanical alloying and milling. Prog Mater Sci. 2001;46:1-184.

"For every fact there is an infinity of hypotheses"

Robert Maynard Pirsig (1928)

Chapter V: Spark-Plasma Sintering of ZrB_2 Ultra-High-Temperature Ceramics at Lower Temperature Via Nanoscale Crystal Refinement

5.1. MOTIVATION

Zirconium diboride (ZrB_2) is one of the few compounds that can be classed as ultra-high-temperature ceramics (UHTC) [1]. Its favourable set of properties (among others, melting point 3250 °C, hardness 23 GPa, elastic modulus >500 GPa, electrical resistivity ~10^{-5} Ω•cm, and thermal conductivity >60 $W \cdot m^{-1} \cdot K^{-1}$) makes ZrB_2 a very attractive candidate material in the world of extreme environment engineering for such applications as hypersonic flight, scramjet and rocket propulsion, atmospheric re-entry, refractory crucibles, and plasma-arc electrodes, to cite just some [2,3].

It is widely recognized by the ceramics community that one of the greatest obstacles to the successful development and implementation of ZrB_2 UHTCs is their poor sinterability, to which various intrinsic and extrinsic factors contribute. The former include the strong covalent bonding, the low

self-diffusion coefficients, and the large particle sizes that together impose severe kinetic restrictions on the diffusion [2-5], and among the latter is contamination by surface oxides that favours the coarsening over the densification [2,3,5]. The strategy typically adopted to tackle the problem of ZrB_2's poor sinterability is to introduce sintering additives (either liquid phase formers, or reactive agents) together with the refinement of the starting powders by ball-milling (normally in the form of wet attrition milling) down to the submicrometre scale [2,3]. Regarding this latter point, in a recent study we investigated in detail the spark-plasma sintering (SPS) kinetics of ZrB_2 without additives as a function of the crystal size from a couple of micrometres down to a few nanometres (achieved by high-energy ball-milling), and concluded that the breakthrough needed to obtain ZrB_2 powders with unmatched sintering behaviour requires going beyond the simple refinement to the submicrometre scale, and that it is nanoscale crystal refinement which offers an unprecedented opportunity to significantly reduce the sintering temperature of ZrB_2 [6]. This latter expectation, which until now has not been confirmed experimentally, arises from the observation that only nanoscale crystal refinement promotes considerably greater grain-boundary diffusion at much lower temperatures in ZrB_2 [6], and this is the mass transport mechanism responsible for the material's densification. Elucidating this pending issue of the role of the crystal refinement scale in reducing the sintering temperature of ZrB_2 is thus a fundamental question requiring a prompt experimental response not only because lower-temperature sintering is one of the long sought for objectives in the field of UHTCs, but also because, if confirmed, it could have important implications regarding the comminution practices employed by the UHTC community.

With this in mind, the objective of the present work is to extend the previous kinetics study by conducting the first extensive set of SPS experimental measurements explicitly designed to explore by means of a detailed densification study the question of the crystal refinement scale in reducing the sintering temperature of ZrB_2. For this proof-of-concept study, we spark-plasma sintered six ZrB_2 powders with varied crystal sizes in the micrometre, submicrometre, and nanometre scales, without the introduction of sintering additives to thus investigate crystal-size effects without this interference. The details of the experiments and the major findings are described below.

5.2. EXPERIMENTAL PROCEDURE

5.2.1. Processing

The six ZrB_2 powders used in the present study were taken from the broader set of ZrB_2 powders utilized in the previous SPS kinetics study [6]. We shall thus here only summarize their preparation protocol. Briefly, the coarse powder with an average crystal size of 2 μm was obtained from a commercial source (Grade B, H.C. Starck, Berlin, Germany). The powders with submicrometre and ultra-fine crystals (~500 and 160 nm, respectively), and the three powders with nanometre crystals (~70, 25, and 10 nm) were prepared by subjecting intentionally the commercial ZrB_2 powder to high-energy ball-milling in air in a shaker mill (Spex 8000D, Spex CertiPrep, Metuchen, United States) for different times as required to reach the desired average crystal size [6], using WC balls as milling media with a ball-to-powder

weight ratio of 4:1. More details of the preparation and characteristics of these ZrB_2 powders can be found elsewhere [6-9]. However, it is also important to mention here that to prevent the powder contamination during high-energy ball-milling, a first milling cycle was carried out with the objective of depositing a thin film of ZrB_2 on the surface of the container and of the balls, and the resulting powder was thrown away. Then, the milling cycle was repeated utilizing the same container and balls, using the resulting powder for this study. With this milling procedure, (i) WC contamination was only detected in the powder ball-milled for 180 min, but not in the rest of powders, and in a minimal amount of ~0.9 vol.% according to the Rietveld analysis of the X-ray diffraction (XRD) pattern collected with a high-resolution diffractometer, and (ii) no Fe contamination was detected in any of the ball-milled powders [9].

The direct measurement carried out here through the weight loss of the balls indicates however that the contamination by WC is indeed lower than 0.5 vol.%. This WC contamination degree is about 4-6 times lower than that introduced typically with other common milling procedures, which is due to the combination of many factors such as the two-milling protocol adopted here, the low charge ratio (i.e., ball-to-powder weight ratio) of 4 used in this study, and the more than likely differences in other milling parameters (for example size, density, and surface roughness of the WC balls, wettability of the ZrB_2 powder towards the WC balls at the milling condition, extent of filling of the container, and milling atmosphere and environment, to name a few), as well as to the fact that the shaker mills operate with compressive forces whereas the attritors and the conventional mills function with a combination of shear and compressive forces.

5.2.2. Sintering

The different ZrB_2 powders were individually loaded into 12-mm diameter graphite dies lined with graphite foil and surrounded by a 1 cm thick graphite blanket to minimize heat loss, and were then spark-plasma sintered (Dr. Sinter SPS-2050, Sumitomo Coal Mining Co., Tokyo, Japan) in a dynamic vacuum atmosphere (i.e., 6 Pa). The graphite die has a wall thickness of 9 mm, and has a hole machined in its central region of 2.5 mm depth. Two types of SPS cycles were implemented: (i) heating at 100 °C/min up to the target temperature under 75 MPa pressure, and soaking at these conditions of temperature and pressure for a certain time (henceforth termed the simple SPS cycle), and (ii) heating at 100 °C/min up to the target temperature under 20 MPa pressure, followed by soaking at the target temperature under 75 MPa pressure for a certain time (henceforth termed the complex SPS cycle). Details of another SPS cycle used only sporadically will be given along with the corresponding results. For each ZrB_2 powder, the target temperature (measured by an optical pyrometer focused on the interior of hole of the graphite die[a]) was considered as a variable, setting its values in accordance with the reference of its transition temperature from surface diffusion to grain-boundary diffusion (T_{GBD}) determined in the previous kinetics study [6] (i.e., ~1550, 1650, 1740, 1765, 1785, and 1810 °C for the crystal sizes of 10,

[a] It is a well-known fact in SPS that the actual temperature inside the specimen is greater than the temperature measured by the optical pyrometer. However, a previous SPS study on HfB_2 and HfC [10], which have both thermal and electrical conductivities similar to ZrB_2, has shown that for the same graphite die and experimental configuration than used here the temperature mismatch is in the range 100-125 °C at 1700 °C and around 250 °C at 2200 °C. With this information, the temperature mismatch up to 1625 °C is estimated to be not greater than 50-75 °C.

25, 70, 160, 500, and 2000 nm, respectively). After the completion of the SPS cycle, the load was released and the electrical power was shut off to allow rapid cooling (in 1-2 min) to room temperature. The SPS furnace is equipped with a dilatometer of resolution better than 0.001 mm, connected to a computer to log the shrinkage curves. These curves were corrected for the expansion of the graphite parts (i.e., die, punches, and spacers) to give the real shrinkage curves of the powders themselves, and were then converted to densification curves by considering the relative densities of the sintered samples.

5.2.3. Microstructural Characterization

The sintered materials were examined by scanning electron microscopy (FE-SEM; S4800-II, Hitachi, Ibarakiken, Japan) to validate the porosity data, and also to observe their microstructure. The SEM observations were done on fracture surfaces, at 5 kV without metal coating.

5.3. RESULTS AND DISCUSSION

The T_{GBD} data obtained in the previous chapter of SPS kinetics study suggested that the ZrB_2 nano-powder with 10 nm crystals would exhibit the lowest sintering temperature of all the powders to be investigated here, for which reason the first set of SPS densification experiments were focused on this powder. Fig. 5.1 compares the densification curves as a function of time for this ZrB_2 nano-powder, obtained with the simple SPS cycle after 15 min of soaking at 1450, 1500, 1550, 1600, and 1625 °C. It is clear that the final degree of densification increases with increasing target temperature, from

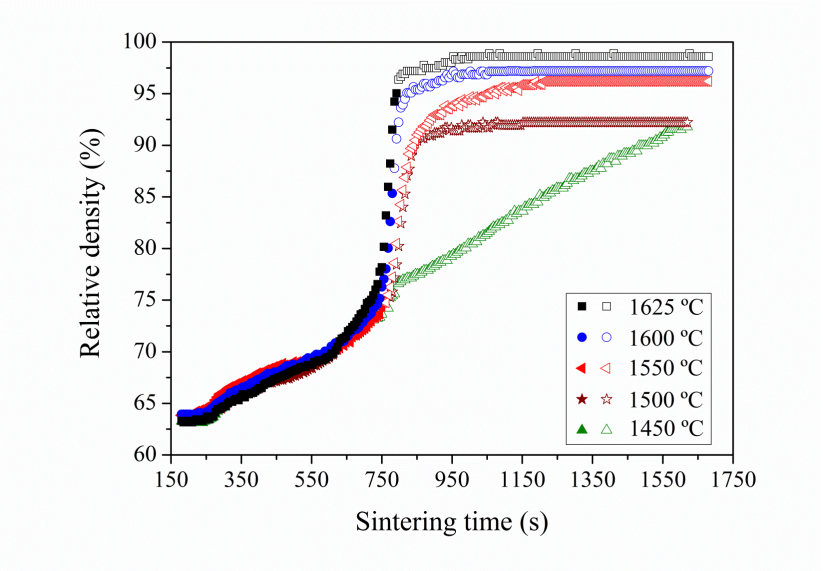

Figure. 5.1. Densification curves as a function of time for the ZrB_2 nano-powder with 10-nm crystals, obtained with the simple SPS cycle for target temperatures of 1450, 1500, 1550, 1600, and 1625 °C. Solid symbols correspond to data measured during the heating ramp up to the target temperature, and open symbols to data measured during the soaking.

~91% at 1450 °C to ~98.5% at 1625 °C. The latter can be considered to be a dense UHTC. Since the densification curve at 1625 °C stabilized after 3.5 min of isothermal soaking, there is no reason to prolong further the sintering as this would only cause coarsening. One notes that the target temperature of 1625 °C is fairly close to the corresponding value of T_{GBD} (~1550 °C), with only ~75 °C difference. Hence, these results confirm the possibility of densifying ZrB_2 UHTCs close to the temperature dictated by T_{GBD} under appropriate isothermal soaking. This trend was also evident in the direct examination of the microstructures by SEM, as illustrated by way of example

in the comparison of micrographs in Fig. 5.2 which shows incomplete densification at 1450 °C but pore absence at 1625 °C.

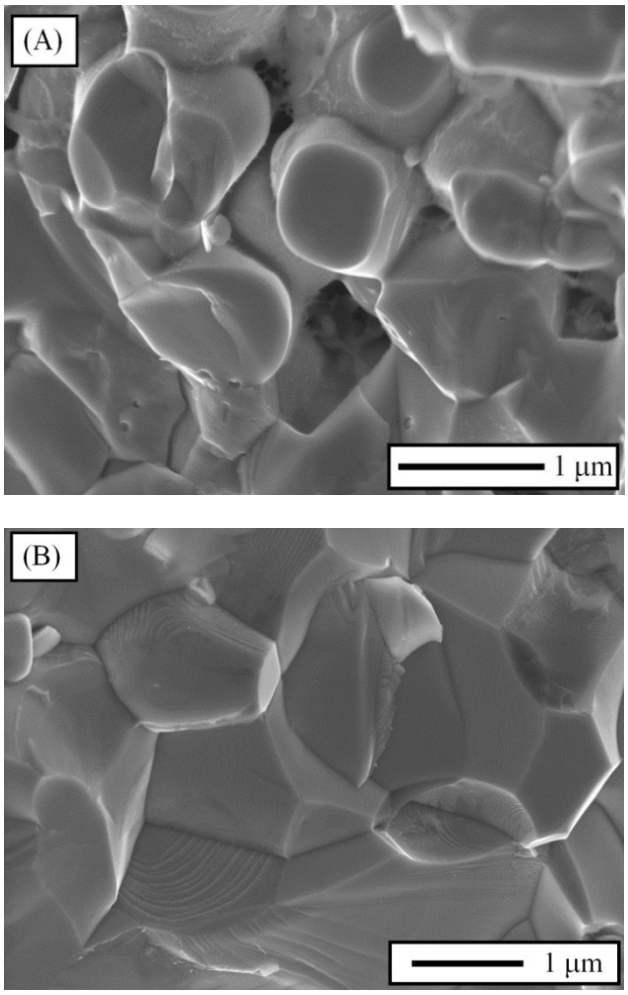

Figure. 5.2. SEM micrographs of the UHTCs fabricated from the ZrB_2 nano-powder with 10 nm crystals using the simple SPS cycle for 15 min at (A) 1450 °C and (B) 1625 °C.

In principle, it could be argued that this near-complete densification at a temperature as low as 1625 °C is assisted by the 0.5 vol.% WC contamination through the oxide removal reaction [11]:

$$ZrO_2 + 3WC \longrightarrow ZrC + 3W + 2CO(g)$$

since thermodynamic calculations indicate that this reaction is favourable above ~1260 °C under the vacuum of 6 Pa. To explore this possibility, because for example the reaction could not be kinetically favourable, the sample sintered at 1625 °C has been analysed by XRD. If the XRD pattern shows the presence of the reaction products ZrC and W, it could then be concluded that WC plays a role; otherwise, there is no role played by WC. The XRD pattern of the sample sintered at 1625 °C in Fig. 5.3 shows, beside the ZrB_2 peaks, the presence of ZrO_2 and WC peaks (i.e., of the reactants) but not of ZrC or W peaks (i.e., of the reaction products). Other reduction reactions of ZrO_2 by WC would also lead to the formation of ZrC, which is not observed here. Thus, this XRD analysis reveals the absence of role played by WC during the present SPS treatment, and, consequently, indicates that the near-complete densification observed at 1625 °C must be attributed to the crystal size refinement of the starting powder down to the low nanoscale.

Another interesting observation in Fig. 5.1 is that all the densification curves reached the plateau after several minutes of isothermal soaking, except the curve obtained at 1450 °C which has still not flattened out after 15 min. In this last case, it appeared that the ZrB_2 nano-powder would have densified further with a more prolonged soaking at 1450 °C. Consequently, we measured the densification curve of the ZrB_2 nano-powder at 1450 °C until the stabilization of the graphite punches. The result is shown in Fig. 5.4.

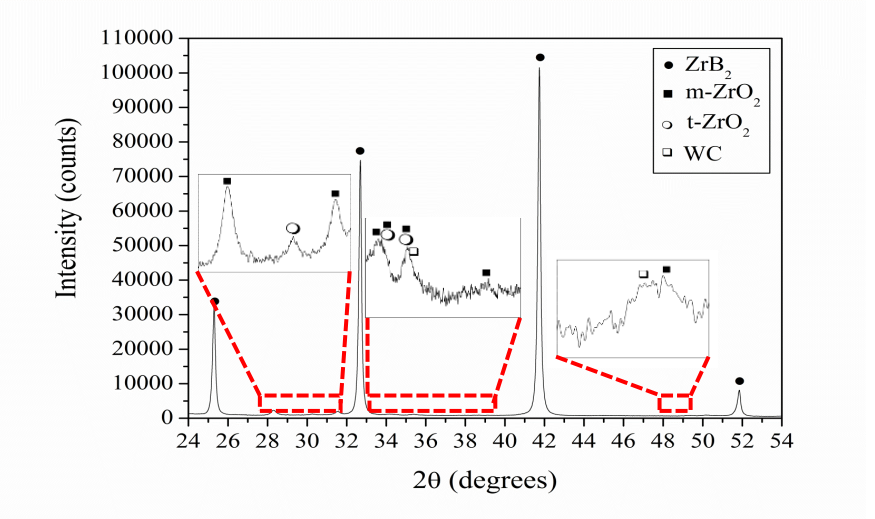

Figure. 5.3. X-ray diffraction pattern of the UHTC fabricated from the ZrB_2 nano-powder with 10 nm crystals using the simple SPS cycle at 1625 °C for 15 min. The insets show magnificated regions in logarithmic Y-scale to facilitate the appreciation of the weak ZrO_2 and WC peaks.

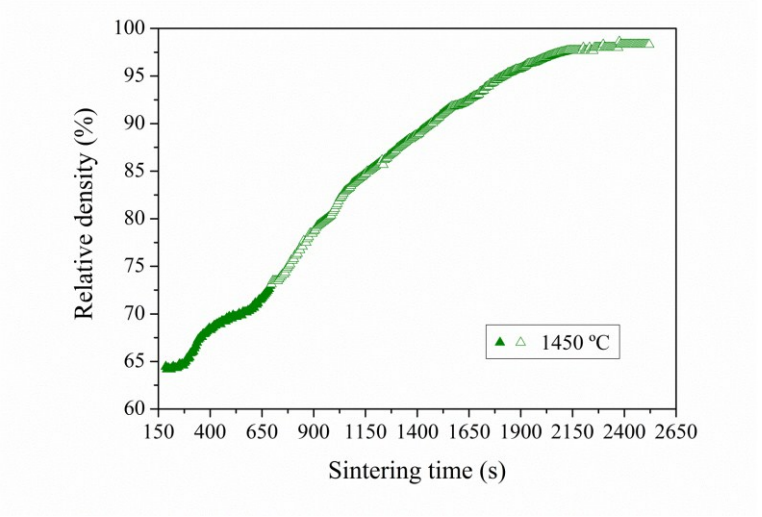

Figure. 5.4. Densification curve as a function of time for the ZrB_2 nano-powder with 10 nm crystals, obtained with the simple SPS cycle for a target temperature of 1450 °C. The closed symbols correspond to data measured during the heating ramp up to 1450 °C, and the open symbols to data measured during the soaking at 1450 °C.

This measurement indicates that ~98% relative density can be reached with the simple SPS cycle after 30 min at 1450 °C. Interestingly, this is almost the same final degree of densification reached at 1625 °C (~98.5%), and is slightly greater than those reached at 1550 (~96%) and 1600 °C (~97%) and much greater than that at 1500 °C (~92%), in all cases after the corresponding curve stabilization. This was an unexpected finding because it is not what we would have predicted considering simply that the diffusion coefficients obey an Arrhenius-type law [12]. Therefore, to shed light on this question, we examined by SEM the sample fabricated at 1450 °C. As one observes in the micrograph of Fig. 5.5, the detailed SEM observations revealed that some grain faces exhibit what appears to have been a liquid phase.

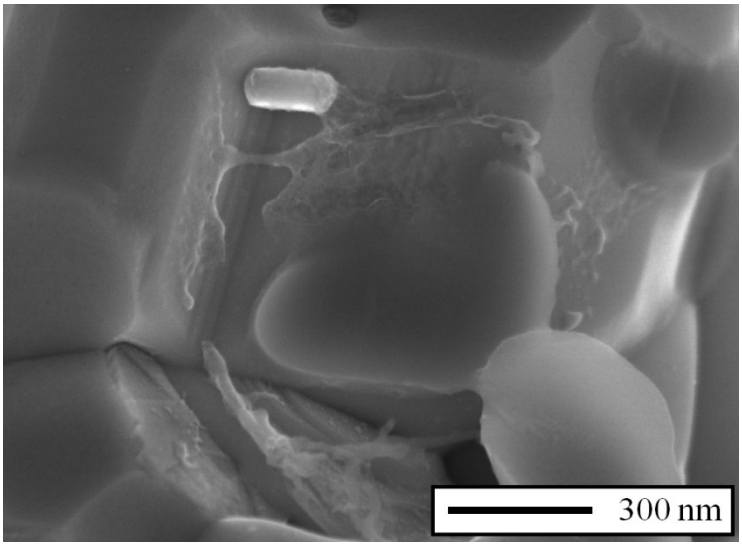

Figure. 5.5. High-magnification SEM micrograph of the UHTC fabricated from the ZrB_2 nano-powder with 10 nm crystals using the simple SPS cycle at 1450 °C for 30 min.

We believe that this liquid is boria, and that it is responsible for the unexpected anomalously high densification at 1450 °C because the presence of liquid boria facilitates not only grain sliding but also mass transport. This boria forms because the high-energy ball-milling was done in air, so that ZrB_2 can oxidize superficially during the milling, and also because the resulting ZrB_2 nano-powder passivates spontaneously in contact with air [13]. The evolution of the vacuum level during the SPS test at 1450 °C supports the presence of liquid boria deduced from the SEM observations. Thus, the vacuum level hardly changed throughout the experiment (almost constant at ~6 Pa), indicating that no detectable boria gas emission occurred at 1450 °C and therefore that boria remained in the liquid state. This scenario was, however, totally different during the SPS experiments at higher temperatures in which gas release was indeed detected, with the vacuum level temporarily dropping a couple of Pa or more and then recovering its initial level. Given this information , it is reasonable to conclude that, despite the SPS at 1450 °C eventually resulting in near-complete densification, this low-temperature densification is not useful because the residual boria will make the resulting ZrB_2 material degrade in service when exposed to ultra-high-temperature applications. Thus, 1625 °C continues to be the best SPS temperature.

Since the objective pursued is the lower-temperature SPS of boria-free ZrB_2 UHTCs, the following step was to focus on the possible optimization of the SPS cycle between 1450 and 1625 °C. The SEM observations such as that shown in Fig. 5.6 for the UHTC processed at 1500 °C indicated that the residual pores in the UHTCs fabricated with the simple SPS cycle have a near-perfect spherical shape, thus suggesting that they originated from the slow outward diffusion of the boria gas occluded when the pore distribution

transformed very rapidly from open porosity to closed porosity in the presence of pressure [b]. In consequence, one possible manner of facilitating the escape of the boria gas generated would be to apply a lower compaction pressure during the heating ramp in order to delay the collapse of the open pore structure so that the gasses can leave the sample more easily.

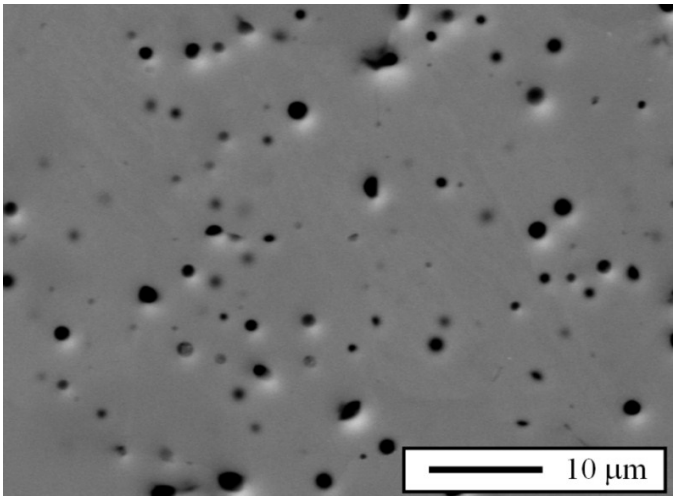

Figure. 5.6. Low-magnification SEM micrograph of the UHTC fabricated from the ZrB_2 nano-powder with 10 nm crystals using the simple SPS cycle at 1500 °C for 15 min.

To explore this possibility, we performed new experiments using the complex SPS cycle described in the experimental procedure. Fig. 5.7 shows the resulting densification curves as a function of time for the ZrB_2 nano-

[b] According to solid-state sintering theory, the transformation from open porosity to closed porosity occurs during the intermediate stage of sintering, which covers normally the interval of relative densities between 70 and 90% [14]. Thus, 90% densification represents typically the onset of the final stage of sintering, which is the sintering regime where the closed porosity is eliminated [14]. Consequently, 90% relative density will henceforth be taken to be the moment of the collapse of the open pore structure.

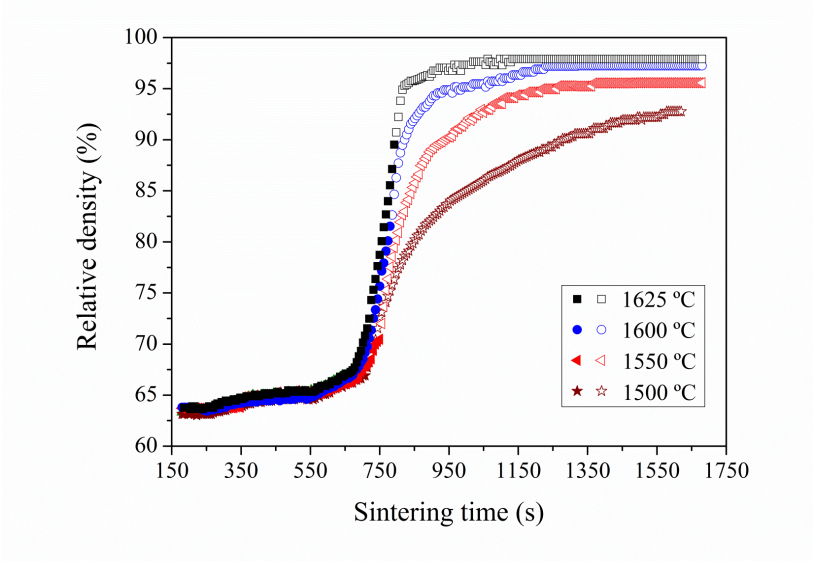

Figure. 5.7. Densification curves as a function of time for the ZrB_2 nano-powder with 10 nm crystals, obtained with the complex SPS cycle for target temperatures of 1500, 1550, 1600, and 1625 °C. The closed symbols correspond to data measured during the heating ramp up to the target temperature, and the open symbols to data measured during the soaking.

powder obtained with the complex SPS cycle after 15 min of soaking at 1500, 1550, 1600, and 1625 °C. Recall that the temperature of 1450 °C had been excluded from further analysis due to the undesired presence of residual boria in the microstructure. As can be observed in Fig. 5.7, these curves exhibit the same trend as was seen before in Fig. 5.1, with the final degree of densification increasing with increasing target temperature. The comparison between the densification curves obtained with the simple and complex SPS cycles is very interesting however. One can infer that in all cases the densification was better during the first moments (i.e., approximately the first 750 s) with the simple SPS cycle doubtless due to the greater compaction pressure (75 vs 20 MPa), but that the ultimate densification was essentially the

same with both cycles (i.e., ~92.5% at 1500 °C, 96% at 1550 °C, 97% at 1600 °C, and 98% at 1625 °C). One can thus conclude that the complex SPS cycle by itself is not effective in improving the final degree of densification. Neither does the complex SPS cycle seem to affect appreciably the grain size, as deduced by comparing for example the SEM micrograph in Fig. 5.8 for the sample fabricated with the complex cycle at 1625 °C with the corresponding micrograph in Fig. 5.2.B for the simple SPS cycle.

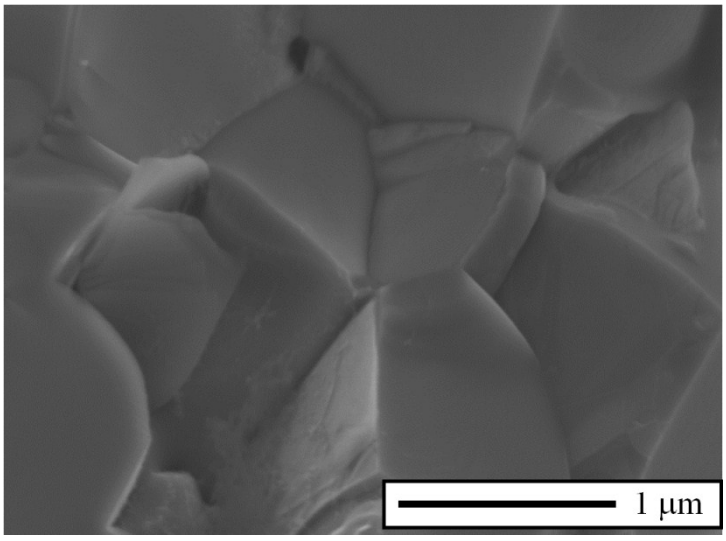

Figure. 5.8. SEM micrograph of the UHTC fabricated from the ZrB_2 nano-powder with 10 nm crystals with the complex SPS cycle at 1625 °C for 15 min.

These observations indicate that the microstructure (i.e., porosity and grain size) is dictated essentially by the high-pressure/high-temperature stretch. Nevertheless, comparison of the curves of Figs. 5.1 and 5.7 merits further attention. Clearly, one sees that, except for the above-mentioned differences

during the first moments of SPS, the shapes of the densification curves at 1550, 1600, and 1625 °C are otherwise very similar for the two SPS cycles, and that at these temperatures the use of the complex SPS cycle does little to delay the end of the collapse of the open pore structure (i.e., by ~90, 30 and 20 s, respectively). Consistent with this scenario, we measured at 1550, 1600, and 1625 °C only a marginal difference between the evolution of the vacuum levels during the simple and complex SPS cycles. The 1500 °C densification curves exhibit, however, a relevant variation in shape since, with the complex SPS cycle, the approach to the limiting value of ~92.5% is far more gradual. Indeed, the open pore structure collapses much later (i.e., ~500 s later). Interestingly, we now indeed noted at 1500 °C a relevant difference in the boria emission. In particular, with the complex SPS cycle not only was the gas emission peak 2 Pa more intense and longer lasting than with the simple SPS cycle, but at 1500 °C the same level was reached as at 1625 °C with the simple SPS cycle despite the temperature being 125 °C lower. Unfortunately, despite the better elimination of boria gas at 1500 °C with the complex SPS cycle, the final densification degree reached was still only moderate due to the insufficient diffusion at that temperature. Considering all these analyses together, we decided to test a two-step SPS cycle with a first step at 1500 °C for ~10 min under a moderate pressure of 20 MPa to eliminate the boria impurities while densifying the compact up to ~90% relative density with little coarsening, followed by a shorter second step at 1600 °C under a higher pressure of 75 MPa to promote the complete pore elimination.

These expectations were indeed borne out experimentally because, as shown in the densification curve of Fig. 5.9 and in the SEM micrograph of Fig. 5.10, a fully dense ZrB_2 compact was obtainable with this two-step SPS

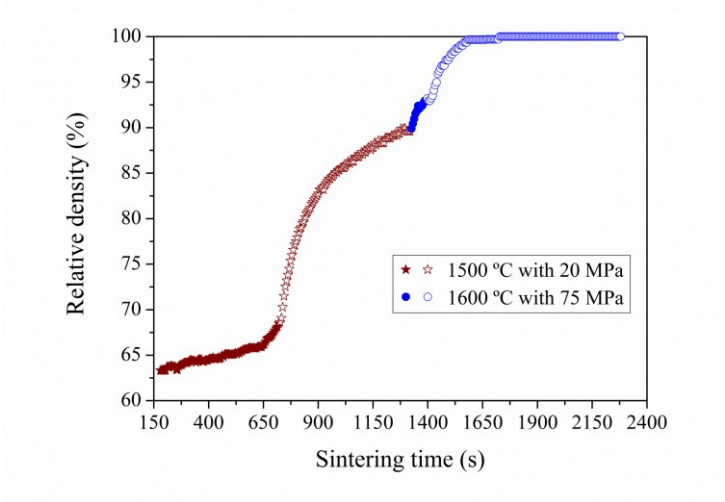

Figure. 5.9. Densification curves as a function of time for the ZrB_2 nano-powder with 10 nm crystals, obtained with the two-step SPS cycle comprising a first simple SPS cycle under 20 MPa pressure with a target temperature of 1500 °C, followed by a second complex SPS cycle with a target temperature of 1600 °C. The closed symbols correspond to data measured during the heating ramp up to the target temperatures, and the open symbols to data measured during the corresponding soakings.

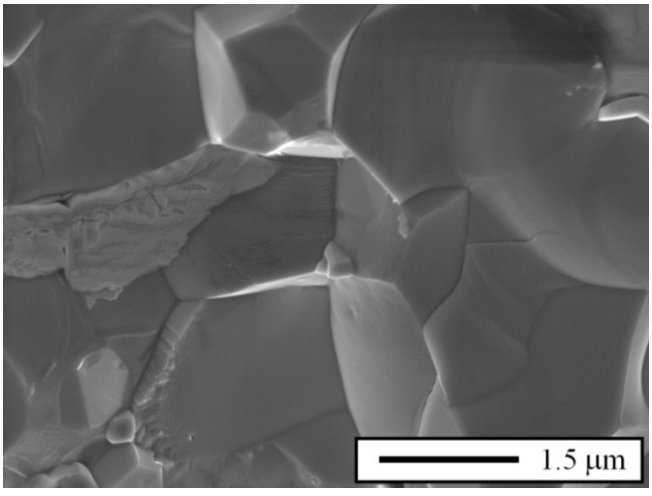

Figure. 5.10. SEM micrograph of the UHTC fabricated from the ZrB_2 nano-powder with 10 nm crystals with the two-step SPS cycle at 1600 °C for 15 min.

cycle. Note that, although this present proposal of a two-step cycle and the one typically used to process nano-ceramics pursue the same objective of densification with little grain boundary migration, their procedures are reversed with respect to each other [15]. In the latter, the powder is first heated at the high temperature for a short period, and then rapidly cooled to a lower temperature and maintained there for a long period. In the present case the main concern is to eliminate the boria impurities, which requires a "smooth" intermediate stage of sintering, while in the typical nano-ceramics processing case the principal concern is inhibition of grain growth, which requires a "smooth" final stage of sintering.

To put the ZrB_2 nano-powder with 10 nm crystals results into perspective, in the following we shall compare the above SPS data with those of ZrB_2 powders with larger crystal sizes of ~25, 70, 160, 500, and 2000 nm. Given that the experimental observations indicated that the simple and complex SPS cycles yielded eventually the same degree of densification and similar microstructure, the SPS experiments for these ZrB_2 powders with larger crystal sizes were conducted using only the simple SPS cycle which was clearly sufficient for the purposes of the present comparative study. Fig. 5.11 is a comparison of the lowest-temperature densification curves for all these ZrB_2 powders, with the lowest temperature being that which satisfied the condition of reaching at least 95% densification. Note that the measurements of the data comprising these curves required many SPS experiments to be carried out at different temperatures for each of these ZrB_2 powders in the same way as was done previously for the nano-powder with 10 nm crystals, although, for the sake of brevity, these densification curves will not be presented. As one observes, the curves in Fig. 5.11 demonstrate clearly that the crystal size

refinement progressively reduces the SPS temperature of ZrB_2, and also that the reduction is only moderate with the refinement to the ultra-fine range, but very marked with the the ZrB_2 nano-powder with 10 nm crystals reached 96%

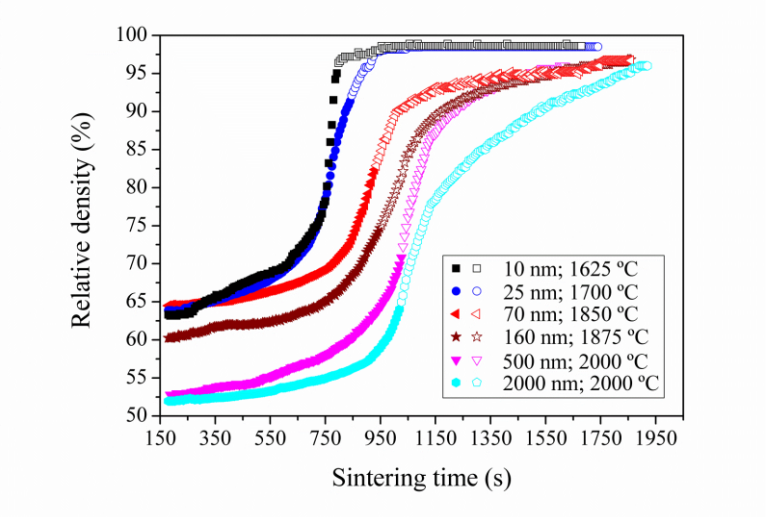

Figure. 5.11. Densification curves as a function of time for the ZrB_2 coarse, submicrometre, ultra-fine, and nanometre powders, obtained with the simple SPS cycle at the lowest target temperatures that resulted in final densification degrees greater than 95%. The closed symbols correspond to data measured during the heating ramp up to the corresponding target temperature, and the open symbols to data measured during the soaking. The fact that the degree of densification at the onset of the SPS cycle first increases and then decreases is simply because the powder's mechanical-packing density scales inversely with the particle sizes, not with the crystal sizes, and the nano-crystals achieved with the long-time high-energy ball-milling are actually agglomerated [6,8,9].

densification at 1550 °C, which is the densification reached by the micrometre and submicrometre powders at 2000 °C (see Fig. 5.11), one can thus conclude that the nanoscale crystal refinement reduced the SPS temperature by not less than 450 °C for the typical crystal sizes of the most-widely used ZrB_2 powders. This reduction is very relevant because it is similar

to or even greater than the temperature reductions previously achieved with the aid of former liquid-phase sintering additives (for example with $MoSi_2$ or with $TaSi_2$) [2,3]. In addition, there was no attempt here to prevent oxygen contamination (which is known to promote coarsening [2,3,4,16,17]) by use of an inert atmosphere during the milling, suggesting that there could be still room for further reductions in the sintering temperature, but at the expense of making the comminution routine more tedious and costly. Another additional benefit of the nanoscale crystal refinement is that it allows fine-grained microstructures to be obtained (see Figs. 5.2.B, 5.8, and 5.10) instead of the coarse-grained microstructures resulting from the sintering of the typical micrometre or submicrometre starting powders (Fig. 5.12), an aspect that is very important to provide the ZrB_2 UHTCs with superior strength [2,3].

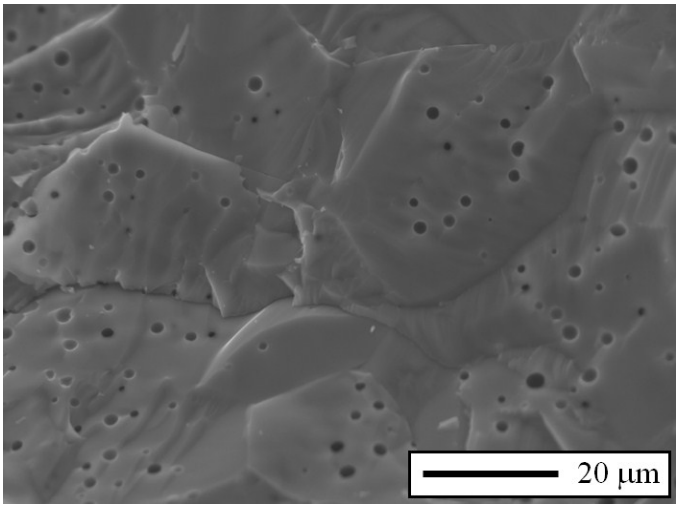

Figure. 5.12. SEM micrograph of the UHTC fabricated from the submicrometre ZrB_2 powder with 0.5 μm crystals with the simple SPS cycle at 2000 °C for 15 min.

Finally, the present study has interesting implications for comminution practices in the UHTC community. In particular, it emerges that the preparation of ZrB_2 powders with unequalled sintering behaviour necessarily requires the use of high-energy ball-milling because the typical wet attrition milling, which has so far been the gold-standard comminution treatment, is a form of conventional milling that does not generate the high compressive stresses in the ball-to-ball collisions needed to refine the crystal sizes down to nanoscale. This, however, does not rule out attritor use because this technique can also function as a high-energy ball-mill if operated in dry with a high ball-to-powder ratio (> 40:1) and with a high peripheral speed of the agitator (> 3 m/s). This would be another way of achieving the nanoscale crystal refinement needed to make the lower-temperature sintering of ZrB_2 possible.

5.4. SUMMARY

We have explored the feasibility of reducing the spark-plasma-sintering (SPS) temperature of additive-free ZrB_2 ultra-high-temperature ceramics (UHTCs) via crystal size refinement of the starting powder down to the low nanoscale. We found that under otherwise the same SPS conditions (75 MPa pressure, and 100 °C/min heating ramp) nanoscale ZrB_2 can be densified at temperatures about 450 °C lower than for the typical micrometre and submicrometre ZrB_2 powders, and at least 250 °C below the ultra-fine powder temperature. Furthermore, the nanoscale crystal refinement also promotes the production of fine-grained ZrB_2 UHTCs. We also found that elimination of the B_2O_3 impurities plays an important role in the complete

densification. The unequalled sinterability of the nanoscale ZrB_2 powders highlights the need to use high-energy ball-milling for the comminution of the typical commercially available ZrB_2 powders.

5.5. REFERENCES

1) Wuchina, E., Opila, E., Opeka, M., Fahrenholtz, W., Talmy, I. UHTCs: ultra-high temperature ceramic materials for extreme environment applications. Interface. 2007;16:30-6.

2) Fahrenholtz, W. G., Hilmas, G. E., Talmy, I. G. and Zaykoski, J. A. Refractory diborides of zirconium and hafnium. J Am Ceram Soc. 2007;90:1347-64.

3) Guo, S-Q. Densification of ZrB_2-based composites and their mechanical and physical properties: a review. J Eur Ceram Soc. 2009;29:995-1011.

4) Telle, R., Sigl, L. S. and Takagi, K. Boride-based hard materials. In: Riedel R, editor. Handbook of ceramic hard materials, vol. 2. Weinheim: Wiley-VCH; 2000. 802-945.

5) Thompson, M., Fahrenholtz, W. G. and Hilmas, G. Effect of starting particle size and oxygen content on densification of ZrB_2. J Am Ceram Soc. 2011;94:429-35.

6) Zamora, V., Ortiz, A. L., Guiberteau, F. and Nygren, M. Crystal-size dependence of the spark-plasma-sintering kinetics of ZrB_2 ultra-high-temperature ceramics. J Eur Ceram Soc. 2012;32:271-6.

7) Galán, C. A., Ortiz, A. L., Guiberteau, F. and Shaw, L. L. Crystallite size refinement of ZrB_2 by high-energy ball-milling. J Am Ceram Soc. 2009;92:3114-7.

8) Galán, C. A., Ortiz, A. L., Guiberteau, F. and Shaw, L. L. High-energy ball milling of ZrB_2 in the presence of graphite. J Am Ceram Soc. 2010;93:3072-5.

9) Zamora, V., Ortiz, A. L., Guiberteau, F., Shaw, L. L. and Nygren, M. On the crystallite size refinement of ZrB_2 by high-energy ball-milling in the presence of SiC. J Eur Ceram Soc. 2011;31:2407-14.

10) Sciti, D., Guicciardi, S. and Nygren, M. Densification and mechanical behavior of HfC and HfB_2 fabricated by spark plasma sintering. J Am Ceram Soc. 2008;91:1433-40.

11) Fahrenholtz, W. G., Hilmas, G. E., Zhang, S. C. and Zhu, S. Pressureless sintering of zirconium diboride: particle size and additive effects. J Am Ceram Soc. 2008;91:1398-404.

12) Mehrer, H. Diffusion in solid metals and alloys. Springer-Verlag; 1990.

13) Ortiz, A. L., Zamora, V. and Rodríguez-Rojas, F. A study of the oxidation of ZrB_2 powders during high-energy ball-milling in air. Ceram Int. 2012;38:2857-63.

14) German RM. Sintering theory and practice. Wiley: New York; 1996.

15) Chen, I-W. and Wang, X-H. Sintering dense nano-crystalline ceramics without final stage grain growth. Nature. 2000;404:168-71.

16) Chamberlain, A. L., Fahrenholtz, W. G. and Hilmas, G. E. Pressureless sintering of zirconium diboride. J Am Ceram Soc. 2006;89:450-6.

17) Zhang, S. C., Hilmas, G. E. and Fahrenholtz, W. G. Pressureless densification of zirconium diboride with boron carbide additions. J Am Ceram Soc. 2006;89:1544-50.

"Bad times have a scientific value. These are occasions a good learner would not miss"

Ralph Waldo Emerson (1803-1882)

Chapter VI: In Situ Formation of ZrB_2-ZrO_2 Ultra-High-Temperature Ceramic Composites from High-Energy Ball-Milled ZrB_2 Powders

6.1. MOTIVATION

Zirconium diboride (ZrB_2) is an ultra-high-temperature ceramic (UHTC) that generates great interest in the aerospace sector, in particular for the protection of vehicle aerosurfaces exposed to high-flow environments of hot oxidizing gases, as is the case in hypersonic flights and atmospheric re-entry [1,2]. However, ZrB_2 alone is very brittle and does not have sufficient toughness, strength, and thermal shock resistance to be used successfully for such aerospace applications [1,2]. Reducing this inherent brittleness has thus become a critical issue to ensure the mechanical integrity of ZrB_2 UHTCs when they are in service. The strategy adopted to achieve this goal consists of engineering the microstructure of the ZrB_2 UHTCs, normally by the addition of second phases [1-26] and sometimes also by the fabrication of laminated-type architectures with compressive residual stresses [27-29] or of

complex cell-type architectures [30]. SiC is the typical second phase particle in ZrB_2 [1-3], and its introduction improves the toughness because of the crack defection and crack wake bridging in the weak ZrB_2-SiC interfaces. The addition of SiC also enhances the strength of ZrB_2 because SiC inhibits grain growth thus reducing the dominant initial flaw size. Other ceramic second phases such as $MoSi_2$, ZrC, HfN, and TiN [1,2,4], or combinations of various second phases [1,2,4-7], that improve densification may also inhibit grain growth improving the strength and toughness of the material. However, ductile Nb and Mo metal particles have also been added to ZrB_2 [8,9], which has been observed to favour crack deflection and branching as well as to promote stress relaxation near the crack tip [8]. The incorporation of high aspect ratio reinforcements, such as for example carbon fibres [10,11] and nanotubes [12], graphite flakes [13-16], and SiC whiskers [17-20], fibres [17,18], or platelets [21] further reduces the brittleness of the ZrB_2-based composites, which is attributed to the combination of debonding, pull-out, and bridging of these reinforcements as well as enhanced crack deflection and crack pinning. Finally, another interesting strategy lies in dispersing within the ZrB_2 matrix a second phase with phase-transformation capability, such as ZrO_2 [22-26]. Thus, it has been demonstrated that the ZrB_2-ZrO_2 composites exhibit *R*-curve behaviour while pure ZrB_2 ceramics do not [22-24], resulting from crack bridging and the stress-induced martensitic transformation in ZrO_2.

So far, the ZrB_2-ZrO_2 particulate composites have been fabricated from mixtures of ZrB_2 and ZrO_2 powders (the preparation of which involves comminution, wet homogenization, and slurry drying) that are densified by hot-pressing resulting in a duplex ceramic microstructure. In this context, here a simpler route is reported that results in the in situ formation of fine-grained

ZrB_2 UHTCs containing evenly distributed ZrO_2 of uniform size located at triple joints and grain boundaries of the ZrB_2 grains. The formation of these ZrB_2-ZrO_2 composites was discovered during the spark-plasma sintering (SPS) of ZrB_2 powders refined by high-energy ball-milling in air. The technique of SPS is similar to the more classical hot-pressing in that both apply uniaxial load, although SPS has the advantage that the pulsed electrical current heats the die (and the compact if the powder is electrically conductive) directly, and the rapid sintering cycles enable a better control of the final microstructure and therefore of the properties of the resulting material [31]. The objective of the present study is to describe the in situ formation mechanism of these ZrB_2-ZrO_2 UHTC composites, and to propose how these and other ZrB_2-oxide UHTC composites could be processed more controllably in the future.

6.2. EXPERIMENTAL PROCEDURE

6.2.1. Processing

The ZrB_2 starting powder was obtained from a commercial source (Grade B, H.C. Starck, Berlín, Germany). This ZrB_2 powder has a purity of 96-97% according to the manufacturer specification and an oxygen content of 1.5 wt.% based on the measurement by fusion in inert gas, and consists of micrometre particles with an average size of 2-3 μm. To reduce its particle size, the as-received ZrB_2 powder was subjected to high-energy ball-milling in air for 180 min in a shaker mill (Spex 8000D, Spex CertiPrep, Metuchen, United States) operated at about 1060 back-and-forth cycles per minute. The milling was carried out in a cylindrical hardened-steel container with WC balls

(6.7 mm in diameter; Union Process Inc., Akron, United States) under a ball-to-powder weight ratio of 4:1 [1]. This experimental milling condition has been proved to be effective in refining ZrB_2 to nano-crystallites with ~10 nm average size [32-34], as is also shown here in the transmission electron microscopy (TEM) images of Fig. 6.1.

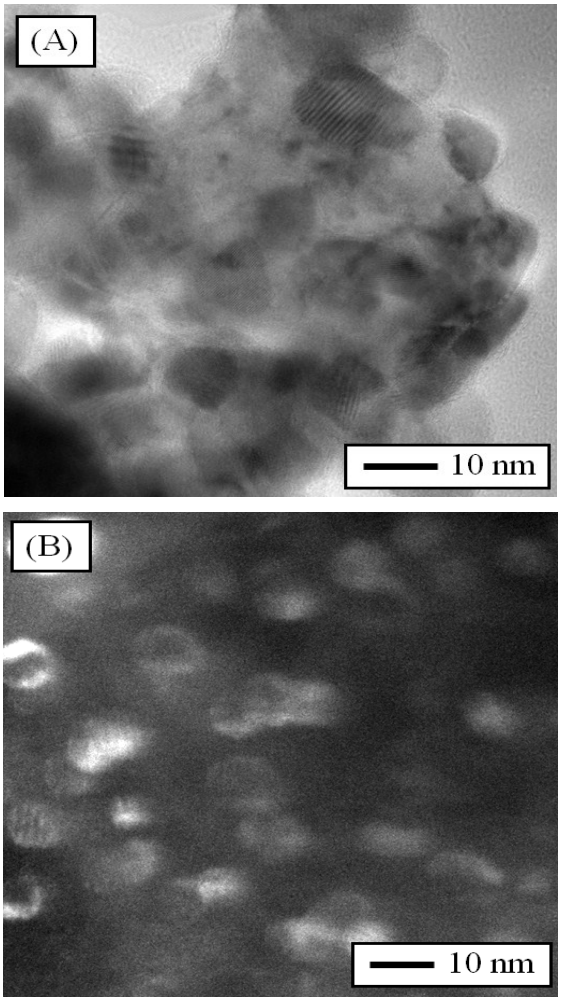

Figure. 6.1. (A) TEM bright-field image and (B) TEM dark-field image of the ZrB_2 powder with 180 min of high-energy ball-milling in air, showing both primary nanoparticles with ~10 nm size.

6.2.2. Sintering

The ball-milled ZrB_2 powder, which contains 4.5 wt.% oxygen according to the measurement by fusion in inert gas and 2.5 wt.% WC (taken from milling media) according to the X-ray diffraction (XRD) analysis [34], was then spark plasma sintered (Dr. Sinter SPS-2050, Sumitomo Coal Mining Co., Tokyo, Japan) at 1900 °C with 75 MPa for 3 min in a dynamic vacuum (i.e., ~6 Pa), within a graphite die lined with graphite foil and surrounded by a 1 cm thick graphite blanket to minimize the heat loss. The heating ramp was set at 200 °C/min with 50 MPa up to 1200 °C, and at 100 °C/min with 75 MPa from 1200 to 1900 °C. The application of the 50 MPa pressure was done at room temperature, and at 1200 °C the pressure was increased rapidly up to 75 MPa at a rate of 2 MPa/s. After the completion of the sintering cycle, the load was released and the electrical power was shut off to allow rapid cooling to room temperature (i.e., in 1-2 min). The density of the resulting ceramic was measured using the Archimedes principle with distilled water as the immersion medium.

6.2.3. Microstructural Characterization

The microstructural characterization was performed by the combination of scanning electron microscopy (SEM; S-3600N, Hitachi, Ibarakiken, Japan), energy dispersive X-ray spectroscopy (EDXS; XFLASH Detector 3001, Röntec GmbH, Germany), and XRD (D8 Advance, Bruker AXS, Karlsruhe, Germany), using in all cases routine procedures applicable to ceramics materials.

6.2.4. Mechanical Test

The hardness (H) and toughness (K_{IC}) were evaluated by Vickers-indentation tests (98 N load, P), using standard formulae for the calculations (i.e., $H = P/2a^2$ and $K_{IC} = 0.016(E/H)^{0.5}P \cdot c^{-1.5}$, where 2a and 2c are the diagonals and radial-crack diameters (surface traces) of the indents, respectively, and E is the Young modulus which is 517 GPa for this ZrB_2-ZrO_2 composite) [35]. The tests were done at room temperature using a conventional hardness tester (Shimadzu HSV-30 (Shimadzu Corp., Kyoto, Japan) equipped with a diamond pyramid.

A reference material was also prepared by spark-plasma sintering the as-received ZrB_2 powder under identical experimental conditions as used for the ball-milled ZrB_2 powder. Furthermore, its microstructure and mechanical properties were determined similarly as well to be utilized as a comparison baseline. The Young modulus of this ZrB_2 monolith used for calculation of its toughness is 540 GPa.

6.3. RESULTS AND DISCUSSION

Figure 6.2.A shows a representative SEM micrograph of the UHTC fabricated from the 180-min ball-milled ZrB_2 powder. The average ZrB_2 grain size is ~5 μm, which is relatively small compared to the ~15 μm grain size of the reference ZrB_2 monolith prepared from the as-received ZrB_2 powder (Fig. 6.2.B). The reference monolith contains pores located at triple joints, grain edges, and especially within the grains, as seen more clearly in the optical micrograph of Fig. 6.3.

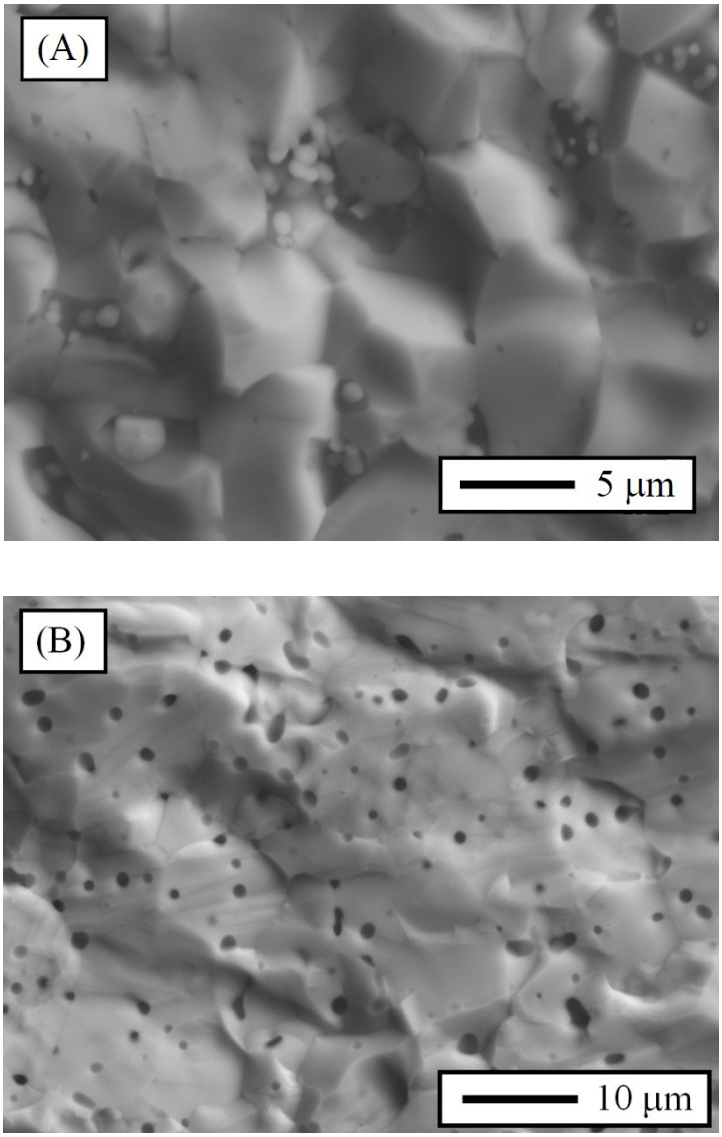

Figure. 6.2. SEM micrographs (taken with backscattered electrons from the fracture surface) of the ZrB_2 UHTCs processed from (A) the powder subjected to 180 min of high-energy ball-milling in air, and (B) the as-received powder.

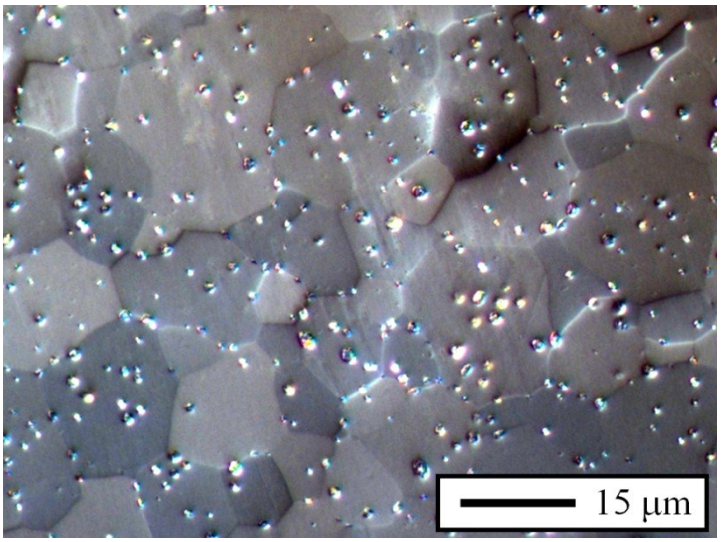

Figure. 6.3. Optical micrograph (taken from the etched, polished surface) of the ZrB_2 UHTC processed from the as-received powder. Etching was carried out by polishing with a colloidal silica suspension.

The SEM micrograph of Fig. 6.2.A also displays the presence of smaller particles (i.e., ~1 μm) that exhibit a slight compositional contrast. The EDXS analysis of these small particles shown in Fig. 6.4.A indicates that they are ZrO_2, and the XRD analysis of the compact shown in Fig. 6.4.B that this ZrO_2 crystallized in its monoclinic and tetragonal variants with the total amount of ZrO_2 representing ~8 wt.%. Thus, the combination of the SEM, EDXS, and XRD analyses reveals that the UHTC fabricated from the ball-milled ZrB_2 powder is indeed a ZrB_2-ZrO_2 composite.

The hardness and toughness measured by Vickers testing were 17.6(±0.2) GPa and 3.0(±0.1) $MPa \cdot m^{0.5}$ for the ZrB_2-ZrO_2 composite, and 16.2 (±0.2) GPa and 1.9 (±0.1) $MPa \cdot m^{0.5}$ for the reference ZrB_2 monolith. The increased toughness of the ZrB_2-ZrO_2 composite compared to the reference

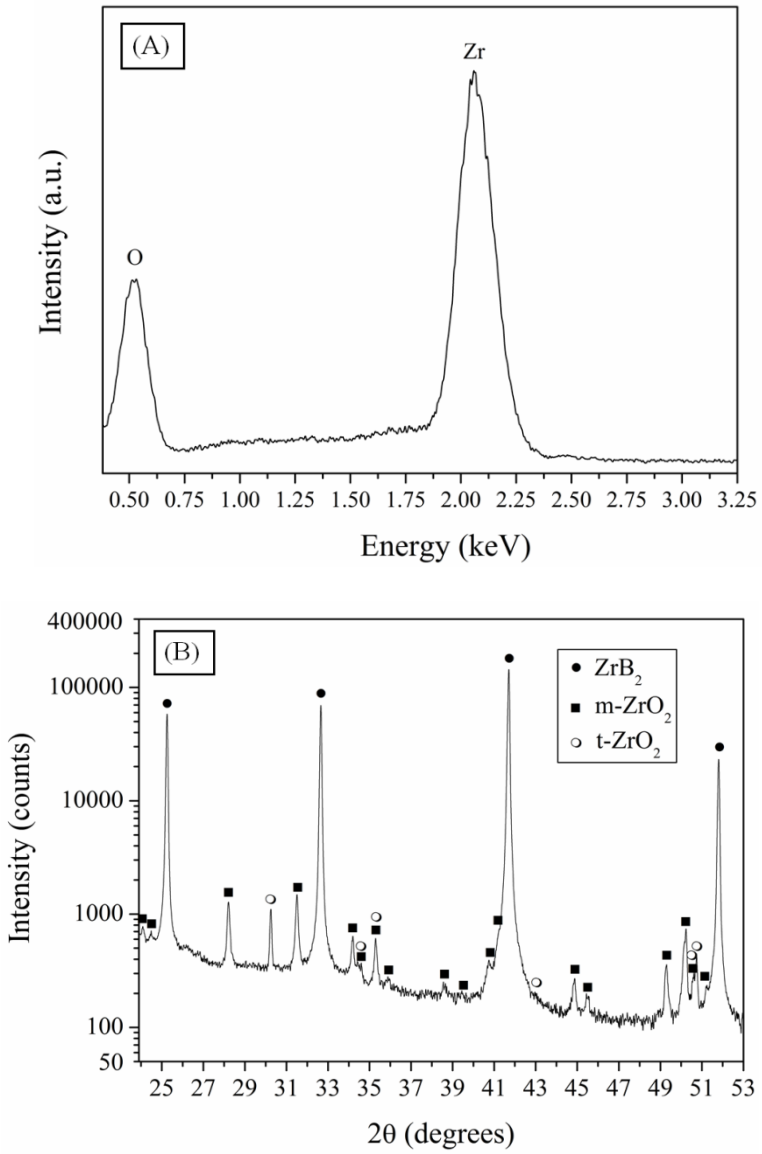

Figure. 6.4. (A) Energy-dispersive X-ray spectra taken in spot mode on the small particles in the BSE-SEM micrograph of Fig. 6.1.A. (B) X-ray diffraction pattern of the ZrB_2 UHTC processed from the 180-min ball-milled powder; the phase identification is included, and the logarithmic Y-scale is to facilitate the appreciation of the monoclinic (m) and tetragonal (t) ZrO_2 peaks.

ZrB_2 monolith, which has a grain size more than twice as large, highlights the fundamental role of ZrO_2 in enhancing the ZrB_2 toughness via crack bridging and its transformation toughening in accordance with previous observations [22–24]. Furthermore, despite ZrO_2 being softer than ZrB_2, the ZrB_2-ZrO_2 composite is harder than the reference ZrB_2 monolith, in part because the former is fully dense whereas the latter is only ~96% dense (see Figs. 6.2.B and 6.3).

The remarkable characteristic of the ZrB_2-ZrO_2 UHTC composite prepared in this study is its microstructure. Previously, ZrB_2-ZrO_2 composites have been fabricated from the typical mechanical mixture of ZrB_2 and ZrO_2 powders [22-24]. As such, they have the classical duplex microstructure, with micrometre-sized ZrO_2 grains dispersed between coarser ZrB_2 grains. In the present case, however, the ZrB_2-ZrO_2 composite has a different microstructure, with submicrometre ZrO_2 particles located in the grain boundaries and multigrain junctions of fine ZrB_2 grains. Importantly, the fabrication route of this ZrB_2-ZrO_2 composite does not require the explicit incorporation of ZrO_2 particles, since they form in situ during the SPS of the ZrB_2 powder previously subjected to high-energy ball-milling in air, which notably simplifies the processing route. Thus, the ZrO_2 phase arises from the surface oxidation itself of ZrB_2 that occurs during the high-energy ball-milling in air [36], which, as will be demonstrated below, is actually the key to obtaining that particular microstructure. In addition to ZrO_2, B_2O_3 is also formed during this oxidation of ZrB_2 [36] but is not retained during the SPS at high temperatures, as will be discussed below.

To elucidate the formation mechanism of this ZrB_2-ZrO_2 UHTC composite, a series of model experiments was conducted in which the

electrical power of the SPS furnace was shut off at lower temperatures. Owing to the rapid cooling to room temperature of the SPS furnace, the micrographs taken from these samples can be considered "frozen" pictures of the microstructure of the ZrB_2-ZrO_2 composite during the heating ramp, thus providing a good method for monitoring its microstructural development. Fig. 6.5.A is a representative SEM micrograph of the sample obtained at 1700 °C, showing many grain boundaries without apparent evidence of other phases. However, the extensive SEM observations revealed the existence of another two types of grain boundaries/faces. One of these can be observed in Fig. 6.5.A, but is shown in more details in the SEM micrograph of Fig. 6.5.B. It consists of a phase with viscous appearance located at grain boundaries and multigrain joints, which was identified by EDXS as being ZrO_2. The other type of grain-boundary structure is shown in the SEM micrograph of Fig. 6.5.C. It can be seen that some grain faces exhibit what appears to be a dendritic-like structure. This type of structure was rarely found in the sample

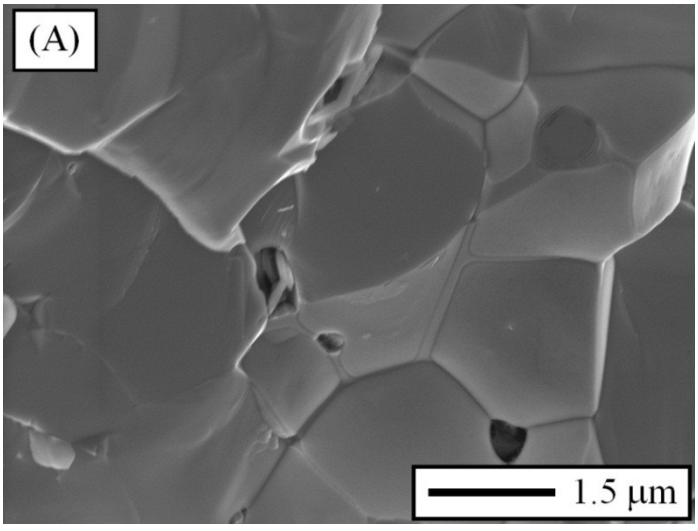

Figure. 6.5. In the next page.

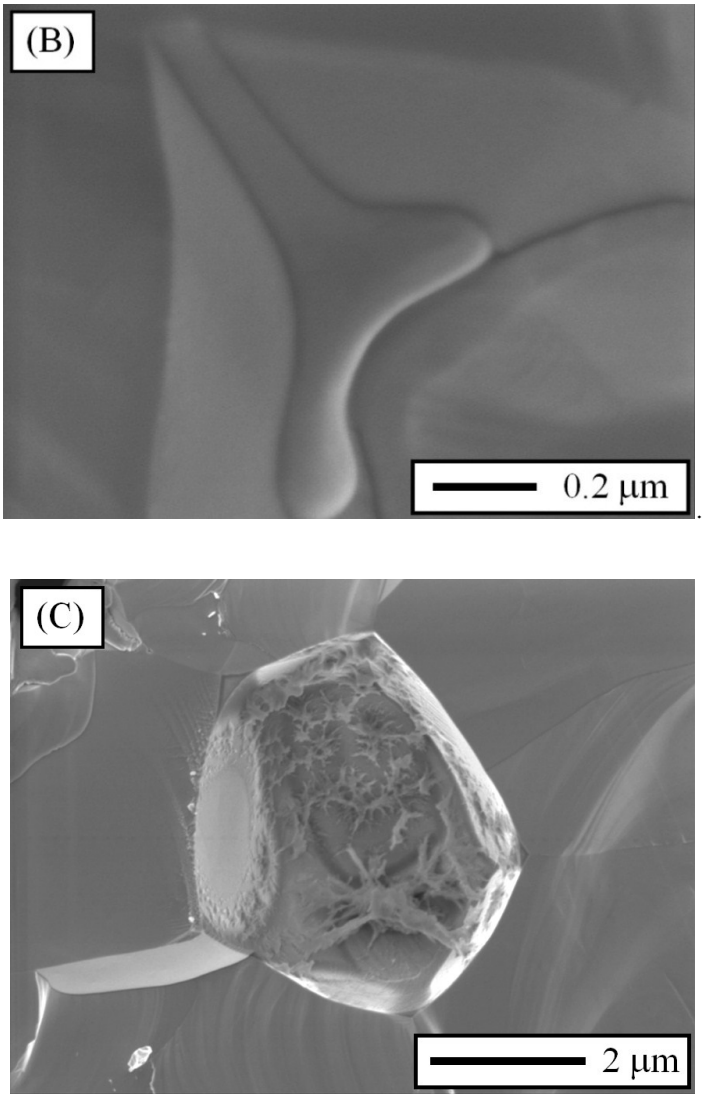

Figure. 6.5. SEM micrographs (taken with secondary electrons from the fracture surface) of the different types of grain boundaries/faces observed during the heating ramp at 1700 °C for the ZrB_2 UHTC processed from the powder with 180 min of high-energy ball-milling in air, showing (A) many ZrB_2-ZrB_2 contacts without any presence of other phases, (B) a viscous phase at grain boundaries and multigrain joints, and (C) a dendritic-like structure on some grain faces.

obtained at 1700 °C, and was not observed during the SEM examination of the ZrB_2-ZrO_2 composite sintered at 1900 °C, indicating that it is transient. The probable explanation is that this dendritic-like structure originated due to the fast condensation (fast cooling rates greater than 600 °C·min^{-1} are achieved when the electrical power in the SPS is shut off) of the gaseous B_2O_3 formed during the heating ramp. Sublimation of B_2O_3 in the temperature range 1400-1650 °C is a well-know phenomenon in ZrB_2 UHTCs, and is indeed the method used to remove the B_2O_3 impurities present on the surface of the ZrB_2 particles with a view to facilitating sintering [37,38]. Since according to the densification curve shown in Fig. 6.6 the relative density in the

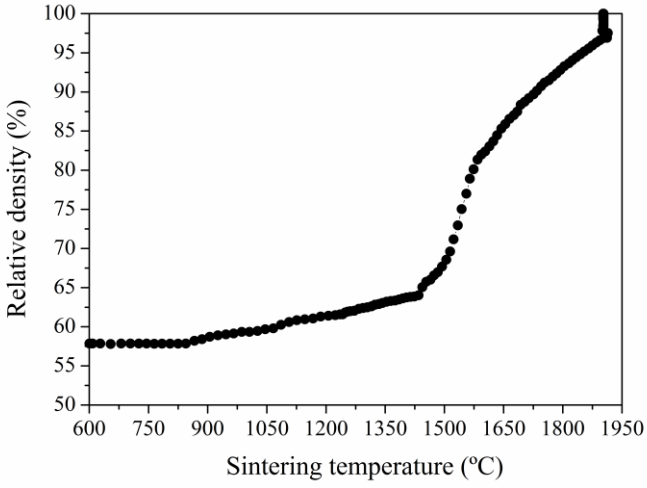

Figure. 6.6. SPS-densification curve as a function of temperature for the ZrB_2 powder with 180 min of high-energy ball-milling in air.

temperature range 1400-1650 °C varies in the interval ~65-88%, and the SPS test was done in dynamic vacuum (~6 Pa), most of the B_2O_3 gas generated was

eliminated during the heating ramp, whereas the still-enclosed B_2O_3 gas at 1700 °C condensed dendritically when exposed to the ultra-fast cooling to room temperature. However, the B_2O_3 gas is completely eliminated at higher sintering temperatures, as proved by the absence of the dendritic-like structure in the ZrB_2-ZrO_2 UHTC composite sintered at 1900 °C, and the observation that the vacuum level temporary dropped from ~6 to 8 Pa and then recovered its level of ~6 Pa.

With these SEM/EDXS observations, it is very reasonable to think that the formation of the ZrB_2-ZrO_2 UHTC composites occurs as follows. Initially during the high-energy ball-milling in air, the ZrB_2 particles oxidize superficially, developing an amorphous oxide film of ZrO_2 and B_2O_3 [36]. Subsequently, during the heating ramp under dynamic vacuum atmosphere, the B_2O_3 impurities are removed by sublimation, while the ZrO_2 film creeps due to the applied pressure (75 MPa in the present case). Note that the creep literature has shown sufficient experimental evidence that ZrO_2, and in particular the monoclinic and tetragonal phases, can creep appreciably below 1400 °C at 50 MPa [39-43], which are temperatures and pressures lower than used here. At the intermediate stage of sintering when, according to Coble's model [44], an interconnected cylindrical pore structure exists along the grain edges as schematized by the idealized geometry of Fig. 6.7.A, the viscous ZrO_2 is then squeezed out from grain faces under compression and accumulates within the pore structure network. Later during the heating ramp already in the final stage of sintering when, again according to Coble's model [44], the open pore structure collapses and evolves towards discrete spherical pores located at grain corners as sketched in Fig. 6.7.B, the viscous ZrO_2 flows to the multigrain joints. Upon fast cooling to room temperature, the viscous ZrO_2

entrapped at multigrain joints crystallizes there in part as monoclinic ZrO_2 because this is the stable polymorph in the absence of doping. However, the high-temperature tetragonal polymorph is also present at room temperature, possibly stabilized by some 3^+ solute ions (i.e., B^{3+}) as has been observed before for Al^{3+} [45], or simply retained by the ultra-fast cooling in the SPS.

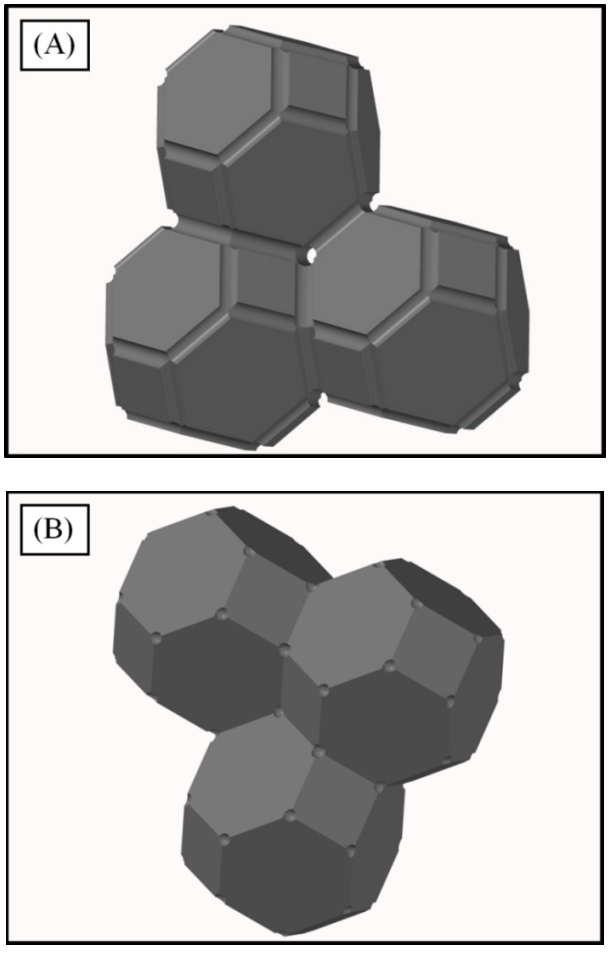

Figure. 6.7. Schematic representation of three grains and the pore structure during the (A) intermediate and (B) final stages of sintering, according to Coble's model. The actual microstructure consists of many of these units packed to fill the space.

The proposed mechanism is consistent with the densification curve measured experimentally. As shown in Fig. 6.6, there is a clear increase in densification between ~1450 °C and 1600 °C, as would be expected from the formation and flow of a viscous phase. However, there is no full densification by pore filling due to the insufficient volume fraction of viscous ZrO_2 formed (~8 wt.% equivalent to ~8 vol.% because the densities of ZrB_2 and ZrO_2 are very similar). Furthermore, the subsequent densification does not proceed via liquid-phase sintering, but by solid-state sintering, because ZrO_2 does not form a continuous liquid matrix that embeds the ZrB_2 grains.

With the mechanism of microstructural development proposed above, the formation of these ZrB_2-ZrO_2 UHTC composites might not be exclusive of the ZrB_2 powder subjected to high-energy ball-milling for 180 min in air, but may also occur for any ZrB_2 powder as long as it oxidizes sufficiently during ball-milling. This assumption has been explored here using two ZrB_2 powders subjected to high-energy ball-milling in air for 10 and 30 min, respectively, and then spark-plasma sintered under the same conditions as the powder with 180 min of high-energy ball-milling. The average crystallite size in these two ZrB_2 powders is 70 and 25 nm [34], respectively, and their oxygen content is 3.4 and 4.1 wt.%, respectively. These results and the previous ones for the powder with 180 min of ball milling indicate that the oxygen content increases and the crystallite size decreases with increasing high-energy ball-milling time. As can be observed in Fig. 6.8, the SEM micrographs confirm the formation of ZrB_2-ZrO_2 UHTC composites in both cases, with different ZrB_2 grain sizes (~10 and 7 μm, respectively) and ZrO_2 contents (~3 and 7 wt.%, respectively). It can thus be inferred from the microstructural

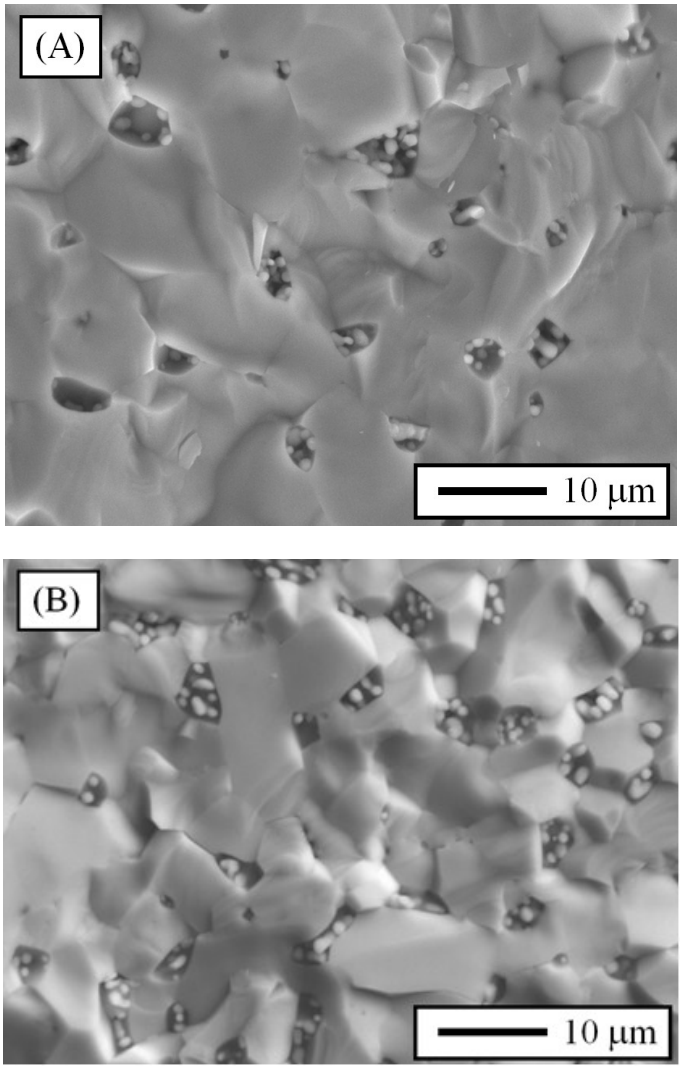

Figure. 6.8. SEM micrographs (taken with backscattered electrons from the fracture surface) of the ZrB_2 UHTCs processed from the powders subjected to high-energy ball-milling in air for (A) 10 min, and (B) 30 min.

observations (Figs. 6.2.A, 6.8.A and 6.8.B) that the longer the high-energy ball-milling time of the ZrB_2 powder, the smaller the ZrB_2 grain size and the

higher the ZrO_2 content in the ZrB_2-ZrO_2 UHTC composites. Consequently, it is reasonable to think that in principle it would be possible to control the microstructure of these ZrB_2-ZrO_2 UHTC composites to some extent by the judicious selection of the high-energy ball-milling conditions, in particular of the time and atmosphere (oxygen partial pressure, stationary or dynamic, etc.), together with the optimization of the sintering protocol. Note that the spontaneous passivation of ZrB_2 in contact with air at room-temperature after high-energy ball-milling is not a concern due to the controlled oxidation of ZrB_2 during milling.

In view of the above results, it is worthwhile to examine briefly the reasons why this type of ZrB_2-ZrO_2 UHTC composite has not been observed before. This is most likely due to a combination of two factors. Firstly, the commercially available ZrB_2 powders are typically refined by wet attrition milling under inert atmosphere, and thus the resulting powders have lower oxygen contents and, in addition, are submicrometric. Secondly, the attrition-milled powders are commonly densified either by pressureless sintering or hot-pressing with the help of additives (such as C, B_4C, and WC) that act as reductants removing the surface oxides, because these oxides favour coarsening over densification [1]. In the present study, by contrast, the densification by SPS of the ZrB_2 nano-powders prepared by high-energy ball-milling in air was done without the explicit incorporation of reductants. Note however that the high-energy ball-milling might introduce WC, although in an amount insufficient to reduce all the ZrO_2 formed during the milling in air, and in addition, the reduction reaction is not favoured by the SPS conditions used (rapid sintering for only 3 min at 1900 °C). Having discovered a route to fabricate ZrB_2-ZrO_2 UHTC composites with original

microstructures, the next step will be to reproduce this process more controllably and to extend it to other ZrB_2-oxide composites. It is proposed that this could be done by impregnating the ZrB_2 powder particles obtained by high-energy ball-milling under controlled conditions with oxide solutions prepared by the sol-gel method, and then spark-plasma sintering or hot-pressing these oxide-coated ZrB_2 powders, since the use of pressure is vital for the oxide phase to creep. If successful, this would appear to be a versatile method for processing a wide variety of ZrB_2 UHTC composites containing the desired proportion of evenly distributed oxide particles of uniform size, customized chemistry, and defined crystal structure located at grain boundaries and multigrain joints, and consequently could be used to provide the ZrB_2 UHTCs with tailored properties. This, however, remains to be explored experimentally.

6.4. SUMMARY

The in situ formation is reported of a fine-grained ZrB_2 ultra-high-temperature ceramic (UHTC) containing evenly distributed ZrO_2 of uniform size located at triple joints and grain boundaries of the ZrB_2 grains, discovered during the spark-plasma sintering of ZrB_2 powders subjected to high-energy ball-milling in air. It is found that this type of microstructure forms because the oxide film of ZrO_2, developed on the surface of the ZrB_2 particles during the high-energy ball-milling in air, creeps towards the ZrB_2 multigrain joints under the application of pressure during sintering, and then crystallizes there during the fast cooling down to room-temperature. Together with the mechanism by which these dense ZrB_2-ZrO_2 UHTC composites form, it is also

shown that they are simultaneously harder and much tougher than their ZrB_2 monolith counterpart.

6.5. REFERENCES

1) Fahrenholtz, W. G., Hilmas, G. E., Talmy, I. G. and Zaykoski, J. A. Refractory diborides of zirconium and hafnium. J Am Ceram Soc. 2007;90:1347-64.

2) Guo, S-Q. Densification of ZrB_2-based composites and their mechanical and physical properties: a review. J Eur Ceram Soc. 2009;29:995-1011.

3) Zhang, S. C., Hilmas, G. E. and Fahrenholtz, W. G. Mechanical properties of sintered ZrB_2-SiC ceramics. J Eur Ceram Soc. 2011;31:893-901.

4) Wang, Y., Liang, J., Han, W. and Zhang, X. Mechanical properties and thermal shock behavior of hot-pressed ZrB_2-SiC-AlN composites. J Alloys Compd. 2009;475:762-5.

5) Zhang, X., Li, X., Han, J., Han, W. and Hong, C. Effects of Y_2O_3 on microstructure and mechanical properties of ZrB_2-SiC ceramics. J Alloys Compd. 2008;465:506-11.

6) Liang, J., Wang, Y., Fang, G. and Han, J. Research on thermal shock resistance of ZrB_2-SiC-AlN ceramics using an indentation-quench method. J Alloys Compd.2010;493:695-8.

7) Guo, W. M., Yang, Z. G. and Zhang, G. J. Comparison of ZrB_2-SiC ceramics with Yb_2O_3 additive prepared by hot pressing and spark plasma sintering. Int J Refract Met. 2011;29:452-5.

8) Sun, X., Han, W., Hu, P., Wang, Z. and Zhang, X. Microstructure and mechanical properties of ZrB_2-Nb composite. Int J Refract Met Hard Mater. 2010;28:472-4.

9) Wang, H. L., Chen, D. L., Wang, C. A., Zhang, R. and Fang, D. N. Preparation and characterization of high-toughness ZrB_2/Mo composites by hot-pressing process. Int J Refract Met Hard Mater. 2009;27:1024-6.

10) Yang, F., Zhang, X., Han, J. and Du, S. Processing and mechanical properties of short carbon fibers toughened zirconium diboride-based ceramics. Mater Des. 2008;29:1817-20.

11) Yang, F., Zhang, X., Han, J. and Du, S. Characterization of hot-pressed short carbon fiber reinforced ZrB_2-SiC ultra-high temperature ceramic composites. J Alloys Compd. 2009;472:395-9.

12) Tian, W. B., Kan, Y. M., Zhang, G. J. and Wang, P. L. Effect of carbon nanotubes on the properties of ZrB_2-SiC ceramics. Mater Sci Eng A. 2008; 487:568-73.

13) Zhou, S. B., Wang, Z. and Zhang, W. Effect of graphite flake orientation on microstructure and mechanical properties of ZrB_2-SiC-graphite composite. J Alloys Compd. 2009;485:181-5.

14) Zhi, W., Qiang, Q., Zhanjun, W. and Guodong, S. Effect of oxidation at 1100 °C on the strength of ZrB_2-SiC-graphite ceramics. J Alloys Compd. 2011;509:6871-5.

15) Wang, Z., Wang, S., Zhang, X., Hu, P., Han, W. and Hong, C. Effect of graphite flake on microstructure as well as mechanical properties and thermal shock resistance of ZrB_2-SiC matrix ultrahigh temperature ceramics. J Alloys Compd. 2009;484:390-4.

16) Zhou, P., Hu, P., Zhang, X. and Han, W. Laminated ZrB_2-SiC ceramic with improved strength and toughness. Scripta Mater. 2011;64:276-9.

17) Silvestroni, L., Sciti, D., Melandri, C. and Guicciardi, S. Toughened ZrB_2-based ceramics through SiC whisker or SiC chopped fiber additions. J Eur Ceram Soc. 2010;30:2155-64.

18) Guicciardi, S., Silvestroni, L., Nygren, M. and Sciti, D. Microstructure and toughening mechanisms in spark plasma-sintered ZrB_2 ceramics reinforced by SiC whiskers or SiC-chopped fibers. J Am Ceram Soc. 2010;93:2384-91.

19) Zhang, P., Hu, P., Zhang, X., Han, J. and Meng, S. Processing and characterization of ZrB_2-SiC_w ultra-high temperature ceramics. J Alloys Compd. 2009;472:358-62.

20) Zhang, X., Xu, L., Du, S., Liu, C., Han, J. and Han, W. Spark plasma sintering and hot pressing of ZrB_2-SiC_w ultra-high temperature ceramics. J Alloys Compd. 2008;466:241-5.

21) Wang, M., Wang, C. A. and Zhang, X. Effects of SiC platelet and $ZrSi_2$ additive on sintering and mechanical properties of ZrB_2-based ceramics by hot-pressing. Mater Des. 2012;34:293-7.

22) Li, W., Zhang, X., Hong, C., Han, W. and Han, J. Preparation, microstructure and mechanical properties of ZrB_2-ZrO_2 ceramics. J Eur Ceram Soc. 2009;29:779-86.

23) Li, W., Zhang, Y., Zhang, X., Hong, C. and Han, W. Thermal shock behavior of ZrB_2-SiC ultra-high temperature ceramics with addition of zirconia. J Alloys Compd. 2009;478:386-91.

24) Zhu, T., Li, W., Zhang, X., Hu, P., Hong, C. and Weng, L. Damage tolerance and R-curve behavior of ZrB_2-ZrO_2 composites. Mater Sci Eng A. 2009;516:297-301.

25) Jia, L., Xinghong, Z., Zhib, W., Wenboa, H. and Hua, J. Microstructure and mechanical properties of hot-pressed ZrB_2-SiC-ZrO_{2f} ceramics with different sintering temperatures. Mater Des. 2012;34:853-6.

26) Jia, L., Xinghong, Z., Zhi, W. and Wenbo, H. Microstructure and mechanical properties of ZrB_2-SiC-ZrO_{2f} ceramic. Scripta Mater. 2011;64:872-5.

27) Zhang, X., Zhou, P., Hu, P. and Han, W. Toughening of laminated ZrB_2-SiC ceramics with residual surface compression. J Eur Ceram Soc. 2011;31:2415-23.

28) Wei, C., Zhanga, X., Hua, P., Hana, W. and Tianb, G. The fabrication and mechanical properties of bionic laminated ZrB_2-SiC/BN ceramic prepared by tape casting and hot pressing. Scripta Mater. 2011;65:791-4.

29) Lü, Z., Jiang, D., Zhang, J., Lin, Q. and Huang, Z. ZrB_2-SiC laminated ceramic composites. J Eur Ceram Soc. 2012;32:1435-9.

30) Zimmermann, J. W., Hilmas, G. E. and Fahrenholtz, W. G. Themal shock resistance and fracture behavior of ZrB_2-based fibrous monolith ceramics. J Am Ceram Soc. 2009;92:161-6.

31) Munir Z. A., Quach, D. V. and Ohyanagi, M. Electric current activation of sintering: a review of the pulsed electric current sintering process. J Am Ceram Soc. 2011;94:1-19.

32) Galán, C. A., Ortiz, A. L., Guiberteau, F. and Shaw, L. L. Crystallite size refinement of ZrB_2 by high-energy ball milling. J Am Ceram Soc. 2009;92:3114-7.

33) Galán, C. A., Ortiz, A. L., Guiberteau, F. and Shaw, L. L. High-energy ball milling of ZrB_2 in the presence of graphite. J Am Ceram Soc. 2010;93:3072-5.

34) Zamora, V., Ortiz, A. L., Guiberteau, F., Shaw, L. L. and Nygren, M. On the crystallite size refinement of ZrB_2 by high-energy ball-milling in the presence of SiC. J Eur Ceram Soc. 2011;31:2407-14.

35) Lawn, B. R. Fracture of brittle solids. Cambridge University Press, Cambridge, United Kingdom, 1993.

36) Ortiz, A. L., Zamora, V. and Rodríguez-Rojas, F. A study on the Oxidation of ZrB_2 powders during high-energy ball-milling in air. Ceram Int. 2012;38:2857-63.

37) Zhang, S. C., Hilmas, G. E. and Fahrenholtz, W. G. Pressureless densification of zirconium diboride with boron carbide additions. J Am Ceram Soc. 2006;89:1544-50.

38) Fahrenholtz, W. G., Hilmas, G. E., Zhang, S.C. and Zhu, S., Pressureless sintering of zirconium diboride: particle size and additive effects, J Am Ceram Soc. 2008;91:1398-404.

39) Zapata-Solvas, E., Gómez-García, D., García-Gañán, C. and Domínguez-Rodríguez, A. High temperature creep behaviour of 4 mol% yttria tetragonal zirconia polycrystals (4-YTZP) with grain sizes between 0.38 and 1.15 μm. J Eur Ceram Soc. 2007;27:3325-9.

40) Jiménez-Melendo, M., Domínguez-Rodríguez, A. and Bravo-León, A. Superplastic flow of fine-grained yttria-stabilized zirconia polycrystals constitutive equation and deformation mechanisms. J Am Ceram Soc. 1998;81:2761-76.

41) Lorenzo-Martín, C., Gómez-García, D., Gallardo-López, A., Domínguez-Rodríguez, A. and Chaim, R. An explanation of the high temperature creep of yttria tetragonal zirconia nanocrystals. Scripta Mater. 2004;50:1151-5.

42) Jiménez-Melendo, M. and Domínguez-Rodríguez, A. High temperature mechanical characteristics of superplastic yttria-stabilized zirconia. An examination of the flow process. Acta Mater. 2000;48:3201-10.

43) Roddy, M. J., Cannon, W. R., Skandan, G. and Hahn, H. Creep behavior of nanocrystalline monoclinic ZrO_2. J Eur Ceram Soc. 2002;22:2657-62.

44) Coble, R. L. Sintering crystalline solids. I. Intermediate and final state diffusion models. J Appl Phys. 1961;32:787-92.

45) Vasiliev, A. L., Padture, N. P. and Ma, X. Nanostructured coatings of metastable ceramics: Part I, the ZrO_2-Al_2O_3 binary System. Acta Mater. 2006;54:4913-20.

"The important thing in science is not so much to obtain new facts as to discover new ways of thinking about them"

Sir Willian Lawrence Bragg (1890-1971)

Chapter VII: Enhancement of the Spark-Plasma Sintering Kinetics of ZrB_2-SiC Powder Mixtures Subjected to High-Energy Co-Ball-Milling

7.1. MOTIVATION

ZrB_2 with SiC additions is one of the few materials to have captured the attention of the ultra-high-temperature ceramic (UHTC) community. This is because these composites combine efficiently attractive ultra-refractory properties and relatively low density of the ZrB_2 matrices with the beneficial role of the SiC improving the oxidation resistance and the mechanical properties [1,2]. Not surprisingly, the last few years have seen a flurry of research activity aimed at studying the ZrB_2-SiC composites in detail [1-36], much of which has centred on their conventional pressureless sintering and hot-pressing at lower temperatures. More recently, the development of spark-plasma sintering (SPS) has also motivated a growing

interest in their rapid lower-temperature densification[a] with finer microstructures [2,37-47], with the anticipation of further improvement of the mechanical properties.

Another field of particular current attention within the UHTC community is the study of the dependence of the sinterability of these materials on the processing method used for the starting powders, because it is now known that the features of the starting powders strongly condition the driving force for their densification [1,2,17,45,48,49]. The ZrB_2-SiC powder mixtures for SPS are no exception to this general rule, as has been demonstrated recently in two comparative densification studies, one performed on powders in the as-received condition and after attrition milling (these latter with and without intentional oxidation and carbon addition [45]), and the other on powders subjected to conventional ball-milling or attrition milling, with and without subsequent heat-treatment for oxide elimination [47]. Clearly, more fundamental studies of this kind are required to extend our knowledge of the effects of the powder processing methods on the densification by SPS of the ZrB_2-SiC composites.

One of the most recent advances in the powder processing area of UHTCs is high-energy ball-milling under dry conditions, which is able to refine ZrB_2 powders and ZrB_2-SiC powder mixtures to the nanoscale[b] [50-52]. However, systematic investigation of its effects on the sinterability of ZrB_2-

[a] This is beyond the possibilities of both conventional pressureless sintering and hot-pressing, since they are based on the use of radiant heating elements. Furthermore, microwave sintering has fundamental problems in the case of ZrB_2 -a very good conductor that does not readily couple with microwaves- and the viability of flash sintering ZrB_2 has yet to be demonstrated.
[b] This cannot be done by conventional ball-milling or wet attrition milling because neither of them generate the high compressive stresses required to fracture ultra-fine particles [53,54].

based powders is very limited, the exception being two studies devoted to investigating the SPS kinetics [55] and densification [56] of ZrB_2 powders as a function of milling time. Consequently, as a continuation to these previous studies, the present work was undertaken to investigate for the first time the improvement of the SPS kinetics of the typical ZrB_2-SiC powder mixtures (i.e., 5-30 vol.% of SiC) induced by high-energy co-ball milling. The study is therefore focused exclusively on processing aspects, without investigation of materials properties.

7.2. EXPERIMENTAL PROCEDURE

7.2.1. Processing

The preparation protocol of the three sets of ZrB_2-SiC powder mixtures with eight different degrees of high-energy co-ball-milling[c] each which were used in the present study has been described in detail elsewhere [52]. Consequently, we shall describe here only the key steps. Briefly, commercially-available ZrB_2 (Grade B, H.C. Starck, Germany; ~2 μm) and SiC (UF-15, H.C. Starck, Germany; ~0.55 μm) powders combined in relative concentrations of 95-5, 82.5-17.5, and 70-30 vol.%, respectively, were co-milled in air for different times (i.e., 1, 3, 5, 10, 30, 60, and 180 min) in a shaker mill (Spex 8000D, Spex CertiPrep, United States) operated at 1060 back-and-forth cycles per minute. The milling was carried out in a cylindrical hardened-steel container with WC balls (6.7 mm in diameter;

[c] Hereafter, the term high-energy (co)-ball-milling will be abbreviated simply as (co)-milling for the sake of readability.

Union Process Inc., United States) under a ball-to-powder weight ratio of 4, using the procedure described elsewhere to minimize the contamination from the milling media and container [56]. ZrB_2-SiC powder mixtures without co-milling were also prepared following the conventional method of wet homogenization plus drying of the slurries under stirring. The microstructural features of all these ZrB_2-SiC powder mixtures have been investigated in detail by X-ray diffractometry (XRD), scanning electron microscopy (SEM), and laser scattering (LS) in an earlier chapter and published elsewhere [52], where the evolution of the ZrB_2 crystal sizes and of the particle sizes with the milling time as a function of the SiC content was also discussed comprehensively. Consequently, these crystal and particle size data will be used here directly without repeating their presentation or discussion.

7.2.2. Sintering

All ZrB_2-SiC powder mixtures were individually loaded into 12-mm diameter graphite dies lined with graphite foil and surrounded by a 1-cm thick graphite blanket to minimize the heat loss, and were then spark-plasma sintered (Dr. Sinter SPS-2050, Sumitomo Coal Mining Co., Japan) in dynamic vacuum up to 1750 °C. The graphite die has a wall thickness of 9 mm, and has a hole machined in its central region of 2.5 mm depth. The temperature was first raised manually to 600 °C in 3 min, and thence onwards was measured by an optical pyrometer focused on the interior of hole of the graphite die. The heating ramp was set at 200 °C/min up to 1200 °C, and thence onwards at only 100 °C/min to capture more accurately the characteristic points of the SPS curves. The uniaxial pressure was 50 MPa up to 1200 °C, and 75 MPa thenceforth. The soaking at 1750 °C was interrupted

when the punches ceased traveling, at which moment the load was released and the electrical power was shut off.

The shrinkage curves measured experimentally with the dilatometer of the SPS furnace were then corrected for the expansion of the graphite parts to obtain the real shrinkage curve of the powders themselves, and next converted to densification curves using the relative densities of the sintered materials.

7.2.3. Microstructural Characterization

Selected UHTCs resulting from these SPS cycles were characterized using SEM, X-ray energy dispersive spectrometry (XEDS), and XRD. The SEM observations were made on fracture surfaces without additional preparation, using either a conventional microscope (S-3600N, Hitachi, Japan) or a field-emission (FE) microscope (S-4800II, Hitachi, Japan). The XEDS analyses were carried out under the FE-SEM, essentially to map the distribution of elemental Zr (line $L\alpha_1$ at 2.040 keV), Si (line $K\alpha_1$ at 1.739 keV), C (line $K\alpha_1$ at 0.266 keV), and O (line $K\alpha_1$ at 0.517 keV), although spectra in spot mode were also collected occasionally. B was not mapped because this light element is at the detection limit of the spectrometer, and in addition its $K\alpha_1$ line (at 0.172 keV) severely overlaps with the $M\alpha_1$ line of Zr (at 0.152 keV), thus introducing an unnecessary uncertainty into the measurements. W was not mapped either, because the WC contamination introduced during milling is very low (i.e., less than 0.5 vol.%) [56]. Finally, the XRD patterns were acquired in step-scanning mode (measurement range 22-62° 2θ, step width 0.028° 2θ, and count time 3 s/step) using a high-resolution laboratory diffractometer (D8 Advance, Bruker AXS, Germany) equipped with a primary monochromator that provides pure $CuK\alpha_1$ radiation (λ = 1.5406 Å) and a

linear ultra-fast detector. The phases present were identified with the aid of the PDF2 database.

Microstructural characterization study has been completed with the analysis of selected ZrB_2-SiC powder mixtures by X-ray photoemission spectroscopy (XPS) for the determination of the bonding status. The XPS spectra were recorded under ultra-high vacuum conditions (10^{-6} Pa) using a high-resolution spectrometer (K-Alpha, Thermo Scientific, UK) equipped with a monochromatic Al-Kα X-ray source (1486.6 eV), and making two types of measurement: (1) survey scans in the 0-1350 eV range at 1 eV resolution, and (2) detailed scans in the 96-110 and 177-195 eV ranges at 0.1 eV energy resolution, which cover the Si 2p, and the Zr 3d and B 1s core lines, respectively.

7.3. RESULTS

7.3.1. Kinetics of SPS

Figure 7.1 shows the SPS densification curves as functions of time for the three sets of ZrB_2-SiC powder mixtures. It can be seen that they all have the same general shape regardless of the milling time and SiC content. Specifically, first the powder always compacts linearly, then at a certain sintering time rapidly consolidates while the furnace continues heating up to 1750 °C, and lastly the compaction slows down to eventually reach the ultimate degree of densification. Nevertheless, the mere comparison of the curves in Fig. 7.1 indicates clearly that SPS kinetics benefits from the increase in SiC content and milling time.

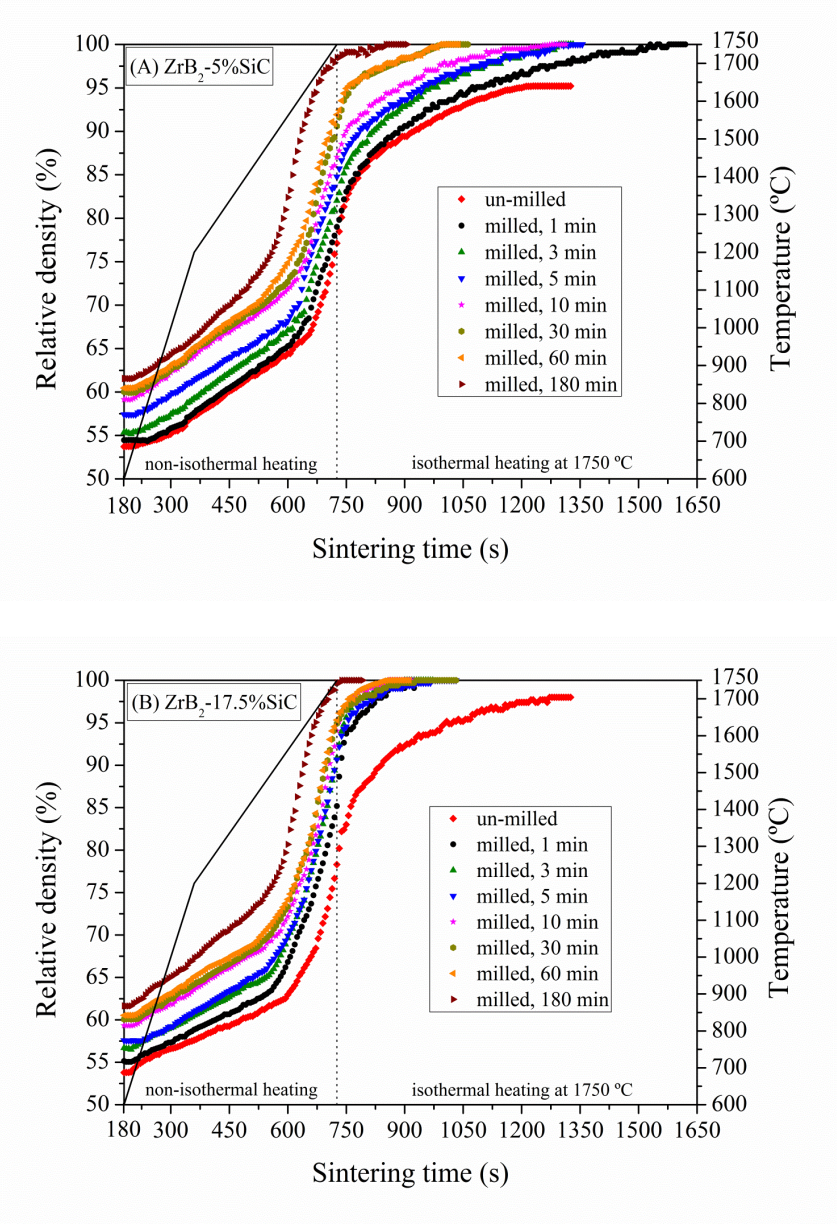

Figure. 7.1. In the next page.

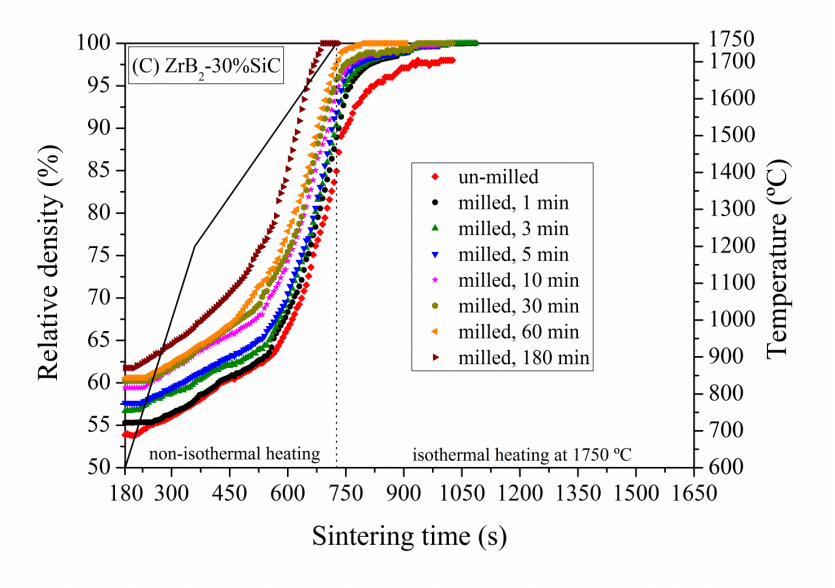

Figure. 7.1. SPS-densification curves as a function of time for the ZrB_2-SiC powder mixtures with different degrees of high-energy co-ball-milling and SiC additions of: (A) 5 vol.%, (B) 17.5 vol.%, and (C) 30 vol.%. The points are the experimental data. The solid line indicates the temperature profile used. The dashed line separates the regimes of non-isothermal and isothermal heating during the SPS cycle.

To illustrate this kinetics enhancement more rigorously, we compared various characteristic points of these densification curves with each other and, when possible, also with those determined before for the ZrB_2 without SiC [55]. There are[d]: (i) the degree of densification at the beginning of the SPS cycle (ρ_{GB}); (ii) the onset temperature of sintering (T_{OS}), which is the temperature at which the densification curve first deviates from the linear compaction stretch

[d] Temperatures will be given if the characteristic point of the densification curve falls within the regime of non-isothermal heating for the three ZrB_2-SiC powder mixtures and milling time including the un-milled case. Otherwise, sintering times will be reported.

due to the activation of diffusion; (iii) the onset temperature of the intermediate stage of sintering (T_{OIS}), which is the sintering regime in which the pore distribution transforms from open porosity to closed porosity and is typically taken to begin at ~70% relative density [57]; (iv) the peak temperature in the shrinkage-rate curves (T_{MSC}), which is the temperature at which the best combination of active densification mechanisms occurs; (v) the onset time of the final stage of sintering (t_{OFS}), which is the sintering regime in which the closed porosity is eliminated, and is normally taken to commence at ~90% relative density [52]; and finally (vi) the sintering time required to reach complete or near-complete densification (t_{FD}).

Figure 7.2 compares the evolution of ρ_{GB} with the milling time for the three ZrB_2-SiC powder mixtures and for the ZrB_2 powder [55]. There are various interesting features in this figure. Firstly, ρ_{GB} increases continuously although very little (i.e., less than 1.33%) with increasing SiC content in the ZrB_2-SiC powder mixtures from 5 to 30 vol.%. Secondly, except for the intermediate milling times (i.e., 7 to 20 min), the ZrB_2-SiC powder mixtures compacted better than the ZrB_2 powder, a phenomenon that was more pronounced for long milling times (i.e., ~3.5% at 180 min of milling). And thirdly, the three ZrB_2-SiC powder mixtures exhibit a simple trend, with ρ_{GB} increasing continuously as the milling time increases, which is substantially different from the ZrB_2 powder that first displays an increase and then a decrease. As also shown in Fig. 7.2, all these trends are determined by the particle sizes in these powders[e] because in powder compacts particle size and pore size scale together [58].

[e] The evolution of the particle sizes differs because SiC alters the rates of fracture and of cold-welding of ZrB_2 during the milling, as is explained in more detail in an earlier publication [52].

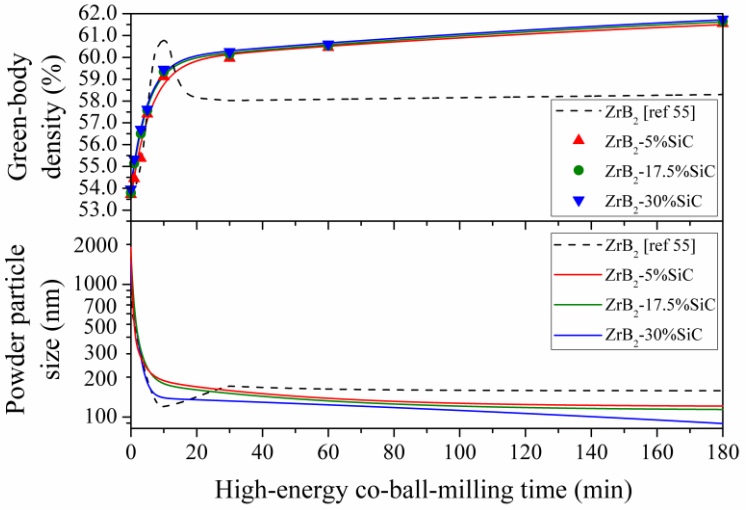

Figure. 7.2. Green-body densification for the ZrB_2-SiC powder mixtures (5, 17.5, or 30 vol.% SiC) as a function of the high-energy co-ball-milling time. The points are the experimental data, and the solid lines are merely to guide the eye. The dashed line is for ZrB_2 without SiC addition (taken from Ref. 50). Also included is the average particle size in the different ZrB_2-SiC powder mixtures and in the ZrB_2 powder as determined by laser scattering (taken from Ref. 50).

Figure. 7.3 compares the evolution of T_{OS}, T_{OIS}, T_{MSC}, t_{OFS}, and t_{FD} with the ZrB_2 crystal size achieved during the milling for the three ZrB_2-SiC powder mixtures and, when possible, also for the ZrB_2 powder [55]. It can be seen that these magnitudes all decrease progressively with decreasing ZrB_2 crystal size and also with increasing SiC content, thus confirming the deductions made from the mere observation of the densification curves in Fig. 7.1. Also very interesting is that these five plots show that, for a given SiC content, the enhancement of the SPS kinetics is always only moderate with the refinement of the ZrB_2 crystal size to the ultra-fine range, but very marked with the

refinement to the nanometre range. The dependence on the SiC content is more complex. Firstly, just 5 vol.% SiC is sufficient to appreciably speed up

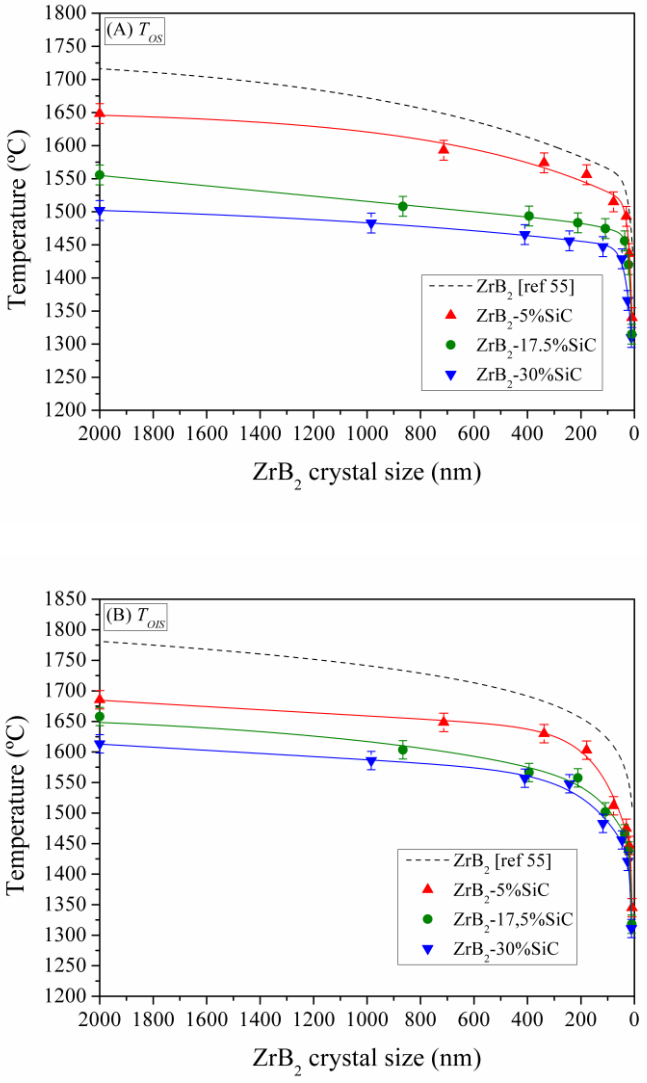

Figure. 7.3. In page 139.

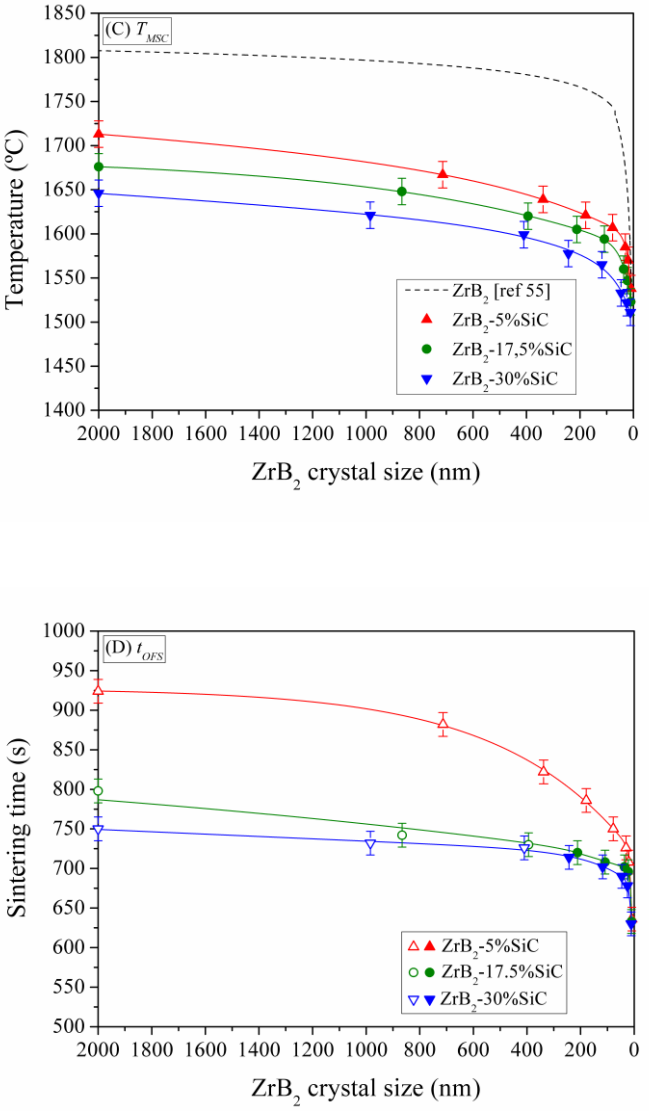

Figure. 7.3. In page 139.

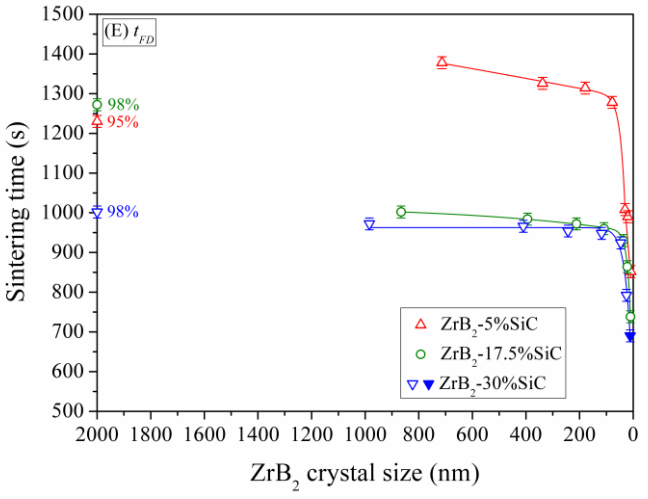

Figure. 7.3. Evolution of T_{OS}, T_{OIS}, T_{MSC}, t_{OFS}, and t_{FD} with the ZrB_2 crystal size achieved during the milling for the ZrB_2-SiC powder mixtures (5, 17.5, or 30 vol.% SiC). The points are the experimental data, and the lines are merely to guide the eye. The open symbols are values of t_{OFS} and t_{FD} determined under isothermal heating at 1750 °C, and not under non-isothermal heating as in the rest of the cases. Temperature data for the ZrB_2 powders without SiC have also been included as dashed lines (taken from Ref. 50) because the heating ramp was the same as used here; the sintering time data have not been compared with those of ZrB_2 powders because they are affected by the isothermal soakings at different temperatures (i.e., 1750 and 1900 °C with and without SiC addition, respectively).

the ZrB_2 densification, even in the un-milled condition. Secondly, the kinetics enhancement does not scale directly with the SiC content, but tends to saturate as this increases[f]. And thirdly, the beneficial role of the SiC addition decreases in relevance with the progressive refinement of the ZrB_2

[f] For example, the reductions in T_{OS}, T_{OIS}, T_{MSC}, t_{OFS}, and t_{FD} achieved with the addition of 5 and 30 vol.% SiC do not reflect any 6-fold difference between the values. Furthermore, there is greater kinetics enhancement when the SiC content was increased from 5 to 17.5 vol.% than from 17.5 to 30 vol.%, despite the SiC content increasing by 12.5 vol.% in both cases.

crystal size, especially at the nanoscale. Taken together, these observations suggest a change in the densification mechanism of the ZrB_2-SiC powder mixtures in relation to the ZrB_2 powder.

7.3.2. Microstructure after SPS

Figure. 7.4 shows representative FE-SEM micrographs of the UHTC resulting from the ZrB_2-30%SiC powder mixture milled for 180 min, which has the best SPS kinetics of all those investigated here. It can be observed in Fig. 7.4.A that this material is completely dense, as there is no evidence of residual porosity. At this temperature, ZrB_2 without SiC but with the same milling time has reached only ~90% relative density [55]. It can also be seen in Fig. 7.4.A that the microstructure consists of a mixture of various types of grains. Specifically, there are micrometre grains (~1.2 μm) with equiaxed shape, which form the primary matrix. There are also submicrometre grains

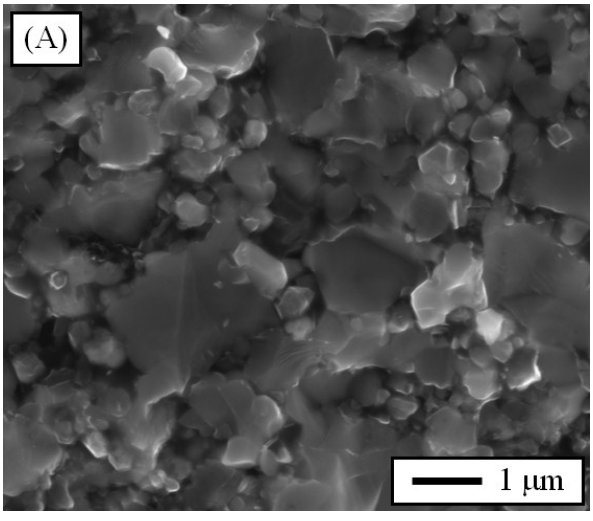

Figure. 7.4. Overleaf.

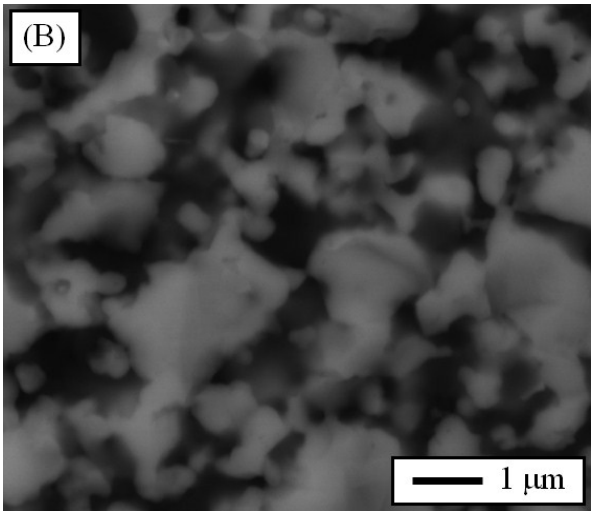

Figure. 7.4. FE-SEM micrographs of the UHTC resulting from the SPS at 1750 °C for 0 min of the ZrB_2-30%SiC powder mixture subjected to 180 min of high-energy co-ball-milling. (A) Secondary-electron image, and (B) backscattered-electron image.

(~0.5 μm) distributed uniformly in the matrix. And lastly, there are rounded grains with much smoother surfaces and ultra-fine size (~0.25 μm or less) which are segregated between the micrometre and submicrometre grains and whose morphology suggests that they originated from the solidification of a viscous phase. In the backscattered-electron FE-SEM micrograph of Fig. 7.4.B the micrometre grains and a few of the ultra-fine ones display a marked compositional contrast, indicating that they contain heavier chemical elements than the rest of the grains; the submicrometre grains and the vast majority of the ultra-fine ones exhibit a similar compositional contrast, suggestive of certain similarity between them. Furthermore, the size of the grains in Figs. 7.4.A and B reveals the occurrence of marked coarsening induced by diffusion because this powder mixture consisted of ultrafine

agglomerates (i.e., ~100 nm) of nano-particles (i.e., ~10 nm) [52]. Fig. 7.5 shows the compositional maps of elemental Zr, Si, C, and O obtained by

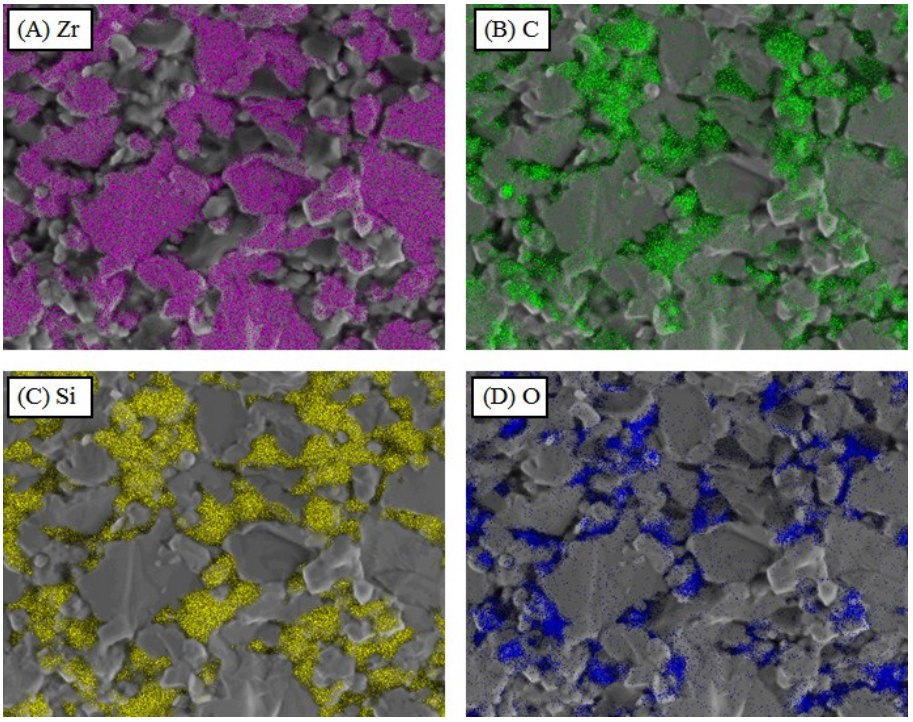

Figure. 7.5. Compositional mapping of elemental (A) zirconium, (B) carbon, (C) silicon, and (D) oxygen corresponding to the FE-SEM micrograph of Fig. 7.4. See Fig. 7.4 for the bar scale. W was not mapped, but the detection of C-rich particles without overlap with the Si and Zr signals suggests the existence of sparse WC particles.

XEDS under the FE-SEM to identify precisely the chemical nature of the different types of grains observed in Fig. 7.4. It can be concluded from the Zr distribution that the micrometre grains that form the matrix are ZrB_2. The submicrometre grains are SiC, as proved by the overlap of the Si and C signals. And lastly, the ultra-fine grains are mostly borosilicate with ZrO_2 at a much smaller proportion. Note that the ambiguity between borosilicate and

SiO_2 was broken by XEDS analyses in spot mode (not shown), which revealed a clear deviation from the SiO_2 stoichiometry. Finally, Fig. 7.6 shows the XRD analysis carried out to determine the crystalline or amorphous nature of the phases deduced from the FE-SEM/XEDS analyses. As can be observed,

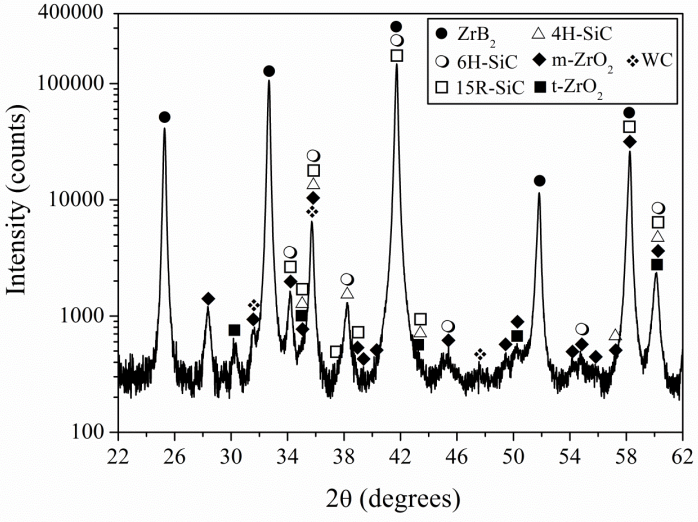

Figure. 7.6. XRD pattern of the UHTC resulting from the SPS at 1750 °C for 0 min of the ZrB_2-30%SiC powder mixture subjected to 180 min of high-energy co-ball-milling. The phase identification is included (*t* and *m* mean tetragonal and monoclinic, respectively). The logarithmic vertical scale is to facilitate the appreciation of the weak peaks (from 15R-SiC, 4H-SiC, *t*-ZrO_2, *m*-ZrO_2, and WC).

besides the expected ZrB_2 and SiC (6H, 15R, and 4H polytypes) peaks there only appear peaks from ZrO_2 (monoclinic and tetragonal polymorphs) and WC. Therefore, it can be concluded that ZrB_2, SiC, and ZrO_2 are crystalline, while the borosilicate is glassy, as also might be part of the ZrO_2 formed [59]. It is also worth noting that the ZrB_2 and SiC peaks are not shifted from their reference position, which rules out the formation of solid solutions.

Figure 7.7 shows a representative FE-SEM micrograph and the corresponding compositional maps of elemental Zr, Si, C, and O for the

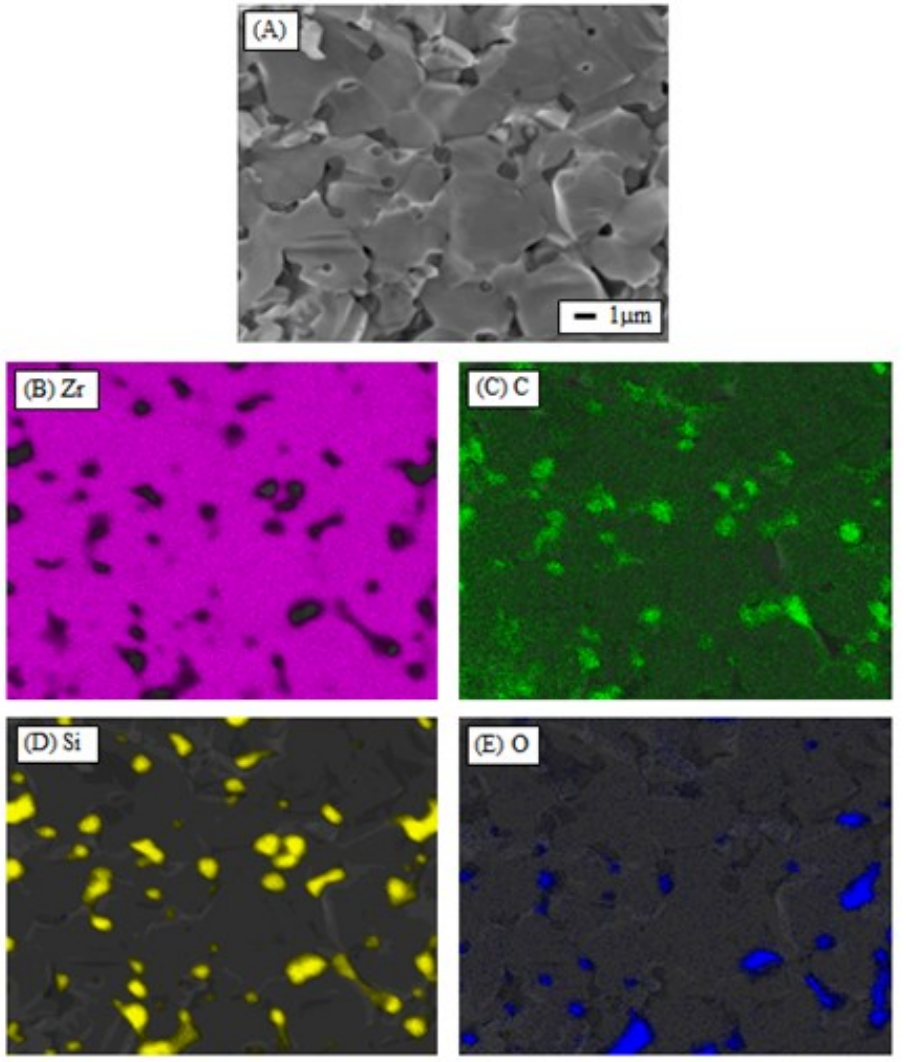

Figure. 7.7. Microstructure of the un-milled ZrB_2-30%SiC powder mixture sintered at 1750 °C for 5 min. (A) FE-SEM micrograph (secondary-electron image), and the corresponding compositional mapping of elemental (B) zirconium, (C) carbon, (D) silicon, and (E) oxygen. Average grain sizes were measured from various FE-SEM secondary-electron images using an image analysis system.

UHTC resulting from the un-milled ZrB_2-30%SiC powder mixture, and Fig. 7.8 shows its XRD pattern. The combination of FE-SEM, XEDS, and XRD analyses indicates that the microstructure is formed by fine grains of

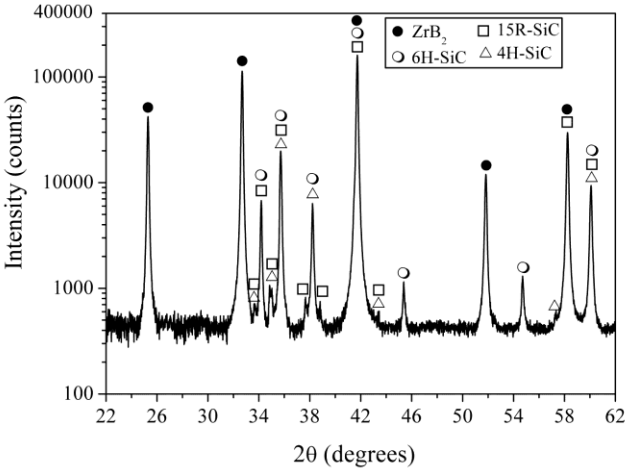

Figure. 7.8. XRD pattern of the UHTC resulting from the SPS at 1750 °C for 5 min of the un-milled ZrB_2-30%SiC powder mixture. The phase identification is included. The logarithmic vertical scale is to facilitate the appreciation of the weak peaks (from 15R-SiC, and 4H-SiC).

crystalline SiC (~0.8 μm), amorphous ZrO_2 (~0.5 μm), and amorphous borosilicate (~0.5 μm) in a matrix of large grains of crystalline ZrB_2 (~3.5 μm). Again, the grain sizes reveal diffusion-induced coarsening, but less than in the powder mixture milled for 180 min because the starting sizes were ~2 μm for ZrB_2 and ~0.55 μm for SiC. Therefore, it can be said that the microstructures in Figs. 7.4 and 7.7 are qualitatively similar, of course except for WC because one powder mixture was milled and the other not. In quantitative terms the clear difference is, however, that without milling there is less formation of

oxides (i.e., borosilicate plus ZrO_2), there occurs less grain coarsening but the microstructure is less refined, and there persists some slight residual porosity.

Figure 7.9 are typical SEM micrographs of the UHTCs resulting from the ZrB_2-5%SiC and ZrB_2-17.5%SiC powder with extreme milling times (i.e., 0 and 180 min). Comparison of these SEM images with each other and with

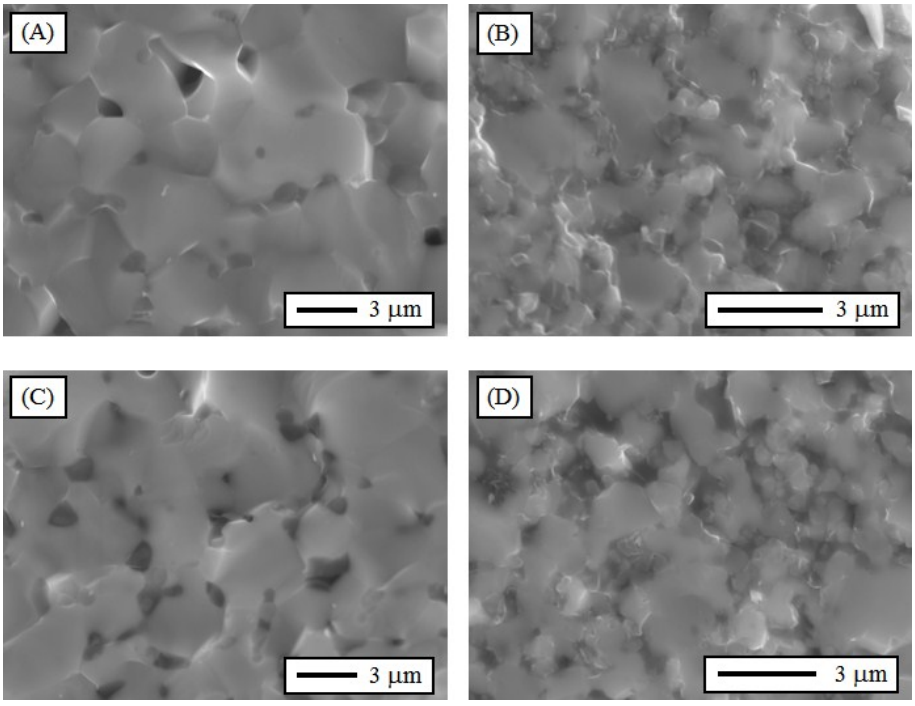

Figure. 7.9. SEM micrographs ZrB_2-5%SiC powder mixture sintered at 1750 °C (A) without and (B) with 180 min of high-energy co-ball-milling, as well as of the ZrB_2-17.5%SiC powder mixture (C) without and (D) with 180 min of high-energy co-ball-milling. The isothermal soakings lasted for 10, 3, 10, and 1 min, respectively.

those shown in Figs. 7.4 and 7.5 for the UHTC ZrB_2-30%SiC shows clearly that the increase in milling time and in SiC content promotes densification, oxide formation, and microstructural refinement despite the greater diffusion.

7.4. DISCUSSION

The results demonstrate that the SPS kinetics of the ZrB_2-SiC composites is enhanced with increasing SiC content, and also with increasing milling time. This latter is consistent with what has already been observed in ZrB_2, for which enhancement of the SPS kinetics was explained in the framework of solid-state sintering theory [57] (Herring's scaling law [60]), considering that the progressive crystal size refinement to the nanoscale induced by the milling shortens the diffusion distance of the Zr and B species while promoting the formation of a greater density of grain boundaries available as fast diffusion paths. Clearly, all this also occurs in the ZrB_2-SiC powder mixtures, for which the ZrB_2 crystals are also refined progressively with increasing milling time [57]. However, this mechanism alone does not explain the kinetics enhancement observed in ZrB_2-SiC with increasing SiC content, because SiC slowed down the kinetics of ZrB_2 crystal size refinement[g] [57]. Indeed, considering exclusively the criterion of the ZrB_2 crystal size, one would expect worsening of the SPS kinetics with increasing SiC content. Therefore, apart from the ZrB_2 crystal size refinement, there should be other(s) additional mechanism(s) of kinetics enhancement operating in the ZrB_2-SiC powder mixture whose effectiveness increases with increasing SiC content. In principle, it might be argued that SiC, driven by its lower refractoriness (melting point of 2730 °C for SiC vs 3250 °C for ZrB_2), plays a direct role in the enhancement of the SPS kinetics of ZrB_2 and thus the greater the SiC content in the ZrB_2-SiC powder mixtures the faster the SPS kinetics. However,

[g] This is due to the early nanocrystallization of SiC that promotes the consumption of collision energy in the form of frictional sliding, thus reducing the effective compressive stresses acting on the ZrB_2 crystals [52].

this explanation is not very plausible because the SiC contents used here were below the percolation threshold for SiC to form by itself a connected phase that really helps in the densification of ZrB_2 (Figs. 7.5 and 7.7), and also because a recent SPS study has demonstrated that the SiC nano-powder with 10 nm crystal size reaches only ~88% relative density at 1800 °C under 100 MPa pressure (which are a temperature and pressure higher than used here) [61].

Another possible mechanism is simply the greater green body density in the compacts of ZrB_2-SiC with increasing SiC content resulting from the lower agglomerate size [52], which ensures more intimate contact favouring diffusion between powder particles during the first moments of SPS. However, Fig. 7.2 indicates clearly that this is only a minor effect, and therefore it cannot account for the marked enhancement of the SPS kinetics although it indeed contributes to it.

Nor is Interdiffusionn between ZrB_2 and SiC the mechanism operating, the microstructural characterization of the present UHTCs has ruled out the formation of mixed compounds with Zr and Si, or of solid solutions based on ZrB_2 or SiC (Fig. 7.6).

The WC introduced during milling does not play a role either because the XEDS and XRD analyses ruled out the carbothermal reduction of ZrO_2 by WC[h]. This is reasonable because the WC contamination was less than 0.5 vol.%, and is also consistent with other recent SPS studies on ZrB_2 powders [55,56,59] and on ZrB_2-SiC powder mixtures [46] which have not observed

[h] ZrC is produced by carbothermal reduction of ZrO_2 by WC ($ZrO_2+3WC \rightarrow ZrC+3W+2CO(g)$, or $3ZrB_2+6WC+ZrO_2 \rightarrow 4ZrC+6WB+2CO(g)$), and was not observed here.

carbothermal reduction even for greater WC contamination [46]. Note that, unlike pressureless sintering and hot-pressing, in SPS these reduction reactions are neither kinetically nor thermodynamically favoured, because the reaction times are very limited and the rapid densification of the compacts prevents the CO(g) generated from escaping, thus tipping the reaction in favour of the reactants.

Therefore, the mechanism of kinetics enhancement of ZrB_2 with increasing SiC content has necessarily to be related to the formation of the oxides detected by the SEM and XRD analyses (Figs. 7.4-7.9). The presence of oxides in the microstructure of ZrB_2-SiC UHTCs is possible because ZrB_2 and SiC powders passivate spontaneously on contact with air. The surface oxidation of ZrB_2 produces ZrO_2 and B_2O_3, and that of SiC, SiO_2. To confirm this expectation, selected ZrB_2-SiC powder mixtures were analysed by XPS, which is one of the few techniques capable of detecting thin oxide films on ZrB_2 [62]. Fig. 7.10 shows the binding energy of the Si 2p, Zr 3d, and B 1s core levels in the ZrB_2-30%SiC powder mixtures with 0, 10, and 180 min of milling. Two sets of Si 2p ($2p_{3/2}$-$2p_{1/2}$ doublet with severe overlapping), Zr 3d ($3d_{5/2}$-$3d_{3/2}$ doublet), and B 1s (singlet) peaks are observed in these XPS spectra, which suggests the existence of two different bonding statuses for the Si, Zr, and B atoms. Both in the un-milled and in the two milled ZrB_2-30%SiC powder mixtures, one set of Si 2p, Zr $3d_{5/2}$, Zr $3d_{3/2}$, and B 1s peaks is located at binding energies of ~100.7, 179.2, 181.5, and 188.2 eV, respectively, values which are due to SiC [63] and ZrB_2 [64]. The other set of peaks appears at higher binding energies of ~103.2, 183.6, 186.0, and 193.2 eV, respectively, which are due to SiO_2 [65], ZrO_2 [64], and B_2O_3 [64]. It can also be seen in Fig. 7.10 that the SiO_2/SiC, B_2O_3/ZrB_2 , and ZrO_2/ZrB_2 peak intensity ratios increase with

increasing milling time. Therefore, XPS has unambiguously detected the presence of SiO_2, B_2O_3, and ZrO_2 in the un-milled and milled ZrB_2-30%SiC powder mixtures, and also shows them to be much more abundant as the milling time increases[i]. This trend, which is also valid for the ZrB_2-5%SiC and ZrB_2-17.5%SiC powder mixtures, is due to the increase in specific surface area

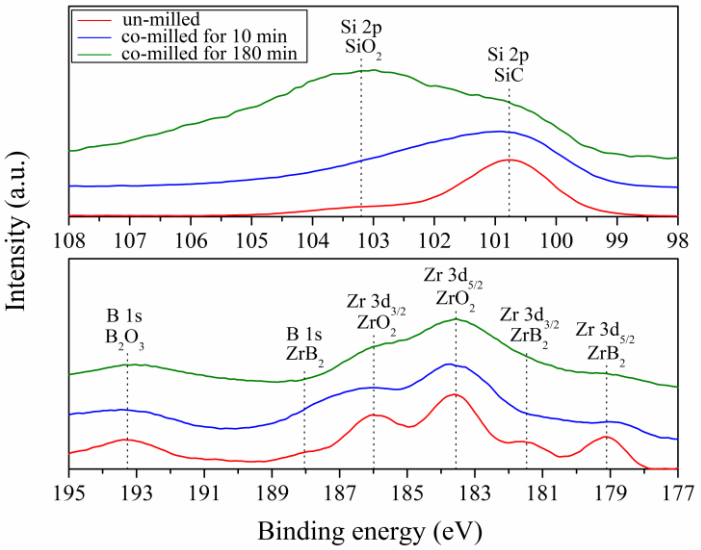

Figure. 7.10. High-resolution XPS spectra of the Si 2p (doublet Si $2p_{3/2}$-$2p_{1/2}$), Zr 3d (doublet Zr $3d_{5/2}$-$3d_{3/2}$), and B 1s (singlet) core-levels for the ZrB_2-30%SiC powder mixture without and with 10 and 180 min of high-energy co-ball-milling. The peak indexing is included. For the sake of comparison, the XPS spectra have been normalized by imposing the same maximum intensity for the Si 2p peak from SiC, and then shifted along the vertical axis to facilitate their observation. Calculations of peak ratios were made on the original data without shifting.

[i] In particular, using the core levels Si 2p for both SiO_2 and SiC, B 1s for B_2O_3, and Zr $3d_{5/2}$ for both ZrO_2 and ZrB_2, one calculates the SiO_2/SiC, B_2O_3/ZrB_2, and ZrO_2/ZrB_2 peak intensity ratios to be, respectively, 0.16, 0.85, and 2.27 for the un-milled powder, 0.68, 1.11, and 4.46 for the powder milled for 10 min, and 1.41, 1.19, and 9.97 for the powder milled for 180 min.

available for passivation induced by the crystal size refinement. Furthermore, the survey XPS spectra shown in Fig. 7.11.A indicate that the abundance of SiO_2 increases, while those of ZrO_2 and B_2O_3 decrease with increasing SiC content in the ZrB_2 powder[j]; this trend was further confirmed by detailed XPS scans[j] as is shown for convenience in Fig. 7.11.B for SiO_2 because this is the limiting compound for the formation of borosilicate.

Among the two oxides present in the microstructure, ZrO_2 plays, if any, a very secondary role in the SPS kinetics of the ZrB_2–SiC powder mixtures because it has two opposite contributions that tend to cancel out. On one hand, the passivating nano-film of ZrO_2 on the ZrB_2 particles promotes microstructural coarsening, which is detrimental for the densification [66,67]. But on the other hand it also creeps under pressure towards the multigrain joints thus filling pores [59], which is beneficial for the densification. Thus, the combination of opposite effects leaves the borosilicate as the primary responsible for the enhancement of the SPS kinetics of the ZrB_2 with increasing SiC content.

It is therefore reasonable to think that the underlying mechanism of kinetics enhancement is the following. During the SPS, part of the existing B_2O_3 on the ZrB_2 particles, which normally is highly volatile and escapes from the sample, reacts with the existing SiO_2 on the surface of the neighbouring SiC particles, producing a borosilicate glass that stays in the sample doubly benefiting the SPS kinetics.

[j] Note that the intensity of the Si 2p signal in the survey XPS spectra of the powders with 0, 5, 17.5, and 30 vol.% SiC is 0, 4000, 11000, and 22300 counts, that of the Zr 3d signal is 166500, 144500, 109300, and 105700 counts, and that of the B 1s signal is 83800, 78000, 61850, and 60900 counts. Similarly, the intensity of the Si 2p signal from SiO_2 in the detailed XPS spectra is 0, 426, 1250, and 2440 counts.

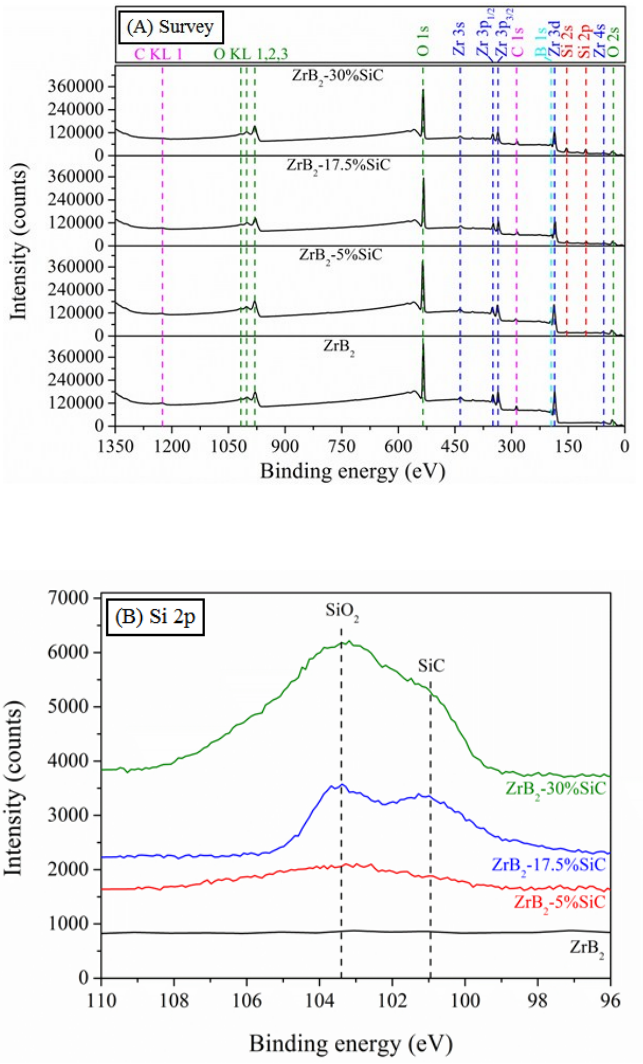

Figure. 7.11. (A) Survey XPS spectra of the three ZrB_2-SiC powder mixtures (5, 17.5, or 30 vol.%SiC) and of the ZrB_2 powder, all subjected to 180 min of high-energy ball-milling. (B) The corresponding high-resolution XPS spectra of the Si 2p (doublet Si $2p_{3/2}$-$2p_{1/2}$) core-level. The peak indexing is included in both figures. No normalization condition was imposed in any of the cases. In (B), the XPS spectra have been shifted along the vertical axis to facilitate their observation. Measurements of signal intensities were made on the original data without shifting.

Firstly, part of the borosilicate forms amorphous nano-films at the interphase grain boundaries, speeding up the interparticle diffusion and therefore enhancing the densification kinetics. Note that the existence of these nano-films has been confirmed elsewhere by high-resolution transmission electron microscopy [17]. And secondly, under the application of high pressures the excess of borosilicate is segregated by viscous flow into the multi-grain joints, thus contributing to the densification by pore filling. This is consistent with independent FE-SEM observations on a ZrB_2-25%SiC UHTCs also fabricated by SPS [47].

The proposed mechanism explains well the entire set of experimental observations. Consider first the effect of the SiC content in the ZrB_2-SiC powder mixtures. Clearly, increasing the proportion of SiC particles, the carriers of SiO_2, implies greater formation of borosilicate, and therefore faster SPS kinetics. However, the kinetics enhancement does not scale directly with the SiC content because it is not dictated merely by the pore filling by borosilicate since various diffusion mechanisms are also active. Furthermore, two other reasons are that neither is the pore filling limited by the amount of borosilicate once the pores have collapsed sufficiently, and that the viscosity of borosilicate glasses increases as they become richer in SiO_2 [68]. Consider now the effect of increasing the milling time. Clearly, the greater specific surface area available for passivation resulting from the crystal size refinement entails greater formation of borosilicate, thus inducing, together with the crystal size refinement itself, a faster SPS kinetics. However, the contribution from borosilicate starts to become less relevant with the progressive refinement of the ZrB_2 crystal size to the nanoscale, because in this size regime the sintering kinetics is dominated by the great density of grain boundaries available as fast

diffusion paths for the Zr and B species, together with the diminished diffusion lengths. Finally, the faster diffusion induced by the combination of the greater abundance of borosilicate and the smaller crystal sizes also explains the greater coarsening observed with increasing milling time and SiC content, but finer microstructures are obtained since the soaking times required to reach complete densification are shorter.

In closing, it seems worthwhile to discuss potential implications and limitations deriving from the present work. It has been demonstrated recently that the T_{MSC} data provide the referent for the optimization of the SPS isothermal cycles of the ZrB_2 UHTCs. Therefore, thanks to the borosilicate formation, in principle it would be possible to reduce the SPS temperatures of the ZrB_2-SiC powder mixtures to the limits shown in Fig. 7.3.D if the isothermal soaking is appropriate. Such lower-temperature sintering is one of the long sought objectives in the field of UHTCs. However, because the presence of the low melting-point borosilicate segregated at grain boundaries and multi-grain joints will adversely affect the high-temperature mechanical properties [33], the concentration of SiC in the ZrB_2 powder and the milling conditions have to be chosen appropriately for a correct balance between lower-temperature densification and mechanical properties. This warrants further investigation not only on the lower-temperature SPS of these ZrB_2-SiC powder mixtures, but also on the mechanical properties (and oxidation resistance) of the resulting UHTCs.

7.5. SUMMARY

The spark-plasma sintering (SPS) kinetics of ZrB_2-SiC powder mixtures was investigated as a function of the degree of high-energy co-ball-milling and of the SiC content (5, 17.5, or 30 vol.%). As in ZrB_2 without SiC, it was found that the crystal size refinement induced by the continued milling progressively enhances the SPS kinetics of ZrB_2-SiC, again only moderately if the refinement is to the ultra-fine range, but very marked if the refinement is to the nanoscale. It was also found that the SiC addition further enhances the SPS kinetics of ZrB_2, although the improvement did not scale directly with the SiC content, and became less relevant with the refinement of the ZrB_2 crystal sizes to the nanoscale. The improved kinetics induced by the SiC addition was identified as being due to the formation of amorphous borosilicate from the oxide passivating layers on the ZrB_2 and SiC particles. This not only speeds up the interparticle diffusion, but also it is segregated under the application of pressure into the multi-grain joints, filling pores. The enhanced kinetics induced by the progressive milling is due to the continuous reduction of the diffusion distances and to the development of a greater density of grain boundaries available as faster diffusion paths, together with the greater formation of amorphous borosilicate. Implications of interest for the ultra-high-temperature ceramics community are discussed.

7.6. REFERENCES

1) Fahrenholtz, W. G., Hilmas, G. E., Talmy, I. G. and Zaykoski J. A. Refractory diborides of zirconium and hafnium. J Am Ceram Soc. 2007; 90:1347-64.

2) Guo, S-Q. Densification of ZrB_2-based composites and their mechanical and physical properties: a review. J Eur Ceram Soc. 2009; 29:995-1011.

3) Tripp, W. C., Davis, H. H. and Graham, H. C. Effect of an SiC addition on the oxidation of ZrB_2. J Electrochem Soc. 1973;52:612-6.

4) Opeka, M., Talmy, I. G., Wuchina, E. J. and Zaykoski, J. A. and Causey, S.J. Mechanical, thermal, and oxidation properties of refractory hafnium and zirconium compounds. J Eur Ceram Soc. 1999;19:2405-14.

5) Zhang, G. J., Deng, Z. Y., Kondo, N., Yang, J. F. and Ohji, T. Reactive hot pressing of ZrB_2-SiC composites. J Am Ceram Soc. 2000;83:2330-2.

6) Opila, E. J. and Halbig, M. C. Oxidation of ZrB_2-SiC. Ceram Eng Sci Proc. 2001;22:221-8.

7) Levine, S. R., Opila, E. J., Halbig, M. C., Kiser, J. D., Singh, M. and Salem J. A. Evaluation of ultra-high temperature ceramics for aeropropulsion use. J Eur Ceram Soc. 2002;22:2757-67.

8) Monteverde, F., Guicciardi, S. and Bellosi, A. Advances in microstructure and mechanical properties of zirconium diboride based ceramics. Mater Sci Eng A. 2003;346:310-9.

9) Chamberlain, A. L., Fahrenholtz, W. G., Hilmas, G. E. and Ellerby, D. T. High-strength zirconium diboride-based ceramics. J Am Ceram Soc. 2004; 87:1170-2.

10) Monteverde, F. and Bellosi, A. Development and characterization of metaldiboride-based composites toughened with ultra-fine SiC particulates. Solid State Sci. 2005;7:622-30.

11) Chamberlain, A. L., Fahrenholtz, W. G. and Hilmas, G. E. Oxidation of ZrB_2-SiC ceramics under atmospheric and reentry conditions. Refract Appl Trans. 2005;1:1-8.

12) Monteverde, F. Beneficial effects of an ultra-fine α-SiC incorporation on the sinterability and mechanical properties of ZrB_2. Appl Phys A: Mater Sci and Process. 2006;82:329-37.

13) Rezaie, A. R., Fahrenholtz, W. G. and Hilmas, G. E. Oxidation of zirconium diboride-silicon carbide at 1500 °C a low partial pressure of oxygen. J Am Ceram Soc. 2006;89:3240-5.

14) Rezaie, A., Fahrenholtz, W. G. and Hilmas, G. E. Effect of hot pressing time and temperature on the microstructure and mechanical properties of ZrB_2-SiC. J Mater Sci. 2007;42:2735-44.

15) Rezaie, A., Fahrenholtz, W. G. and Hilmas G. E. Evolution of structure during the oxidation of zirconium diboride–silicon carbide in air up to 1500°C. J Eur Ceram Soc. 2007;27:2495–501.

16) Hwang, S. S., Vasiliev, A. L. and Padture, N. P. Improved processing and oxidation-resistance of ZrB_2 ultra-high temperature ceramics containing SiC nanodispersoids. Mat Sci Eng A. 2007;464:216-24.

17) Peng, F. and Speyer, R. F. Oxidation resistance of fully dense ZrB_2 with SiC, TaB_2, and $TaSi_2$ additives. J Am Ceram Soc. 2008;91:1489-94.

18) Inna, G., Talmy, J. A., Zaykoski, M. M. and Opeka, M. High-temperature chemistry and oxidation of ZrB_2 ceramics containing SiC, Si_3N_4, Ta_5Si_3, and $TaSi_2$. J Am Ceram Soc. 2008;91:2250-7.

19) Zhang, S. C., Hilmas G. E. and Fahrenholtz, W. G. Pressureless sintering of ZrB_2-SiC ceramics. J Am Ceram Soc. 2008;91:26-32.

20) Zimmermann, J. W., Hilmas, G. E. and Fahrenholtz, W. G. Thermal shock resistance of ZrB_2 and ZrB_2-30% SiC. Mater Chem Phys. 2008;112:140-5.

21) Han, J., Hu, P., Zhang, X., Meng, S. and Han, W. Oxidation-resistant ZrB_2-SiC composites at 2200 °C. Compos Sci Technol. 2008;68:799-806.

22) Zimmermann, J. W., Hilmas, G. E., Fahrenholtz, W. G., Dinwiddie, R. B., Porter, W. D. and Wang, H. Thermophysical properties of ZrB_2 and ZrB_2-SiC ceramics. J Am Ceram Soc. 2008;91:1405-11.

23) Karlsdottir, S. N. and Halloran, J. W. Oxidation of ZrB_2-SiC: influence of SiC content on solid and liquid oxide phase formation. J Am Ceram Soc. 2009;92:481-6.

24) Guo, W. M., Zhou, X. J., Zhang, G. J., Kan, Y. M., Li, Y. G. and Wang, P. L. Effect of Si and Zr additions on oxidation resistance of hot-pressed ZrB_2-SiC composites with polycarbosilane as a precursor at 1500 °C. J Alloys Compd. 2009;471:153-6.

25) Guo, W-M., Vleugels, J., Zhang, G-J., Wang, P-L. and Van der Biest, O. Effects of Re_2O_3 (Re =La, Nd, Y and Yb) addition in hot-pressed ZrB_2-SiC ceramics. J Eur Ceram Soc. 2009;29:3063-8.

26) Hu, P., Guolin, W. and Wang, Z. Oxidation mechanism and resistance of ZrB_2-SiC composites. Corros Sci. 2009;51:2724-32.

27) Zimmermann, J. W., Hilmas, G. E. and Fahrenholtz, W. G. Thermal shock resistance and fracture behavior of ZrB_2-based fibrous monolith ceramics. J Am Ceram Soc. 2009;92:161-6.

28) Alfano, D., Scatteia, L., Monteverde, F., Bêche, E. and Balat-Pichelin, M. Microstructural characterization of ZrB_2-SiC based UHTC tested in the MESOX plasma facility. J Eur Ceram Soc. 2010; 30:2345-55.

29) Silvestroni, L., Sciti, D., Melandri, C. and Guicciardi, S. Toughened ZrB_2-based ceramics through SiC whisker or SiC chopped fiber additions. J Eur Ceram Soc. 2010;30:2155-64.

30) Watts, J., Hilmas, G. and Fahrenholtz W. G. Mechanical characterization of ZrB_2-SiC composites with varying SiC particle sizes. J Am Ceram Soc. 2011;94:4410-8.

31) Sciti, D., Guicciardi, S. and Silvestroni, L. SiC chopped fibers reinforced ZrB_2: Effect of the sintering aid. Scripta Mater. 2011;64:769-72.

32) Sciti, D., Silvestroni, L., Medri, V. and Guicciardi, S. Pressureless sintered in situ toughened ZrB_2-SiC platelets ceramics. J Eur Ceram Soc. 2011;31:2145-53.

33) Zou, J., Zhang, G-J., Hu, C-F., Nishimura, T., Sakka, Y., Vleugels, J. and Van der Biest, O. Strong ZrB_2-SiC-WC ceramics at 1600 °C. J Am Ceram Soc. 2012;95:874-8.

34) Sciti, D., Savino, R. and Silvestroni, L. Aerothermal behaviour of a SiC fibre-reinforced ZrB_2 sharp component in supersonic regime. J Eur Ceram Soc. 2012;32:1837-45.

35) Sciti, D. and Silvestroni, L. Processing, sintering and oxidation behavior of SiC fibers reinforced ZrB_2 composites. J Eur Ceram Soc. 2012;32:1933-40.

36) Zou, J., Zhang, G-J., Hu, C-F., Nishimura, T., Sakka, Y., Tanaka, H., Vleugels, J. and Van der Biest, O. High-temperature bending strength, internal friction and stiffness of ZrB_2-20vol.%SiC ceramics. J Eur Ceram Soc. 2012;32:2519-27.

37) Zhao, Y., Wang, L., Zhang, G., Jiang, W. and Chen, L. Preparation and microstructure of a ZrB_2-SiC composite fabricated by the spark plasma sintering-reactive synthesis (SPS-RS) method. J Am Ceram Soc. 2007;90:4040-2.

38) Wang, H., Wang, C-A., Yao, X. and Fang, D. Processing and mechanical properties of zirconium diboride-based ceramics prepared by spark plasma sintering. J Am Ceram Soc. 2007;90:1992-7.

39) Wu, W-W., Zhang, G-J., Kan, Y-M., Wang, P-L., Vanmeensel, K., Vleugels, J. and Van der Biest, O. Synthesis and microstructural features of ZrB_2-SiC-based composites by reactive spark plasma sintering and reactive hot pressing. Scripta Mater. 2007;57:317-20.

40) Zhang, X., Xu, L., Du, S., Liu, C., Han, J. and Han, W. Spark plasma sintering and hot pressing of ZrB_2-SiC_W ultra-high temperature ceramics. J Alloys Compd. 2008;466:241-5.

41) Akin, I., Hotta, M., Sahin, F. C., Yucel, O., Goller, G. and Goto, T. Microstructure and densification of ZrB_2-SiC composites prepared by spark plasma sintering. J Eur Ceram Soc. (2009);29:2379-85.

42) Carney, C. M., Mogilvesky, P. and Parthasarathy, T. A. Oxidation behavior of zirconium diboride silicon carbide produced by the spark plasma sintering method. J Am Ceram Soc. 2009;92:2046-52.

43) Guo, W-M., Vleugels, J., Zhang, G-J., Wang, P-L. and Van der Biest, O. Effect of heating rate of densification, microstructure and strength of spark plasma sintered ZrB_2-based ceramics. Scripta Mater. 2010;62:802-5.

44) Ran, S., Van der Biest, O. and Vleugels, J. ZrB_2-SiC composites prepared by reactive pulsed electric current sintering. J Eur Ceram Soc. 2010;30:2633-42.

45) Thompson, M., Fahrenholtz, W. G. and Hilmas, G. Effect of starting particle size and oxygen content on densification of ZrB_2. J Am Ceram Soc. 2011;94:429–35.

46) Guo, W-M., Yang Z-G., Vleugels, J. and Zhang, G-J. Effect of pressure loading cycle on spark plasma sintered ZrB_2-SiC-Yb_2O_3 ceramics. Ceram Int. 2012;38:5293-7.

47) Walker, L. S., Pinc, W. R. and Corral, E. L. Powder processing effects on the rapid low-temperature densification of ZrB_2. J Am Ceram Soc. 2012;95:194-203.

48) Zhu, S., Fahrenholtz, W. G., Hilmas, G. E. and Zhang, S. C. Pressureless sintering of carbon-coated zirconium diboride powders. Mater Sci Eng A. 2007;459:167-71.

49) Fahrenholtz, W. G., Hilmas, G. E., Zhang, S. C. and Zhu, S. Pressureless sintering of zirconium diboride: particle size and additive effects. J Am Ceram Soc. 2008;91:1398-404.

50) Galán, C. A., Ortiz, A. L., Guiberteau, F. and Shaw, L. L. Crystallite size refinement of ZrB_2 by high-energy ball milling. J Am Ceram Soc. 2009;92:3114-7.

51) Galán, C. A., Ortiz, A. L., Guiberteau, F. and Shaw, L. L. High-energy ball milling of ZrB_2 in the presence of graphite. J Am Ceram Soc. 2010;93:3072-5.

52) Zamora, V., Ortiz, A. L., Guiberteau, F., Shaw, L. L. and Nygren, M. On the crystallite size refinement of ZrB_2 by high-energy ball-milling in the presence of SiC. J Eur Ceram Soc. 2011;31:2407-14.

53) Soni, P. R. Mechanical alloying. Fundamental and applications. Cambridge International Science Publishing. Cambridge, UK; 2001.

54) Suryanarayana, C. Mechanical alloying and milling. Prog Mater Sci. 2001;46:1-184.

55) Zamora, V., Ortiz, A. L., Guiberteau, F. and Nygren, M. Crystal-size dependence of the spark-plasma-sintering kinetics of ZrB_2 ultra-high-temperature ceramics. J Eur Ceram Soc. 2012;32:271-6.

56) Zamora, V., Ortiz, A. L., Guiberteau, F. and Nygren, M. Spark-plasma sintering of ZrB_2 ultra-high-temperature ceramics at lower temperature via nanoscale crystal refinement. J Eur Ceram Soc. 2012;32:2529-36.

57) German, R. M. Sintering Theory and Practice. Wiley, New York; 1996.

58) German, R. M. Powder metallurgy science. Princeton, NJ: Metal Powder Industries Federation; 1994.

59) Zamora, V., Ortiz, A. L., Guiberteau, F. and Nygren M. In-situ formation of ZrB_2-ZrO_2 ultra-high-temperature composites from high-energy ball-milled ZrB_2 powders. J Alloys Compd. 2012;518:38-43.

60) Herring, C. Effect of change of scale on sintering phenomena. J Appl Phys. 1950;21:301-3.

61) Lara, A., Ortiz, A. L., Muñoz, A. and Domínguez-Rodríguez, A. Densification of additive-free polycrystalline β-SiC by spark-plasma sintering. Ceram Int. 2012;38:45-53.

62) Ortiz, A. L., Zamora, V. and Rodríguez-Rojas, F. A study on the oxidation of ZrB_2 powders during high-energy ball-milling in air. Ceram Int. 2012;38:2857-63.

63) Galuska, A. A., Uht, J. C., Marquez, N. Reactive and nonreactive ion mixing of Ti films on carbon substrates. J Vac Sci Technol A. 1988;6:110-22.

64) Huerta, L., Durán, A., Falconi, R., Flores, M. and Escamilla, R. Comparative study of the core level photoemission of the ZrB_2 and ZrB_{12}. Physica C. 2010; 470:456-60.

65) Wagner, C. D., Passoja, D. E., Hillery, H. F., Kinisky, T. G., Six, H. A., Jansen, W. T. and Taylor, J. A. Auger and photoelectron line energy relationships in aluminium-oxygen and silicon oxygen compounds. J Vac Sci Technol. 1982;21:933-44.

66) Chamberlain, A. L., Fahrenholtz, W. G. and Hilmas, G. E. Pressureless sintering of zirconium diboride. J Am Ceram Soc. 2006;89:450-6.

67) Zhang, S. C., Hilmas, G. E. and Fahrenholtz, W. G. Pressureless densification of zirconium diboride with boron carbide additions. J Am Ceram Soc. 2006;89:1544-50.

68) Bruckner, R. and Fernández, J. F. Physikalisch-chemische untersuchungen in system B_2O_3-SiO_2. Glastech Ber. 1966;39:283-93.

"I am turned into a sort of machine for observing facts and grinding out conclusions"

Charles Robert Darwin (1809-1882)

Chapter VIII: Conclusions

The high-energy ball-milling and spark-plasma sintering behaviours of ZrB_2-based UHTCs has been extensively studied in this Ph.D. work. Among the most relevant conclusions of this study, it is worth highlighting the following ones:

- With respect to the effect of SiC addition on the high-energy ball-milling behaviour of ZrB_2:

  1. The presence of SiC during high-energy ball-milling does not change the comminution mechanism of ZrB_2, i.e., repeated brittle fracture followed by cold-welding. With this mechanism, the powder particles formed during high-energy ball-milling are first sub-micrometre single-crystals, and then become ultrafine agglomerates consisting of single-crystal nano-particles.
  2. The SiC addition, however, does slow down the refinement kinetics of the ZrB_2 crystals and decreases cold-welding, promoting the formation of finer agglomerates. The former is attributed to the early nano-crystallization of SiC during high-energy ball-milling and the

collision energy consumption by frictional sliding of SiC nano-particles, leading to lower compressive stresses on ZrB_2 particles. The latter is due to the lower chemical affinity between SiC and ZrB_2 than ZrB_2 themselves and the generation of many SiC nano-particles at the early stage of high-energy ball-milling.

3. The SiC addition does not affect the ultimate crystal size of ZrB_2 because this is mainly dictated by the fracture strength and by the compressive stress at the collision site.

4. The addition of a harder material with a lower fracture toughness (e.g., SiC) than the softer material (e.g., ZrB_2) can slow down the refinement of crystallite sizes. This discovery offers a new mechanism to control the crystallite size during high-energy ball-milling in the future.

5. High-energy co-ball-milling offers an exciting opportunity to attain ultrafine nano-agglomerates consisting of ZrB_2 and SiC nano-particles intimately dispersed at a nanoscale, factors which would be expected to facilitate the sintering of the ZrB_2-SiC composites. This, together with the simplification of the powder preparation routine, suggests that high-energy co-ball-milling may have an important role to play in the processing of ZrB_2-SiC UHTCs.

❖ With respect to the oxidation of ZrB_2 powders during high-energy ball-milling in air:

1. The direct measurement of the oxygen content by the IGF method revealed that the powders subjected to high-energy ball-milling in air

are twice as rich in oxygen as those subjected to the more conventional attrition milling.

2. The XRD analyzes, including detailed Rietveld refinements, showed that the captured oxygen does not form solid-solutions but amorphous oxides.

3. The density measurement by helium pycnometry confirmed the formation of such oxides, and was entirely consistent with the phase composition determined by IGF and XRD.

4. The XPS analyzes indicated that these amorphous oxides are ZrO_2 and B_2O_3, something that could not be determined by the FTIR or Raman spectroscopy, and that they locate preferentially on the surface of the powder particles, in perfect agreement with the direct TEM observations.

❖ With respect to the crystal-size dependence of the spark-plasma sintering kinetics of ZrB_2 UHTCs:

1. The crystal size refinement enhances the SPS kinetics of ZrB_2 powders, reducing the onset temperatures of sintering and of the intermediate and final sintering regimes, as well as promoting a greater maximum shrinkage rate at lower temperatures.

2. The enhancement in the kinetic performance of the powder is moderate with the reduction of the crystal size within the submicrometre range, but relevant with the refinement down to the nanoscale.

3. The activation energy for grain-boundary diffusion in ZrB_2 is 2070 kJ/mol, which is very high and accounts for the unsinterability of the coarse ZrB_2 powders without sintering additives at moderate temperatures.

4. High-energy ball-milling can provide the ZrB_2 starting powders with the kinetics performance not achievable today by conventional attrition milling. It may therefore have an important role to play in the lower-temperature sintering of ZrB_2 UHTCs.

❖ With respect to the spark-plasma sintering of ZrB_2 UHTCs at lower-temperature via nanoscale crystal refinement:

1. The lower-temperature limit for the spark-plasma sintering densification of ZrB_2 decreases continuously with decreasing crystal size in the starting powder.

2. Under otherwise identical spark-plasma sintering conditions (i.e., 75 MPa pressure, and 100 °C/min heating ramp), nanoscale ZrB_2 has been densified at 1625 °C, well below the 2000 °C required for the typical micrometre and submicrometre powders to reach only 96% densification and the corresponding 1875 °C for the ultra-fine powder. Thus, crystal size refinement to the low nanoscale constitutes one of the long hoped-for break-through solutions to the fundamental problem of the poor sinterability of ZrB_2.

3. Nanoscale ZrB_2 can be densified at temperatures as low as 1450 °C favoured by the presence of B_2O_3 liquid phase, but this

low-temperature sintering with non-transient B_2O_3 is not useful for ultra-high-temperature applications.

4. The complete densification of ZrB_2 UHTCs requires the use of sintering cycles that promote the total elimination, via evaporation, of the B_2O_3 impurities. This is especially relevant in the case of spark-plasma sintering because the rapid collapse of the open pore structure facilitates the trapping of the B_2O_3 gas generated within the closed pores.
5. Nanoscale crystal refinement promotes the production of fine-grained microstructures, derived from the combination of the smaller crystal sizes in the starting powders and the lower sintering temperatures required for densification.
6. High-energy ball-milling can provide ZrB_2 with the superior sinterability which is not otherwise achievable today by the standard comminution method of wet attrition milling.

❖ With respect to the in situ formation of dense ZrB_2-ZrO_2 UHTC composites discovered during the spark-plasma sintering of ZrB_2 powders subjected to high-energy ball-milling in air:

1. The mechanism has been identified in situ formation of dense ZrB_2-ZrO_2 UHTC composites, discovered during the spark-plasma sintering of ZrB2 powders subjected to high-energy ball-milling in air.
2. These composites exhibit original microstructures consisting of submicrometre ZrO_2 particles located in the grain boundaries and multigrain junctions of fine ZrB_2 grains, and form because the oxide

film of ZrO_2 developed on the surface of the ZrB_2 particles during the high-energy ball-milling creeps towards the ZrB_2 multigrain joints under the application of pressure during sintering.

3. Besides identifying the formation mechanism, it has also been shown that these engineered ZrB_2-ZrO_2 UHTC composites are denser and have finer grains than the ZrB_2 monolith fabricated under the same conditions of spark-plasma sintering, and in addition, they are also simultaneously harder and much tougher.

❖ With respect to the enhancement of the spark-plasma sintering kinetics of ZrB_2-SiC powder mixtures subjected to high-energy co-ball-milling:

1. The SiC addition increasingly enhances the spark-plasma sintering kinetics of ZrB_2 by promoting the formation of amorphous borosilicate that speeds up the interparticle diffusion and is segregated under pressure into the multi-grain joints, thus filling pores. Borosilicate forms due to the reaction during the spark-plasma sintering of the SiO_2 and B_2O_3 existing as passivating layers on the surface of SiC and ZrB_2 particles, respectively.

2. The crystal size refinement induced by the high-energy co-milling increasingly enhances the spark-plasma sintering kinetics of the ZrB_2-SiC powder mixtures, which is due to the combination of the reduction of the diffusion distances, the development of a greater density of grain boundaries available as faster diffusion paths, and the greater formation of amorphous borosilicate.

3. The kinetics enhancement promoted by the SiC addition does not scale directly with its content, and becomes less relevant with decreasing ZrB_2 crystal size to the nanoscale. The former finding reflects that the spark-plasma sintering kinetics is not limited by the segregation of borosilicate into the pores (which is also a complex phenomenon not conditioned only by the amount of borosilicate) but involves a combination of various mechanisms, and the latter finding reflects that, at the nanoscale, the spark-plasma sintering kinetics is essentially dictated by the small size of the crystals and its associated effects.

4. The kinetics enhancement promoted by the high-energy ball-milling is progressive with the decrease in the crystal size that is achieved, although while it is only moderate with the refinement to the ultra-fine range, it is very abrupt with the refinement to the nanometre range.

5. High-energy ball-milling offers an exciting opportunity to reduce the spark-plasma sintering temperature of ZrB_2-SiC UHTCs. However, because this reduction is derived in part from the presence of amorphous borosilicate segregated at grain boundaries and at multi-grain joints, a judicious selection of the milling conditions and of the SiC content is required to find a proper balance between the lower-temperature densification and the resulting mechanical properties (and oxidation resistance).

"Science is organized knowledge. Wisdom is organized life"

Immanuel Kant (1724-1804)

Annex I: Experimental Equipment

The aim of this annex is simply to present the experimental equipment used in this Ph. D. thesis, deferring the details of the experimental set-up and conditions to the corresponding experimental sections in Chapters 2-7.

I.1 POWDER PREPARATION

- **Powder Homogenization:** The as-received powder mixtures were homogenized in polytetrafluoroethylene beakers of 1000 ml capacity using 200 ml of ethanol (Panreac, Madrid, Spain). Then, the beakers were placed on hot plates MC-8 (Bunsen, Madrid, Spain) with constant magnetic stirring until complete drying of the ceramic slurries (Fig. I.1).

Figure I.1. Beaker and hot-plate used for the homogenization of the as-received powder mixtures and drying of the ceramic slurries.

- **High-Energy Ball-Milling:** A high-energy Spex 8000D shaker mill with two milling chambers (CertiPrep Spex, Metuchen, United States) was used for the high-energy ball-milling (Fig. I.2).

Figure I.2. High-energy shaker mill used for the powder milling.

The containers were made of hardened steel, whereas the balls were made of tungsten carbide (WC) and had 6.7 mm in diameter (Fig. I.3).

Figure I.3. Milling containers and WC balls used for the high-energy ball-milling of the powders.

I.2 MICROSTRUCTURAL CHARACTERIZATION OF POWDERS AND BULK CERAMICS

- **Laser Scattering:** The particle size was measured by laser scattering using a Mastersizer 2000 equipment (Malvern Instruments, Worcestershire, United Kingdom), and the Hydro 2000MU module (Fig. I.4). The unit is equipped with two laser sources respectively.

Figure I.4. Equipment used for the particle size measurements.

The average particle size (D_a) was computed assuming a lognormal-type distribution using the following expression [1]:

$$D_a = D_{med}\, exp(0.5\sigma^2) \tag{I.1}$$

where D_{med} and σ are given, respectively, by:

$$D_{med} = \exp\left(\frac{\ln(D_S) - \frac{2.5}{3.5}\ln(D_v)}{1 - \frac{2.5}{3.5}}\right) \tag{I.2}$$

$$\sigma = \sqrt{\frac{\ln\left(\frac{D_v}{D_S}\right)}{1.5}} \tag{I.3}$$

and D_s and D_v are the surface-weighted mean diameter and volume-weighted mean diameter provided by the measurement equipment.

- **X-ray Diffractometry:** The experiments of X-ray diffraction have been performed with a high-resolution diffractometer D8 Advance (Bruker AXS, Karlsruhe, Germany). (Fig I.5).

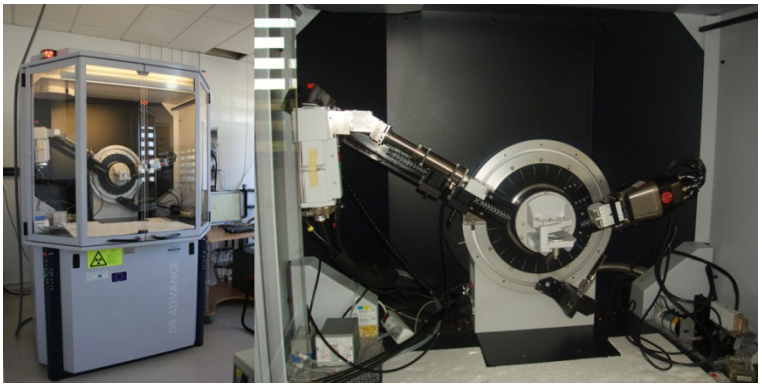

Figure I.5. X-ray diffractometer used to collect the X-ray diffraction patterns (left), and detail of the cabinet interior (right).

- **Scanning Electron Microscopy and X-ray Energy Dispersive Spectrometry:** Two scanning electron microscopes have been used for the examination of the microstructures and the particle morphology, as describe next.

One of them is a conventional microscope S-3600 (Hitachi, Ibarakiken, Japan), which is equipped with an energy dispersive X-ray spectrometer XFLASH Detector 3001 (Röntec GmbH, Berlin, Germany) Fig (I.6).

Figure I.6. Conventional scanning electron microscope with an energy dispersive X-ray spectrometer used for the microstructural characterization.

The other is a field-emission gun scanning electron microscope S4800-II (Hitachi, Ibarakiken, Japan), which is also equipped with an energy dispersive X-ray spectrometer XFLASH Detector 6/100 (Quantax Bruker, Berlin, Germany) (Fig. I.7).

The observations of scanning electron microscopy were made using both secondary and backscattered electrons, in the two cases in high vacuum mode.

Figure I.7. Field-emission gun scanning electron microscope with an energy dispersive X-ray spectrometer used for the microstructural characterization.

- **Transmission Electron Microscopy:** The direct examination of the size and morphology of the powder particles and nanocrystals was done using two conventional transmission electron microscopes. One of them is a Tecnai G^2 20 Twin (FEI, Eindhoven, The Netherlands) and the other one is a JEM-2100 (JEOL, Croissy-sur-Seine, France) (Fig. I.8.A and B, respectively).

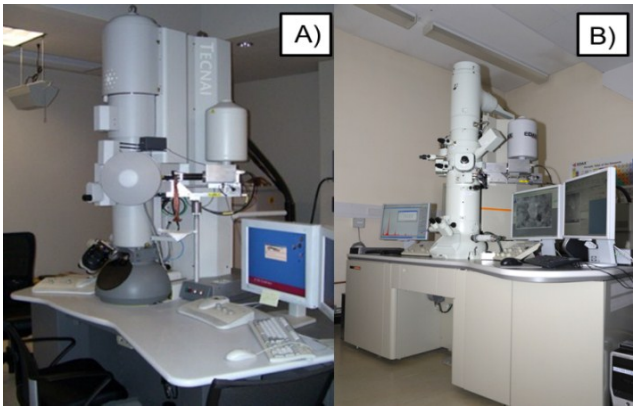

Figure I.8. TEM Tecnai G^2 20 Twin (A) and TEM JEM-2100 (B) used for the microstructural characterization of the powders.

➢ **Inert Gas Fusion Method:** The determination of the oxygen contents of various powder batches was performed by inert gas fusion using a TC-136 (Leco Instrument, St. Joseph, United States) instrument (Fig. I.9).

Figure I.9. Inert gas fusion equipment used to determine the oxygen contents in selected powders.

➢ **Helium Pycnometry:** Density measurements of the powders were made by helium pycnometry using a manual stereopycnometer (Quantachrome Instruments, Hartley Wintney, United Kingdom) (Fig I.10).

Figure I.10. Steropycnometer used to measure densities by Archimedes' method.

- **Infrared Spectrophotometry:** An infrared spectrophotometer Nicolet iS10 (Thermo Scientific, East Grinstead, United Kingdom) (Fig. I.11) was used to register the absorption spectra of selected powders.

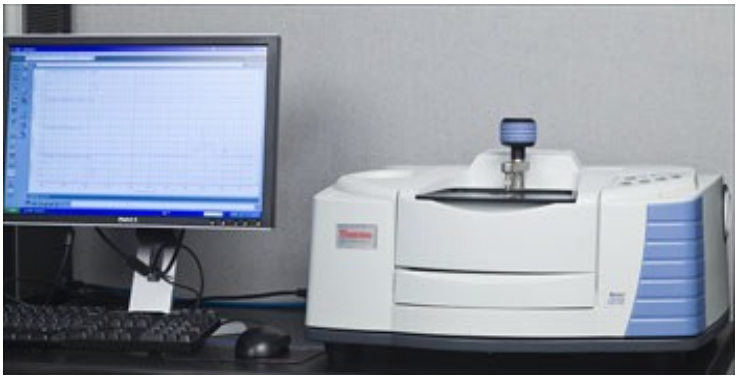

Figure I.11. Infrared spectrophotometer used for the determination of the bonding environment in selected powders

- **Raman Spectroscopy:** A Raman spectrometer Nicolet Almega XR (Thermo Scientific, East Grinstead, United Kingdom) (Fig I.12) was also used for the identification of the compounds present in selected powders.

Figure I.12. Micro-Raman spectrometer used for the determination of the bonding environment in selected powders.

➢ **X-ray Photoelectron Spectroscopy:** Detailed studies of the chemical status in selected powders were carried out using a high-resolution X-ray photoelectron spectrometer K-Alpha (Thermo Scientific, East Grinstead, United Kingdom) (Fig I.13).

Figure I.13. X-ray photoelectron spectrometer used for the determination of chemical status in selected powders.

➢ **Archimedes' Method:** Density measurements in bulk ceramics were made by Archimedes' method using an analytical balance equipped with hydrostatic weighing accessory CP 124S (Sartorius AG, Göettingen, Germany) (Fig I.14). The measurements were performed at ambient conditions using distilled water as immersion medium. The density was then calculated by the following equation:

$$\rho_R = \frac{W_{\mathrm{d}} \cdot \rho_{H_2O}}{W_{\mathrm{w}} - W_{\mathrm{i}}} \qquad \text{(I.4)}$$

where W_d, W_w and W_i are the weight in dry, wet, and immersion conditions, respectively, and ρ_{H2O} is the water density.

Figure I.14. Analytical balance with hydrostatic weighing equipment used to measure densities by Archimedes' method.

I.3 SINTERING

A Dr. Sinter SPS-2050 (Sumitomo Coal Mining Co., Tokyo, Japan) (Fig I.15) was used for the spark-plasma sintering. The equipment allows the recording of the shrinkage, shrinkage rate, temperature, current, voltage, and pressure, in real time. In all SPS cycles the DC pulse sequence used was 12:2. In addition, each pulse lasted 3.3 ms, and the group had a τ_{on} 39.6 ms : τ_{off} 6.6 ms ratio.

Chino KP1000 programmable controllers (Chino Works America Inc., Los Angeles, United States) allow the user to set load and temperature profiles independently up to the maximum capacity of 200 kN and 2200 °C. Voltage and current cannot be controlled directly. A temperature profile is programmed by the user and the current and voltage are adjusted by the SPS unit accordingly, up to a maximum output of 5000 A and 20 V.

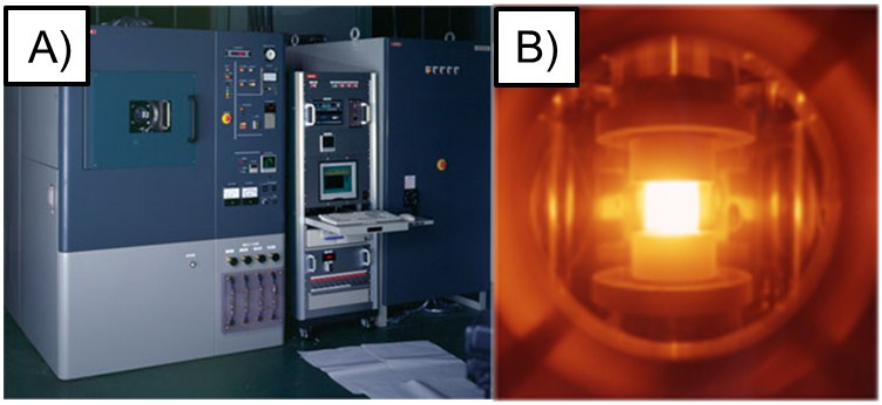

Figure I.15. Spark-plasma sintering furnace. (A) The equipment is shown at the left, the control unit is at the center, and the power unit is at the right. (B) A detail of the chamber interior during a typical sintering.

The powders were individually loaded into 12-mm diameter high-strength graphite dies lined with graphite foil and surrounded by a 1-cm thick graphite blanket to minimize the heat loss. Each die had an inner diameter of 12 mm, an outer diameter of 30 mm, and was 40 mm tall. Punches were cut to a 25 mm length from 12 mm diameter rods of the same grade graphite as the die. The die and punches were put in place using two 15 mm and one 30 mm graphite spacers as seen in Figure I.16. This configuration allows the correct alignment of the die with the window of the optical pyrometer.

The time, temperature, voltage, current, and displacement data were collected using LabView version 8.2 software. In particular, simultaneous values of temperature, applied force, electric current, voltage, and shrinkage were recorded in intervals of 6 s. The pressure in this SPS unit is applied by a hydraulic press with a moving lower ram. According to the manufacturer, the pressure in the Dr Sinter SPS 2050 unit is measured by a load cell with an accuracy of ±0.06 kN.

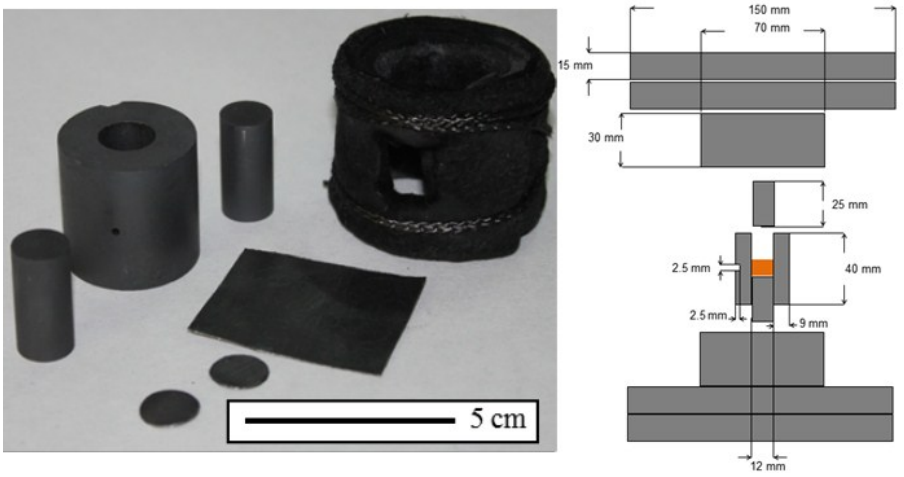

Figure I.16. Die, punches, blanket, and graphite foil used to sinter the bulk samples (left) and schematic of the die, punches, and spacers. Dimensions of each piece are given. The ceramic powder is represented by the orange object inside the die (right).

I.4 SURFACE FINISHING

- **Shot Peening:** To remove the thin layer of graphite adhered to the sample during spark-plasma sintering, a microblasting equipment Peenmatic 750S (Iepco, Leuggern, Switzerland) was used (Fig. I.17).

Figure I.17. Surface shoot-peening machine used to clean the sintered samples.

➢ **Polishing:** The specimens were embedded in epoxy resins, and the surfaces of the sintered samples were polished successively to a 1-µm finish employing first SiC grinding papers (240 grit-2 min, 400 grit-5 min, and 800 grit-10 min) and then diamond suspensions (9 µm-15 min, 6 µm-20 min, 3 µm-25 min and 1 µm-30 min) on woven synthetic clothes. The polishing was carried out using an automatic polishing machine Phoenix 4000 (Buehler Ltd., Waukegan, United States) (Fig I. 18). Some polished samples were also etched with a colloidal silica suspension (0,25 µm-5 min) . Finally, the polished samples were cleaned ultrasonically in ethanol for 15 min.

Figure I.18. Polishing machine, synthetic woven clothes, and diamond suspensions.

I.5 BASIC MECHANICAL CHARACTERIZATION

➢ **Vickers Testing:** The hardness and toughness were evaluated by Vickers indentation tests at ambient temperature. The indentations were carried out with a Vickers hardness tester Shimadzu HSV-30 (Shimadzu Corp., Kyoto, Japan) (Fig I.19).

Figure I.19. Vickers hardness tester.

Vickers hardness, H_v, was calculated using the following expression [2]:

$$H_v = \frac{P}{2a^2} \tag{I.6}$$

where P is the load (98N) and $2a$ is the average value of the diagonals of the indents.

The toughness was calculated by the following equation [3]:

$$K_{IC} = 0.016 \left(\frac{E}{H_v}\right)^{0.5} P c^{-1.5} \tag{I.7}$$

where E is the Young modulus, and $2c$ is the average radial-crack diameters.

At least 5 indentation tests were performed on each material tested. The measurement of the diagonals of the residual indents and of the radial-crack diameters were done with an optical microscope Nikon Epiphot 300 (Nikon Metrology NV, Leuven, Belgium) (Fig I.20.B), using an image analysis program (SigmaScan Pro v5, SPSS Inc. New York, United States).

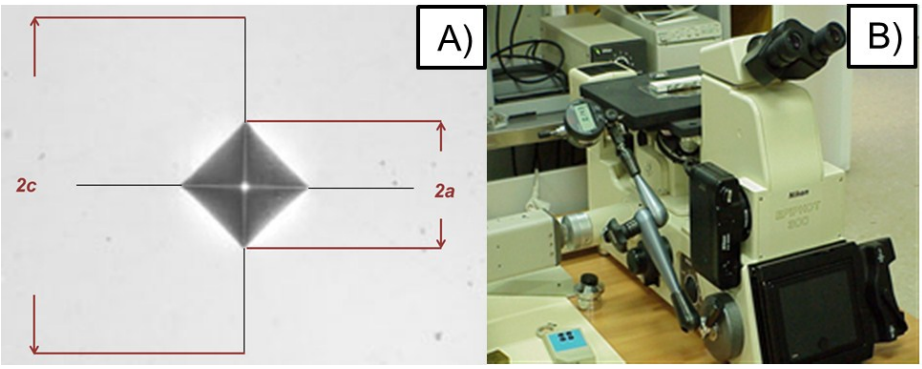

Figure I.20. Surface geometry of the residual indent in a Vickers test (A), and optical microscope (with an image-capture system) used for the observation and digitization of residual indents (B).

I.6. REFERENCES

1) Sánchez-Bajo, F., Ortiz, A. L. and Cumbrera, F. L. Novel analytical model for the determination of grain size distributions in nanocrystalline materials with low lattice microstrains by X-ray diffractometry. Acta Mater. 2006;54:1-10.

2) Lawn, B. R. Fracture of brittle solids. Cambridge University Press, Cambridge, United Kingdom, 1993.

3) Anstis, G. R., Chantikul, P., Marshall, D. B. and B. R. Lawn. A critical evaluation of indentation techniques for measuring fracture toughness: I. direct crack measurements. J Am Ceram Soc. 1981;64:533-38.

"You cannot teach a man anything; you can only help him discover it in himself"

Galileo Galilei (1564-1642)

Annex II: Determination of Densification Curves

Due to the importance of spark-plasma sintering (SPS) in this Ph.D. thesis, this annex describes in detail the procedure followed to correct the curves registered by the dilatometer of the SPS furnace with a view to determine the densification curves from displacement of the punches and relative density.

II.1 CORRECTION OF THE DISPLACEMENT CURVES

The simultaneous recording of temperature or time and of the displacement of the punches during SPS makes it possible to compute the densification kinetics if the final density of the sample is known. However, unfortunately the displacements measured directly with the dilatometer of the SPS furnace represent an overall characterization of shrinkage because such experimental curves include contributions not only from the powder but also from the die, punches, spacers and other system components. To determine the shrinkage curve of the powder itself (without the aforementioned

contributions), the same SPS cycle has to be repeated on a fully dense sample. When this is done, the displacement curve measured is due exclusively to the expansion of the graphite column and rest of components, and is therefore the baseline curve.

With this in mind, the shrinkage curve of the powder can be obtained simply by subtracting the baseline curve from the experimental curve, as is shown graphically in Fig II.1.

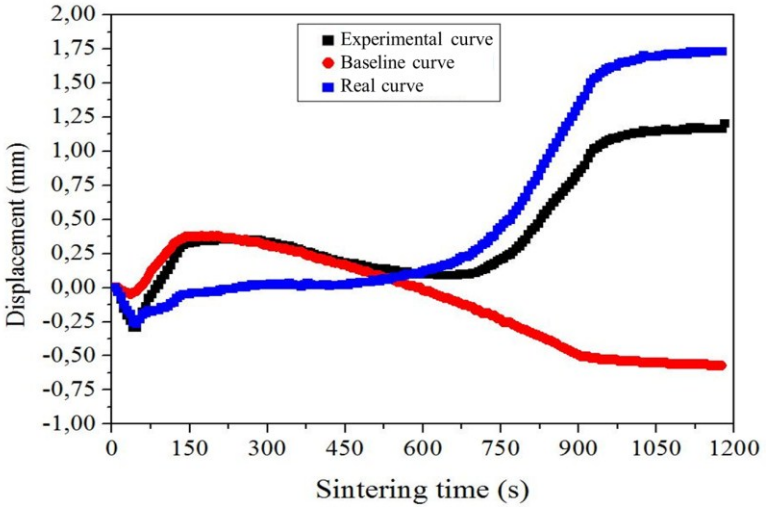

Figure II.1. Example of corrected displacement during the densification of ZrB_2 at 1825 °C under 75 MPa of pressure.

II.2 DETERMINATION OF THE DENSIFICATION CURVES

The so-calculated shrinkage values can then be converted to density values. The information needed to perform such a conversion is: (i) the final position indicated by the dilatometer at the conclusion of the SPS cycle (L_f),

(ii) the density of the sintered sample (ρ_f), for example as measured by Archimedes' method, and (iii) the thickness (e) of the sintered sample. Let us to define ΔL_j as the displacement at each moment of the SPS cycle, that is, the difference between the positions measured by the dilatometer at each moment (L_j) and that at the beginning of the experiment (L_0) (i.e, $\Delta L_j = L_j - L_0$). Normally, L_0 is set to 0 at the beginning of the SPS cycle so that ΔL_j is indeed equal to L_j, but this is not strictly needed. In any case, the absolute density of the compact at each moment of the SPS cycle ρ_j^a can be calculated using the following expression:

$$\rho_j^a = \frac{e \cdot \rho_f}{L_f - L_0 - \Delta L_j + e} = \frac{e \cdot \rho_f}{L_f - L_j + e} \qquad (II.2)$$

Fig. II.2 shows a drawing of the displacements during SPS, which is useful to understand the procedure described above.

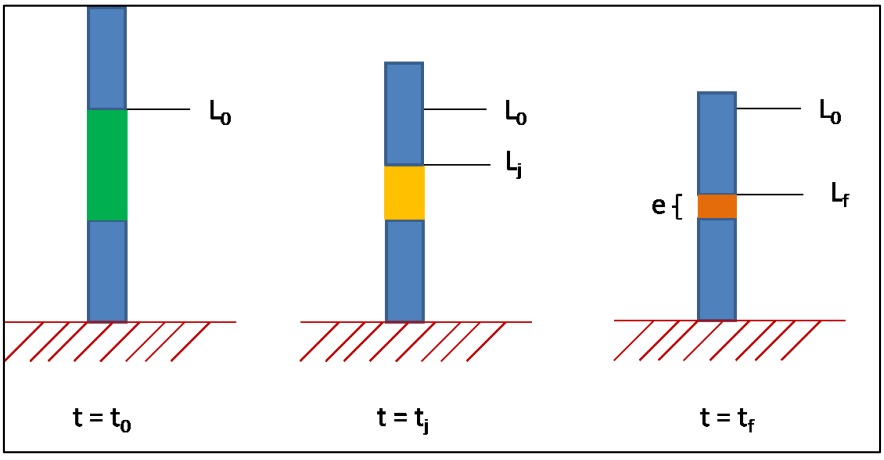

Figure II.2. Stages of the displacements during SPS, from which the expression (II.1) can be deduced.

Subsequently, the relative density curve is calculated from the absolute density curve simply by dividing the ρ_j^a values calculated according to expression II.1 by the theoretical density of the sintered sample (ρ_t). This leads to the following expression:

$$\rho_j^r = \frac{\rho_j^a}{\rho_t} \cdot 100 \qquad (II.2)$$